Universität Bremen

Theoretical Study of Charge Dynamics in Two-dimensional Materials

by

Yuxiang Liu

A thesis submitted in partial fulfillment
of the requirement for the degree of

Doctor of Philosophy in Physics

Supervisor: Prof. Thomas Frauenheim

Bremen Center for Computational Materials Science
University of Bremen
Bremen, Germany

Defense date: 06 March 2023

Bremen 2022

Universität Bremen

Universität Bremen | Postfach 33 04 40, 28334 Bremen

An
- Frau Yuxiang Liu
- die Mitglieder des Prüfungsausschusses

Bremen, d. 22.02.2023

Fachbereich 01
Physik / Elektrotechnik

Doris Pérez Fraga
Geschäftsstelle Promotionsausschuss Dr. rer. Nat.

S2370
Otto-Hahn-Allee 1

28359 Bremen

Tel. 218-62710

E-Mail: dperez@fb1.uni-bremen.de
www.uni-bremen.de/fb1/studium/promotion

E I N L A D U N G

zum Dissertationskolloquium von

Frau Yuxiang Liu

am: 06.03.2023 um 10:00 Uhr st. Raum: AIB Building Seminar Room

Titel der Dissertation:

Theoretical Study of Charge Dynamics in Two-dimensional Materials

1. Gutachter :	Herr Prof. Dr. Thomas Frauenheim
2. Gutachter:	Herr Prof. Dr. Chi-Yung Yam
1. Prüfer:	Herr Prof. Dr. Jens Falta – **Vorsitz der Prüfungskommission**
2. Prüfer:	Frau Dr. Merle Insa Silja Röhr (CNC (Raum 00.012c))
akad. Mitarbeiter:	Herr Dr. Mohamed Madjet
Student:	Herr Nils-Erik Schütte

Mit freundlichem Gruß
Im Auftrag

Prüfungsamt

Acknowledgements

During the three-year PhD student, I have lots of unforgettable memories and many thanks to several persons. Firstly, I would like to express my gratitude to Prof. Thomas Frauenheim, who gave me the precious opportunity to start the exciting route of scientific research in his group in Bremen Center for Computational Material Science (BCCMS). With his permanent support and supervision, I will firmly keep going on the academy. My deepest gratitude also goes to Prof. ChiYung Yam, who supervises most of my present investigation. His patient guidance, valuable suggestions and constructive comments help me grow from a rookie to a qualified PhD student. I am grateful for his warm hospitality offered during my visit to Beijing Computational Science Research Center before I came to Germany. Meanwhile, I would like to thank him for his continual assistance and helpful comments on this thesis. Prof. Meng Sheng is greatly acknowledged for his supervision on the TDAP code. His professional guidance was extremely useful for my study on nonadiabatic dynamics. My sincere appreciation appreciation also goes to Prof. Peter Déak who gave me professional instruments on solid state physics. Dr. Christof Köhler is particularly acknowledged for his assistance in solving HLRN cluster problems and software compilation. I would like to thank the rest of colleagues in BCCMS, such as Dr. Bálint Aradi and Pu Guo. I would like express my grateful appreciation for the enjoyable and fruitful discussion. My thanks also go to Prof. Martin Aeschlimann and Prof. Isabella Gierz for the productive discussion about charge transfer in graphene/WS_2 heterostructure. I am sincerely appreciate Prof. Yongbin Xu, Dr. Xianyang Lu and Qi Liu for supporting our theoretical prediction with experimental observations and for many fruitful discussions. I would like to express my gratitude to the former and current member of BCCMS secretaries Sandra Smit and Ann Kathrin Risken for their support about nonscientific tasks. I would like to appreciate all my friends in Germany and China, who gave me warm support. Finally, I would like to thank my family. Especially, my grandfather and father who provide me with endless support and stimulation. I am extremely thank for their education and I hope my achievements make them proud.

Yuxiang Liu
Bremen, May 2022

Abstract

Exfoliation of graphene in 2004 initiated intensive attention on layered two-dimensional (2D) materials. So far, except for graphene, a large family of 2D materials has been reported, such as transition metal dichalcogenides (TMDCs), hexagonal boron nitride (h-BN), black phosphorene (BP), metal nitrides/carbides (MXenes) and their van der Waals (vdW) heterostructures, *etc.* The large number of species, unique electrical and optical properties and versatile functionalities render 2D materials as promising materials for electronic, optoelectronic and photovoltaic devices. This thesis investigates ultrafast charge dynamics in 2D material system based on real-time time-dependent density functional theory (rt-TDDFT) method within Ehrenfest framework. This work is divided into three major parts.

In first part, we investigate the ultrafast interlayer charge transfer process in the graphene/WS_2 heterostructure. Our results demonstrate that photo-induced holes transfer from WS_2 to graphene more efficient than electrons. The ultrafast charge dynamics arises from the coupling to nuclear vibrations and its amplitude and polarity show a strong dependence on the external electric fields. Further analysis reveals that carrier dynamics in the heterostructure is the result of competition between interlayer and intralayer relaxation process, which is governed by the couplings between carriers and their acceptor states. This work establishes a firm correlation between the charge dynamics and couplings between states in 2D heterostructures, and provide practical methodology to manipulate carrier dynamics at heterointerfaces.

In second part, we study the carrier multiplication (CM) phenomenon in six monolayer TMDCs MX_2 (M = Mo, W; X = S, Se, Te). Our results present that CM is observed in all six TMDCs. The threshold energy of CM can be substantially reduced to 1.75 bandgap (E_g) via couplings to phonon modes. Since electron-phonon couplings (EPCs) can result in significant changes in electronic structures, even trigger semiconductor-metal transition, and eventually assist CM beyond threshold limit. Chalcogen vacancies can further decrease the threshold due to sub-gap defect states. In particular for WS_2, CM occurs with excitation energy of only $1.51E_g$. Our results identify TMDCs as attractive candidate materials for efficient photovoltaic devices with the advantages of high photo-conductivity and phonon-assisted CM

characteristic.

In third part, we report the effect of doping levels on CM in graphene. Our calculation results indicate that doping level can introduce remarkable differences in CM conversion efficiency in graphene. Specifically, the CM quantum yield (QY) can be promoted from 1.41 to 1.89 when the Fermi level rising from 0.40 eV to 0.78 eV via n-doping. Consistently, time- and angle-resolved photoemission spectroscopy (TR-ARPES) measurements on n-doped graphene present the same correlation between doping levels and CM conversion efficiency. Our results provide a practical strategy to promote the performance of graphene as a photovoltaic material by tuning doping levels.

List of publications

1 **Yuxiang Liu**, Jin Zhang, Sheng Meng, ChiYung Yam, Thomas Frauenheim, "Electric Field Tunable Ultrafast Interlayer Charge Transfer in Graphene/WS_2 Heterostructure", *Nano Letters* 2021, 21, 10, 4403–4409.

2 **Yuxiang Liu**, Thomas Frauenheim, ChiYung Yam, "Carrier Multiplication in Transition Metal Dichalcogenides Beyond Threshold Limit", *Advanced Science* 2022, 2203400.

3 Qi Liu*, Xianyang Lu* and **Yuxiang Liu*** et al, "Carrier Relaxation and Multiplication in Bi Doped Graphene", Small, 2023, 2206218.

List of abbreviation

ALDA	adiabatic local density approximation
ARPES	angle-resolved photoemission spectroscopy
E_g	bandgap
BP	black phosphorous
BO	Born-Oppenheimer
CM	carrier multiplication
CBM	conduction band minimum
DFT	density functional theory
DOS	density of states
EPC	electron-phonon coupling
FD	Fermi-Dirac
FSSH	fewest-switches surface hopping
FET	field effect transistor
FT	Fourier transform
GGA	generalized gradient approximation
h-BN	hexagonal boron nitride
HK	Hohenberg-Kohn
KS	Kohn-Sham
LDA	local density approximation
MXenes	metal nitrides/carbides
MQC	mixed quantum-classical
NAC	non-adiabatic coupling
NAMD	non-adiabatic molecular dynamics
PBE	Perdew-Burke-Ernzerhof
PES	potential energy surface
QY	quantum yield
rt-TDDFT	real-time time-dependent density functional theory
RG	Runge-Gross
TR-ARPES	time- and angle-resolved photoemission spectroscopy
TDSE	time-dependent Schödinger equation
2D	two-dimensional
TMDC	transition metal dichalcogenide
VBM	valence band maximum
vdW	van der Waals

Contents

List of Figures

List of Tables

Chapter 1

Introduction

1.1 Layered two-dimensional materials

Since graphene was successfully exfoliated in 2004[1], 2D materials have attracted intensive attention owing to their exceptional properties. Due to the quantum size effect, the transport of carriers, heat and photon can be strongly confined in 2D plane, leading to remarkable changes in electronic and optical properties [2, 3]. Graphene, as the best-known 2D material, exhibits extraordinary properties, including carrier mobility, optical transparency and thermal transport, making it as an promising candidate materials for electronic and photonic devices [4]. Thus, enormous applications, achievements and fundamental scientific research based on graphene inspired researchers to explore new members of 2D materials. The library of layered 2D materials grows fast, currently, it has consisted of more than 150 families. In general, 2D materials are categorized based on their structures, for example, graphene, TMDCs[5], h-BN[6], BP[7], MXenes[8, 9]. The emergence of diverse layered 2D materials has illustrated their promising potential applications in electronics, photovoltaic, catalysis and biomedicine[10–12].

Owing to zero bandgap semimetal nature, graphene presents high charge-carrier mobility and extraordinary conductivity [13, 14]. It has been reported that charge-carrier mobility of graphene can reach up to 2×10^5 $cm^2V^{-1}s^{-1}$[15, 16] and saturation velocities are $\sim5\times10^7$cm s^{-1}[17]. Such a highly permitting electron transport characteristics have potential benefits for the applications in field effect transistors (FETs), which could operate at frequencies as high as 100 GHz and even at terahertz frequencies[18, 19]. Graphene also offers a tremendously high optical transparency of up to 97.7%[20], which enables its superior performance in transparent electrodes in solar cell[21]. Meanwhile, the superb thermal conductivity, with a value of $\sim5\times10^3$ W/mK, establishes graphene as an excellent material for thermal management[22].

Except for graphene, TMDC materials, represented by MX_2 (M = Mo, W; X = S, Se, Te) also attract intense attention due to their unique electrical and optical properties. TMDCs exhibits indirect-to-direct bandgap transition when exfoliated from bulk to monolayer. This tunable bandgap accompanied by strong optical absorption and large exciton binding energy render TMDCs as optimal candidates for a variety of optoelectronic devices, including FETs, photodetectors, solar cells, light-emitting diodes, and phototransistors[23–27]. For example, monolayer MoS_2, with a direct bandgap ($\sim$ 1.8eV), good mobility ($\sim$ 700 $cm^2V^{-1}s^{-1}$), efficient optical absorption ($\sim 10^7$ m^{-1} for sunlight) and high current on/off ratio ($\sim 10^7$-10^8), is of great interest

of high-performance flexible electronics and optoelectronic devices[28].

With dangling-bond-free surface and free of lattice-matching, random combination of 2D materials in one vertical stack creates a plethora of vdW heterostructures[29, 30]. Owing to the weak vdW couplings, the vdW heterostructures could combine superior properties of individual components to achieve desirable functionalities[31, 32], opening up an unprecedented opportunity for the development of novel electronic, optoelectronic and spintronic devices. It has been demonstrated that vdW heterostructure is an optimal platform to construct vertical transistors, including tunneling FETs[33], band-to-band tunneling transistors[34] and hot carrier transistors[35]. In addition, vdW heterostructures also present superior performance in photodetection, especially for infrared photodetection, with ultrafast response speed, ultrahigh sensitivity and polarization sensitivity[36–38]. It has been reported that vdW heterostructures have various magnetic properties, including ferromagnetic semiconductors/metals, antiferromagnetic insulators[39, 40]. The magnetism of these 2D magnets can be tuned by applying external electric fields and varying carrier concentration. Such characteristics provides possibilities to design diverse magnetic devices, such as memory devices, logic devices etc[41, 42].

1.2 Ultrafast dynamics in 2D materials

Owing to the atomically thin thickness, carriers in vdW heterostructures are exposed to layer-layer coupling, the properties of heterostructures are determined not only by constituent monolayer, but also by the interactions between the layers. For example, the formation of vdW heterostructures in TMDC layers can profoundly affect their excited-state dynamics, ranging from dissociation of intralayer excitons and the formation of interlayer excitons to the relaxation of spin and valley polarization[43]. Manipulation of band alignment provides a powerful way to control and optimize the charge dynamics in TMDC heterostructures. In type-I heterostructures, photo-induced carriers can only flow from the layer with a larger bandgap to the layer with a narrower bandgap[44]. In type-II heterostructures, on the other hand, electrons are accumulated in the layer with a lower conduction band minimum (CBM), while holes are maintained in the other layer with a higher valence band maximum (VBM)[45]. In general, photo-excited carrier dynamics process extends from hundreds of femtoseconds to several microseconds in TMDC heterostructures [46]. On the short timescale ($\leq$1 ps), interlayer/intralyer charge transfer and energy

dissipation dominate the relaxation dynamics. On the longer timescale ($\geq$1 ps), the recombination of interlayer excitons is relevant[47]. The rate of these process can be varied by order of magnitude depending on the constituent layers, stack configurations and external electric fields for heterostructures[48–50]. Therefore, understanding the charge carrier dynamics in vdW heterostructures is of central importance for their potential applications in electronics and optoelectronics.

Photoexcitation with phonon energy exceeding E_g can create electron-hole pairs in semiconductors. When the excess energy of excited carriers is beyond E_g, carriers obtain sufficient energy to scatter an additional electron from occupied valence bands to empty conduction bands through Coulomb interactions. This process is known as CM, which is the reverse process of Auger recombination. It is reported that CM can overcome the Schokley-Queisser limit and raise solar cell efficiency up to $\sim$46%[51]. Energy conservation limits optimal CM threshold to be $\sim 2E_g$. However, CM is inefficient in bulk semiconductor with the threshold energy of $\sim 6E_g$ due to constraints imposed by the momentum conservation rule[52] and competitive phonon-assisted energy dissipation. The situation is different in nanostructures, where quantum confinement relaxes the strict momentum conservation requirement and phonon bottleneck inhibits phonon emission[53, 54]. CM has been predicted to be extraordinary effective in graphene, due to its linear band structure[55, 56] combined with weak EPC[57, 58] and strong electron-electron scattering[59, 60]. Further research demonstrates that the amount of generated hot carriers is highly sensitive to the doping level of graphene, that is, the location of Fermi level[61]. The tunability of ultrafast hot carrier dynamics via doping concentration provides an effective approach to control photoconductivity properties of graphene. Meanwhile, CM phenomenon is observed in monolayer TMDCs with threshold as low as $2E_g$, and conversion efficiency can reach up to 99%[62, 63]. These characteristics are superior to previously reported nanocrystals[64–66], which provide a practical strategy to improve the performance of graphene/TMDC heterostructures in optoelectronic devices.

1.3 Theoretical method

Density functional theory (DFT), based on single-particle Kohn-Sham (KS) equations[67, 68], have successfully described ground-states properties, such as bond lengths and bond energies, but it is not suitable for dealing with excited states

quantitatively. A well-known example is that DFT underestimates semiconductor bandgap by more than 50%, which is attributed by the lack of electron-hole interactions and the screening effects in DFT. While TDDFT, developed by Runge and Gross[69], can give accurate values for bandgaps, absorption spectra, and many other excited state properties, including non-adiabatic couplings, potential energy surfaces (PESs), electron transport, atom collisions and molecular vibrations under a strong field[70]. Although an exact theory in principle, TDDFT based on adiabatic local density approximation (ALDA), has limitations in describing Rydberg states, charge transfer and multiple excitation states[71, 72]. Incorporating exact-exchange or modified algorithms in exchange-correlation functional presents significant improvements in above challenging situations[73–75], which maintains a perfect balance between computational cost and high accuracy.

There are numerical implementations of TDDFT. Most conventional TDDFT simulations involve linear response of electron density to an external field with a given frequency, and are generally formulated in the frequency domain[76]. This scheme can reproduce absorption and oscillator strengths accurately by calculating the poles of the density-density response function. However, the dynamics of the excited carriers cannot be investigated. While rt-TDDFT evolves wavefunctions in the time domain, which yields a full time-resolved, potentially non-linear solution. To describe excites states correctly, the most ambitious method is to treat the entire system, including nuclei, quantum-mechanically. Unfortunately, the expensive computational costs limit the scope of applications and can only be applied to small systems within a short timescale. If the nuclear quantum effects are unimportant, the system can be dealt with a mixed quantum-classical (MQC) method, where electronic subsystem is described quantum mechanically while nuclear subsystem evolves along classical Newton's trajectories.

The key issue in quantum-classical method is the quantum-classical self-consistency problem: the electronic subsystem must propagate correctly under the influence of nuclear subsystem, with the transitions between different quantum states along the evolution process; meanwhile, the trajectories of nuclei must respond to the quantum transitions. Ehrenfest dynamics and surface hopping are the most widely applied methods to solve time-dependent Schördinger equation. Ehrenfest method, also known as mean-field method, evolves classical subsystem on a averaged PES, which provides a good description of the transition probabilities. Surface hopping, on the other side, describes the quantum-classical correlation via stochastic hops

between different PESs[77, 78].

1.4 Outline of the thesis

This thesis is written in a cumulative form, with main results published in peer-reviewed journals. This thesis is organised as follows:

Chapter 1 gives a brief introduction to the main topics covered in the rest of thesis.

Chapter 2 describes the basic theoretical background of the most important quantum-mechanical methods used in this work.

Chapter 3 presents the results of my work on the ultrafast charge transfer in graphene/WS_2 heterostructure. A thorough analysis on the possible origins of the ultrafast interlayer charge transfer is presented. Practical methods to manipulate heterointerfacial carrier dynamics are also given. This chapter is based on article 1 in the list of publications.

Chapter 4 introduces the CM characteristics in monolayer MX_2 (M = Mo, W; X = S, Se, Te). A detailed discussion of the role of phonon modes in CM process is presented, which provides insight into the design strategy to break CM threshold limit in monolayer TMDCs. This chapter is based on the article 2 in the list of the publications.

Chapter 5 contains the investigation of the effect of doping level on CM in graphene. Theoretical simulations and experimental measurements figure out the mechanism of CM in doped graphene, which pave a new pathway to improve graphene efficiency in optoelectronic devices. This chapter is based on the article 3 in the list of the publications.

Additional information related to chapter 3, 4 and 5 is given in appendices.

Chapter 2

General theory

2.1 Density functional theory - an overview

Since the advent of quantum mechanics, it was realized that many-body Schödinger equation cannot solved exactly. The idea of implementation of electron density was considered as a practical way to describe a many-body system. Although the origin of DFT can be traced back to Thomas-Fermi model[79, 80], the modern DFT was established based on Hohenberg-Kohn (HK) theorem[81].

Based on Born-Oppenheimer (BO) approximation[82], a stationary electronic state Ψ satisfies many-body time-independent Schödinger equation

$$\hat{H}\Psi = \left[\hat{T} + \hat{V} + \hat{U}\right]\Psi = \left[\sum_{i=1}^{N} -\frac{\nabla_i^2}{2} + \sum_{i=1}^{N} V(\boldsymbol{r}_i) + \sum_{i=1}^{N}\sum_{j<i}^{N} U(\boldsymbol{r}_i, \boldsymbol{r}_j)\right]\Psi = E\Psi \tag{2.1}$$

in which the kinetic energy, external field potential energy and electron-electron interaction energy are denoted by $\hat{T}$, $\hat{V}$, and $\hat{U}$, respectively.

The central statement of HK theorem can be summarized as follows:

- The external potential $\hat{V}$, and hence the total energy E, is a unique functional of the electronic density $\rho(\boldsymbol{r})$.
- Ground state energy can be written as a functional of density $E[n]$, which gives the ground state energy E_0 if and only if the input density is the true ground state density $\rho_0(\boldsymbol{r})$.
- There exists a density functional $F[\rho]$:

$$E\left[\rho\right] = F\left[\rho\right] + \int \rho(\boldsymbol{r})V(\boldsymbol{r})d\boldsymbol{r} \tag{2.2}$$

  where $F[\rho]$ is universal functional of density, which is independent of external potential $V[\boldsymbol{r}]$

Thus, instead of solving many-body Schödinger equation, the ground state eigenvalue can be obtain, at least in principle, by minimizing the density functional in Eq.2.2. However, the explicit form of $F[\rho]$ remains unknown, and approximations have been suggested, such as Thomas-Fermi approximation. Unfortunately, the accuracy of existed approximations is unsatisfactory, making HK theorem rather limited in practical calculations.

A major milestone in the development of modern DFT is KS equation[83], in which introduces a fictitious non-interacting system with the same density as the original system. In this way, the universal functional $F[\rho]$ can be written as a sum of kinetic energy of non-interacting system, the Coulomb energy and an uncertain term exchange-correlation energy

$$\begin{aligned} F\left[\rho\right] &= T_s\left[\rho\right] + V_H\left[\rho\right] + E_{xc}\left[\rho\right] \\ &= -\frac{\hbar^2}{2m}\sum_i f_i \left\langle \psi_i \left| \nabla^2 \right| \psi_i \right\rangle + \frac{1}{2}\int\int d\boldsymbol{r_1} d\boldsymbol{r_2} \frac{\rho(\boldsymbol{r}_1)\rho(\boldsymbol{r}_2)}{|\boldsymbol{r}_1 - \boldsymbol{r}_2|} + E_{xc}\left[\rho\right] \end{aligned} \tag{2.3}$$

The ground state wavefunction of non-interacting system is expressed as a Slater determinant with single-particle orbitals ψ_i. The density can then be computed from single-particle orbitals

$$\rho(\boldsymbol{r}) = \sum_i f_i \left|\psi_i(\boldsymbol{r})\right|^2 \tag{2.4}$$

With Eq.2.3 and Eq.2.4, a set of single-particle orbitals can be found to minimize $E[\rho]$ under the constraints of $\sum_i^{occ}\langle\psi_i|\psi_i\rangle = N$. Shödinger-type equations for such coupled single-particle orbitals are

$$\left[-\frac{\nabla^2}{2} + \nu_s(\boldsymbol{r})\right]\psi_i(\boldsymbol{r}) = \epsilon_i\psi_i(\boldsymbol{r}) \tag{2.5}$$

in which ν_s is effective single-particle potential, given by

$$\nu_s(\boldsymbol{r}) \equiv \nu_{ext}(\boldsymbol{r}) + \int d\boldsymbol{r'}\frac{\rho(\boldsymbol{r'})}{|\boldsymbol{r} - \boldsymbol{r'}|} + \nu_{xc}\left[\rho\right](\boldsymbol{r}) \tag{2.6}$$

The last two terms are referred as Hartree and exchange-correlation potential, where the exchange-correlation potential is defined by

$$\nu_{xc}\left[\rho\right](\boldsymbol{r}) = \frac{\delta E_{xc}\left[\rho\right]}{\delta\rho(\boldsymbol{r})} \tag{2.7}$$

Eq.2.5 is known as KS equation. Since ν_s is a functional of density, KS equations must be solved self-consistently.

Clearly, an approximation for $E_{xc}[\rho]$ is needed for practical DFT calculations. On the one hand, the approximate $E_{xc}[\rho]$ functionals can be applied to any system of interest. On the other hand, a good approximation should perform equally well for very different physical situations. Local density approximation (LDA) is the simplest E_{xc} functional, which depends solely upon the electronic density on each

point in space. In LDA, the exchange-correlation energy, for a spin-unpolarized system, is written as

$$E_{xc}^{LDA}[\rho] = \int d\boldsymbol{r}\rho(\boldsymbol{r})\epsilon_{xc}(\rho(\boldsymbol{r})) \tag{2.8}$$

where $\epsilon_{xc}(\rho)$ is exchange-correlation energy per particle of a homogeneous electron gas with charge density ρ. LDA has been demonstrated to be a remarkably accurate for a wide variety of system with slowly varying spatial density.

A profound improvement is achieved via the emergence of generalized gradient approximation (GGA). Since LDA is derived from homogeneous gas model which tends to underestimate the exchange energy and overestimate the correlation energy[84]. Within GGA functional, the gradient of the density is included to account for the non-homogeneity of the true electron density. The expansion has following form

$$E_{xc}^{GGA}[\rho] = \int d\boldsymbol{r}\rho(\boldsymbol{r})\epsilon_{xc}(\rho(\boldsymbol{r}), \nabla\rho(\boldsymbol{r})) \tag{2.9}$$

The impact of GGA is quite dramatic, especially in molecular geometries and ground state energies.

In recent years, potentially more accurate meta-GGA functionals are developed, which incorporate second derivative of the electron density based on GGA functionals. The meta-GGA functionals take the form

$$E_{xc}^{MGGA}[\rho] = \int d\boldsymbol{r}\rho(\boldsymbol{r})\epsilon_{xc}(\rho(\boldsymbol{r}), \nabla\rho(\boldsymbol{r}), \nabla^2\rho(\boldsymbol{r}), \tau(\boldsymbol{r})) \tag{2.10}$$

with $\tau(\boldsymbol{r}) = \frac{1}{2}\sum_i^{occ} |\nabla\varphi_i(\boldsymbol{r})|^2$, the non-interacting positive kinetic energy density. Thus, the additional flexibility of the functional form gained by introducing new variables can be used to incorporate more precise properties into approximations. In this way, it has been possible to improve the accuracy of GGA for some physical properties.

The final class of approximations to exchange-correlation energy are so-called hybrid functionals which incorporate a portion of exact exchange energy from Hartree-Fork theory with the rest of the exchange-correlation energy from other schemes, such as LDA or GGA,

$$E_{xc}^{HYB}[\rho] = aE_x^{HF}[\rho] + (1-a)E_x[\rho] + E_c[\rho] \tag{2.11}$$

in which a is the empirical mixing parameter. Hybrid functional are tremendously popular and successful in quantum chemistry.

Developing accurate approximations for E_{xc} is an ongoing topic. Currently, KS-DFT has successfully yields excellent results for the ground state properties even

with the simplest LDA functionals. However, KS-DFT scheme cannot give a reliable description of excited states, such as absorption spectra, bandgap in semiconductors etc.

2.2 Time-dependent extension

DFT has presented its superior advantages to handle an ample range of stationary problems. While TDDFT is an extension of DFT, which aims to investigate properties and dynamics of many-body system in the presence of time-dependent potentials, such as electric or laser fields. TDDFT has successfully captured features like, excitation energy, photoabsorption spectra and frequency-dependent response properties.

2.2.1 Formal foundations of TDDFT

Time-dependent Schördinger equation (TDSE) for a many-body system is as follows

$$i\frac{\partial}{\partial t}\Psi(\boldsymbol{r},t) = \hat{H}(\boldsymbol{r},t)\Psi(\boldsymbol{r},t) \tag{2.12}$$

Although the many-body Schördinger equation achieves a remarkably excellent description of nature, it poses a tricky task of computational complexity. In fact, even the simulations of Helium atom in a laser field take several months with a modern computer[85]. In this circumstance, TDDFT was developed to relieve the computational burden. The formal foundation of TDDFT is the Runge-Gross (RG) theorem[86], a time-dependent analogue of HK theorem. Similarly, the central idea of RG theorem can be summarized as

- For a give initial state, time-dependent density is a unique functional of external potentials.

Unlike stationary systems, there is no variational principle on the basis of total energy in time-dependent scheme. However, there exists a quantity analogous to the energy, the quantum mechanical action

$$\mathcal{A}[\rho] = \int_{t_0}^{t_1} \left\langle \Psi[\rho](t) \left| i\frac{\partial}{\partial t} - \hat{H}(t) \right| \Psi[\rho](t) \right\rangle dt \tag{2.13}$$

Time-dependent problem can therefore be solved by calculating the stationary point of the functional $\mathcal{A}[\rho]$, yielding the so-called time-dependent KS equation

$$\hat{H}_{el}\psi_i(\boldsymbol{r},t) = \left[-\frac{1}{2}\nabla^2 + \nu_s(\boldsymbol{r},t)\right]\psi_i(\boldsymbol{r},t) = i\frac{\partial\psi_i(\boldsymbol{r},t)}{\partial t} \tag{2.14}$$

in which $\psi_i(\boldsymbol{r},t)$ are the TDKS orbitals which produces the time-dependent density

$$\rho(\boldsymbol{r},t) = \sum_i f_i \left|\psi_j(\boldsymbol{r},t)\right|^2 \tag{2.15}$$

and the TDKS effective potential can be expressed as

$$\nu_s(\boldsymbol{r},t) = \nu_{ext}(\boldsymbol{r},t) + \int \frac{\rho(\boldsymbol{r'},t)}{|\boldsymbol{r}-\boldsymbol{r'}|}d\boldsymbol{r'} + \nu_{xc}[\rho](\boldsymbol{r},t) \tag{2.16}$$

The last term, time-dependent exchange-correlation potential, can be written as the functional derivative of exchange-correlation part of $E_{xc}[\rho]$

$$\nu_{xc}\left[\rho\right](\boldsymbol{r},t) = \frac{\delta E_{xc}\left[\rho\right]}{\delta\rho(\boldsymbol{r},t)} \tag{2.17}$$

Exchange-correlation potential is evaluated from electron density at a particular time. But it does not contain the information about the history of the density, which implies that memory effects on exchange-correlation potential are completely ignored. The response of exchange-correlation potential to density fluctuations can be directly derived from the second derivative of E_{xc}

$$\frac{E_{xc}\left[\rho\right]}{\delta\rho(\boldsymbol{r},t)\delta\rho(\boldsymbol{r'},t)} = \frac{\delta\nu_{xc}\left[\rho\right](\boldsymbol{r},t)}{\delta\rho(\boldsymbol{r'},t)} \cong \delta(t-t')\frac{\delta\nu_{xc}\left[\rho\right](\boldsymbol{r})}{\delta\rho(\boldsymbol{r'})} \tag{2.18}$$

Inevitably, the exact expression of ν_{xc} is unknown. In contrast to stationary DFT, approximations to ν_{xc} are still in their infancy. The simplest one is ALDA, which assumes ν_{xc} is the ground state exchange-correlation functional at each time.

$$\nu_{xc}^{ALDA}[\rho](\boldsymbol{r},t) = \nu_{xc}^{LDA}[\rho]|_{\rho=\rho(\boldsymbol{r},t)} \tag{2.19}$$

This adiabatic approximation brings considerable simplicity to the scheme and yields excellent performance in many cases, such as excitation energies[87]. Naturally, ALDA approximation inherits shortcomings of LDA, showing poor descriptions of charge transfer, double excited states, Rydberg excited states, as well as conical intersections[72, 88–92]. Many efforts have been made to go beyond the adiabatic approximation, including time-dependent optimized effective potential approximation[93] and functional with memory[94], etc.

2.2.2 Linear response

There are two major methods to solve TDKS equations, namely, linear response technique and real-time propagation of KS orbitals. Linear response technique is a perturbative method which is limited to weak fields. Excitation energy can be exacted within this frame due to the discrete poles at these energies.

Time-dependent external potential can be express as

$$\nu_{ext}(\boldsymbol{r},t) = \nu_{ext}(\boldsymbol{r},0) + \delta\nu_{ext}(\boldsymbol{r},t) \tag{2.20}$$

The system will respond to this perturbation, and the response can be written as

$$\rho(\boldsymbol{r},t) = \rho(\boldsymbol{r},0) + \delta\rho(\boldsymbol{r},t) + \delta\rho^{(2)}(\boldsymbol{r},t) + \cdots \tag{2.21}$$

The first order response is expressed as

$$\delta\rho(\boldsymbol{r},t) = \int dt' \int d\boldsymbol{r'}\chi(\boldsymbol{r},\boldsymbol{r'},t-t')\delta\nu_{ext}(\boldsymbol{r'},t') \tag{2.22}$$

The polarizability χ is the linear density-density response function of the system.The above response functions are in time domain. With Fourier transform (FT) and convolution theorem, the time-dependent equations can be transformed to frequency-dependent equations, which allows to determine the response to individual frequencies of light. Performing FT and convolution, the density linear response is

$$\delta\rho(\boldsymbol{r},w) = \int d\boldsymbol{r'}\chi(\boldsymbol{r},\boldsymbol{r'},w)\delta\nu_{ext}(\boldsymbol{r'},w) \tag{2.23}$$

with

$$\chi(\boldsymbol{r},\boldsymbol{r'},\omega) = \lim_{\eta\to 0^+}\sum_I \left[\frac{\langle\Psi_0|\hat{\rho}(\boldsymbol{r})|\Psi_I\rangle\langle\Psi_I|\hat{\rho}(\boldsymbol{r'})|\Psi_0\rangle}{\omega-(E_I-E_0)+i\eta} - \frac{\langle\Psi_0|\hat{\rho}(\boldsymbol{r'})|\Psi_I\rangle\langle\Psi_I|\hat{\rho}(\boldsymbol{r})|\Psi_0\rangle}{\omega+(E_I-E_0)+i\eta}\right] \tag{2.24}$$

where Ψ_0 and and Ψ_I represent many-body wavefunction of ground state and Ith excited state, and corresponding energy are labeled by E_0 and E_I. If Ψ_0 is single determinant, we could get

$$\chi^0(\boldsymbol{r},\boldsymbol{r'},\omega) = \lim_{\eta\to 0^+}\sum_{ij}^{\infty}(f_i-f_j)\left[\frac{\psi_i^*(\boldsymbol{r})\psi_j^*(\boldsymbol{r})\psi_i(\boldsymbol{r'})\psi_j^*(\boldsymbol{r'})}{\omega-(\epsilon_j-\epsilon_i)+i\eta} - \frac{\psi_i^*(\boldsymbol{r})\psi_j^*(\boldsymbol{r})\psi_i(\boldsymbol{r'})\psi_j^*(\boldsymbol{r'})}{\omega+(\epsilon_j-\epsilon_i)+i\eta}\right] \tag{2.25}$$

where f_i is the occupation of ψ_i orbital in KS ground state.

Dyson-like equation for the polarizabilty χ is

$$\chi = \chi^0 + \chi^0 \left[\nu_H + f_{xc}\right] \chi \tag{2.26}$$

with

$$f_{xc} = \frac{\delta \nu_{xc}}{\delta \rho} \tag{2.27}$$

where ν_H is Hartree potential, and f_{xc} is the exchange-correlation kernel.

The poles of polarizability χ are the excitation energies of system, which can be obtained via the solution to an eigenvalue problem. To explore the excitation energies, we move to the matrix representation to solve Casida equation[95]

$$\left[\begin{smallmatrix} A & K \\ -K^* & -A^* \end{smallmatrix}\right] \left[\begin{smallmatrix} X \\ Y \end{smallmatrix}\right] = E_\lambda \left[\begin{smallmatrix} X \\ Y \end{smallmatrix}\right] \tag{2.28}$$

Based on adiabatic approximation, A and K are frequency-independent, as follows

$$A_{ij}^{kl} = (\epsilon_j - \epsilon_i)\delta_{ik}\delta_{jl} + K_{ij}^{kl} \tag{2.29}$$

$$K_{ij}^{kl} = \int d\boldsymbol{r} \int d\boldsymbol{r'} \psi_i^*(\boldsymbol{r})\psi_j(\boldsymbol{r})(\nu_H + f_{xc})\psi_k(\boldsymbol{r'})\psi_l(\boldsymbol{r'}) \tag{2.30}$$

Hence, the excitation energies and eigenvectors of given systems can be yielded by Eq.2.28.

2.2.3 Real-time time-dependent density functional theory

Rt-TDDFT is another mature methodology to solve TDKS equations, which is based on integrating the TDKS equations in time domain. In contrast to linear response TDDFT which computes transition frequency from a ground state reference. Rt-TDDFT is superiorly powerful technique to simulate ultrafast carrier dynamics, including interlayer charge transfer and the response to external fields. Being intrinsically non-perturbative, rt-TDDFT can also cooperate with both the linear and nonlinear regime of excitation.

As an exact theory in principle, approximations must be employed to maintain a perfect balance between computational cost and high accuracy. The most common approximation is adiabatic approximation, also named by BO approximation which assume electron and nuclei evolve on different time scale, allowing the system Hamiltonian splitting into fast (electron) and slow (nuclei) degrees of freedom. Within adiabatic approximation framework, rt-TDDFT gives surprisingly well descriptions

of systems in weak fields. However, adiabatic approximation cannot account for multielectron excitation which is deviate from ground states. In such a case, excited state molecular dynamics occurs beyond BO regime, and is non-adiabatic. Non-adiabatic molecular dynamics (NAMD) modeling is nontrivial and consists of two basic components. On the one hand, electronic structure methodology adequately depicts excited state PESs. On the other hand, MD algorithms can describe non-adiabatic phenomena and trajectory propagation. Recently, numerous methods have developed to deal with the quantum effects arising from the nuclear motions, which ranges from fully quantum-mechanical treatment of nuclei[96, 97] to semiclassical[98] to MQC methods[99]. The first class is the most ambitious approach to account for excited state dynamics which is limited by the computational cost. The latter two classes are particularly suitable for large systems. Ehrenfest dynamics[100–103] and surface hopping method[104] are the most widely applied MQC methodology.

Mean-field trajectory method, so-called Ehrenfest, is the simplest MQC approach. Assuming the nuclear wavefunction represented by a single Gaussian wavepacket basis, the many-body wavefunction in Eq.2.12 can be rewritten as

$$\Psi(\boldsymbol{r}, \boldsymbol{R}, t) = \Phi_0(\boldsymbol{R}, t) \sum_i c_i(t) \psi_i(\boldsymbol{r}, \boldsymbol{R}) \tag{2.31}$$

in which $\Phi_0(\boldsymbol{R}, t)$ is a normalized single phase-less Gaussian wavepacket. $c_i(t)$ is the time-dependent coefficient of electronic wavefunction and $\psi_i(\boldsymbol{r}, \boldsymbol{R})$ is the solution of stationary Schödinger equation. Thus, TDSE can be expressed as

$$\begin{aligned} i\frac{\partial \Psi(\boldsymbol{r}, \boldsymbol{R}, t)}{\partial t} = \sum_i \Big[& \Phi_0(\boldsymbol{R}, t) \hat{H}_{el} \psi_i(\boldsymbol{r}, \boldsymbol{R}) + \psi_i(\boldsymbol{r}, \boldsymbol{R})(-\frac{\nabla_R^2}{2}) \Phi_0(\boldsymbol{R}, t) \\ & - \nabla_R \Phi_0(\boldsymbol{R}, t) \nabla_R \psi_i(\boldsymbol{r}, \boldsymbol{R}) + \Phi_0(\boldsymbol{R}, t)(-\frac{\nabla_R^2}{2}) \psi_i(\boldsymbol{r}, \boldsymbol{R}) \Big] c_i(t) \end{aligned} \tag{2.32}$$

Multiplied by $\Phi_0^*(\boldsymbol{R}, t)$ and $\psi_j^*(\boldsymbol{r}, \boldsymbol{R})$ on the both sides of Eq.2.32, and integrating overall nuclear space $\boldsymbol{R}$ and electronic space $\boldsymbol{r}$

$$i\frac{\partial c_i(t)}{\partial t} = \left[\epsilon_i + \hat{T}_N\right] c_i(t) + \sum_j \left[- \langle \Phi_0 | \nabla_R | \Phi_0 \rangle d_{ji}^{(1)} + (-\frac{1}{2}) d_{ji}^{(2)} \right] c_j(t) \tag{2.33}$$

where $d_{ji}^{(n)}$ are the nth order non-adiabatic couplings (NACs) between electronic states j and i

$$d_{ji}^{(1)} = \langle \psi_j | \nabla_R | \psi_i \rangle \tag{2.34}$$

$$d_{ji}^{(2)} = \langle \psi_j | \nabla_R^2 | \psi_i \rangle \tag{2.35}$$

Nuclear degrees of freedom are treated classically, as following

$$T_N \equiv -\frac{\hbar^2}{2M}\nabla_R^2 \rightarrow \frac{\vec{P}^2}{2M} \tag{2.36}$$

Due to assumption of a single uncorrelated nuclear wavepacket, the kinetic contribution in Eq.2.33 can be ignored which is a constant across the different electronic states. Second order NACs $d_{ja}^{(2)} \approx 0$. Thus, inserting Eq.2.36 into Eq.2.33

$$i\frac{\partial c_i(t)}{\partial t} = \epsilon_i c_i(t) - \frac{i}{\hbar}\sum_j d_{ji}^{(1)} \vec{P} c_j(t) \tag{2.37}$$

The equations of motions for $\boldsymbol{R}$ and $\vec{P}$ are obtained by Ehrenfest theorem [105] and electronic Hamiltonian

$$\frac{\partial \boldsymbol{R}}{\partial t} = \frac{\vec{P}}{M} \tag{2.38}$$

$$\frac{\partial \vec{P}}{\partial t} = -\langle \Psi | \nabla_R \hat{H}_{el} | \Psi \rangle \tag{2.39}$$

The force acting on nuclear classical trajectory is give by

$$F = \sum_i |c_i(t)|^2 \nabla_R \epsilon_i + \sum_{i<j} 2Re\{c_i^*(t)c_j(t)\} d_{ij}^{(1)} [\epsilon_j - \epsilon_i] \tag{2.40}$$

Ehrenfest dynamics is quite appropriate for nanostructures, such as quantum dots, nanotubes and the other systems with weak correlations of nuclear motion and electronic states, in which nuclei are heavy and the range of their motion is minimal. Attempt to address the loss of electron-nuclear correlation in Ehrenfest method, Tully developed surface hopping scheme, where nuclei propagates on a single electron PES[78], as in the case of BOMD. But the classical trajectory has a finite probability to hop to another PES. In general, the hopping probability is design to maintain the equality between population and the actual number of trajectories on the surfaces[106]. However, this approach introduces an excessive number of hopping events, eventually becoming mean-field PES which is inadequate to describe the chemical processes involving different reaction pathways. Fewest-switches surface hopping (FSSH) method is an effective way to keep the balance between accuracy and the fewest number of hops[78]. FSSH hopping probability is given by

$$P_{i\rightarrow j}(t) = max\left[0, -\frac{\delta t \frac{2}{\hbar} Re\left[c_i^*(t) * c_j(t)\left[d_{ij}^{(1)}\dot{R}\right]\right]}{c_i c_i^*}\right] \tag{2.41}$$

in which δt is the evolution time step. The propagation of electronic wavefunction follows the same equation of motion (Eq.2.37) as that in Ehrenfest dynamics. Hopping proceeds as follows: (1) The hop probability to all included states are determined, if the probability is negative, the probability is set to zero. (2) A random number is created to compare to hop probability to determine the occurrence of hopping. (3) When the hopping occurs, the nuclear moving velocity $\dot{R}$ is adjusted along the direction of NACs d_{ij} to conserve total energy. The key to the success of the surface hopping method is including strong electron-nuclear dynamics, beyond mean-field method. Surface hopping method preforms much more excellently in describing the photoisomerization, like photochemistry, than that in Ehrenfest method.

Chapter 3

Electric field tunable ultrafast interlayer charge transfer in graphene/WS_2 heterostructure

Vertical vdW heterostructures have attracted extensive attractions due to their excellent electrical and optical properties. In this chapter, we investigate the ultrafast interlayer charge transfer in graphene/WS_2 heterostructure via non-adiabatic molecular dynamics (NAMD) calculations. Our results indicate that photo-excited holes transfer from graphene to WS_2 is two times faster than that of electrons. This interlayer charge transfer is related to the nuclear vibration of graphene and WS_2, which can be manipulated by external electric fields. It is further demonstrated that carrier transfer rate at heterointerfaces is determined by the coupling between donor and acceptor states, which is the result of the competition between interlayer and intralayer relaxation process. These results provide insights into understanding of ultrafast carrier dynamics in vdW heterostructures and broaden their future applications in photovoltaic and optoelectronic devices.

3.1 Introduction

VdW heterostructures have attracted extensive attention due to their potential applications in areas of electronic, photonics and renewable energies, etc[107, 108]. The newly developed graphene/TMDC heterostructures with superior light-absorption properties of TMDCs [109] and high electrical conductivity of graphene [110, 111] have been taken as candidate materials for novel optoelectronic devices[112–114]. Enormous experimental and theoretical efforts have been devoted to study ultrafast carrier dynamics at graphene/TMDC heterointerfaces[115–121]. It is reported that the lifetime of photo-excited electrons is ∼1 ps in graphene/$MoSe_2$ heterostructure[122]. Similar results are observed in graphene/WS_2 heterostructure, in which interlayer hole transfer takes place less than 200 fs, an order magnitude faster than that of electron[123–125]. However, the origin of ultrafast interlayer charge transfer in weak coupling graphene/TMDC heterostructures is still unclear.

From the perspective of practical applications, applying with external electric fields has been taken as one of the most effective methods to improve performances of TMDCs due to their nondestructive and reversible nature[126–128]. Electric field tunable electrical and optical properties have been demonstrated in graphene/WSe_2 heterostructure[50]. In the case of optoelectronics, it has been reported that external electric fields can be used to manipulate the amplitude and even reverse the polarity of photo-induced current in graphene/MoS_2/graphene device[129]. Similarly, the gate-tunable photo-induced current is also observed in graphene/WS_2/graphene heterostructure[130]. Meanwhile, graphene/WS_2/graphene stack also exhibits outstanding performances in photoresponse, which is achieved by the modulation of the Schottky barriers between graphene and WS_2 with a gate voltage[131]. Although many experimental efforts have been made to promote performance of graphene/TMDC heterostructures in optoelectronics via the manipulation of heterointerfacial carrier dynamics, the mechanism of these microscopic processes remains uncertain.

In this chapter, we utilize TDDFT combined with NAMD method to investigate the ultrafast charge dynamics in graphene/WS_2 heterostructure. The results show that interlayer hole transfer is more efficient than electrons. This ultrafast carrier dynamics is attributed by phonon modes of graphene and WS_2, and its amplitude and polarity show a strong dependence on external electric fields. Detailed analysis indicates that interlayer charge transfer process in graphene/WS_2 heterostructure is

governed by the coupling between carriers and their final states, in other words, it is the result of the competition between carrier interlayer and intralayer relaxation processes. Further calculations demonstrate that nuclear vibrations in graphene and WS_2 enhance the interlayer couplings and favor the ultrafast interlayer charge transfer after excitation. This work establishes a firm correlation between the charge dynamics and couplings between states in vdW heterostructures, which broaden their applications in optoelectronics.

3.2 Computational details

First-principles calculations of graphene/WS_2 heterostructure are performed with linear combination of atomic orbital methods implemented in SIESTA[132] with Perdew-Burke-Ernzerhof (PBE) exchange-correlation functional[133, 134]. Troullier-Martins norm-conserving pseudopotentials [135] are employed to describe the core electrons. An orthogonal 5×5 graphene/4×4 WS_2 supercell is fully relaxed until the residual forces are less than 5×10^{-3} eV/Å and the total energy variation is less than 10^{-6} eV with vdW-DF2 functional[136]. The optimized lattice parameters are a = 12.433 Å and b = 21.524 Å, corresponding to 0.6% stretch of graphene and 1.7% compression of WS_2. The Brillouin Zone is sampled by 5×5×1 k-mesh grid with a 250 Ry energy cutoff for the orthogonal supercell to obtain electronic structures. A 30 Å vacuum layer is employed to avoid the interactions between repeated images.

The electron and nuclei dynamics are simulated within TDAP code[137]. Core electron are described by the same pseudopotentials[135] and exchange-correlation functional is PBE functional[133, 134]. The orthogonal supercell is sampled at Γ point and the system evolves with a 0.02419 fs time step. Initial ionic velocities are determined by the equilibrium Boltzmann-Maxwell distribution at a given 300 K.

3.3 Results and discussion

3.3.1 Excitation carrier dynamics

To investigate the photo-induced carrier dynamics at graphene/WS_2 heterointerface, a 5×5 graphene/4×4 WS_2 supercell is built, as shown in Figure 3.1(A). Due to the weak vdW interaction, the electronic structures are essentially superposition

of individual band structures of graphene and WS_2. As shown in Figure 3.1(D), Dirac point of graphene is located ∼34 meV below the Fermi level with a negligible bandgap of 4.3 meV. On the other hand, WS_2 remains a direct bandgap with a value of 2.04 eV at K point, with VBM 1.11 eV below E_F and CBM 0.93 eV above E_F. These results are consistent with angle-resolved photoemission spectroscopy (ARPES) measurements, where VBM is 1.20 eV below E_F[123]. The wave functions of VBM and CBM also indicate that the weak vdW interactions indeed have minor influence on the electronic structures (Figure 3.1(B) and (C)). The microscopic processes upon photoexcitation are presented in Figure 3.1(E), an electron-hole pair are generated in WS_2 layer with the energy of the bandgap, in which an electron is moved from VBM to CBM, and consequently hole and electron both transfer to nearby graphene states.

To quantify the charge transfer process, the amount of hole and electron transferred from WS_2 to graphene is calculated by integrating the carrier density over the whole graphene layer

$$n_i(t) = \sum_{\mu,\nu \in graphene} c^*_{\mu i}(t) S_{\mu\nu} c_{\nu i}(t) \tag{3.1}$$

where c is the molecular orbital coefficient, and S is the overlap matrix. μ and ν are the atomic orbitals belong to graphene, and i represents the hole or electron orbital. As shown in Figure 3.2(A), $n_h(t)$ oscillates periodically by filling and emptying graphene states with a period of ∼35 fs, and a gradual accumulation of hole (∼0.3) on the graphene layer is observed within first 100 fs. Meanwhile, $n_e(t)$ shows a relatively slow but steadily increasing trend, with ∼0.15 electron transferring to graphene layer in the same time period. Our calculations are in accordance with reported experimental measurements, in which photoexcited holes transfer to graphene more efficiently than electrons, with lifetime of ∼200 fs for hole and ∼ 1 ps for electron, respectively[115, 125]. Aeschlimann *et al.* attributed this difference to the energetic alignment of the heterostructure, in which p-doped graphene has about 6 times more acceptor states for hole transfer than that of electron transfer[123]. However, in this work, pristine graphene is employed and the density of acceptor states for electron and hole are closed (Figure A.1). Therefore, there must be other factors related to faster hole interlayer transfer process. As shown in Figure 3.2(D), acceptor states on graphene layer locate between hole and electron orbitals. As the system propagating, both hole and electron orbitals get closer to their acceptor states. As a result, hole orbital and its acceptor states on graphene overlap at ∼15 fs, while this occurs at a later time ∼25 fs for electron orbital. This overlap promotes the

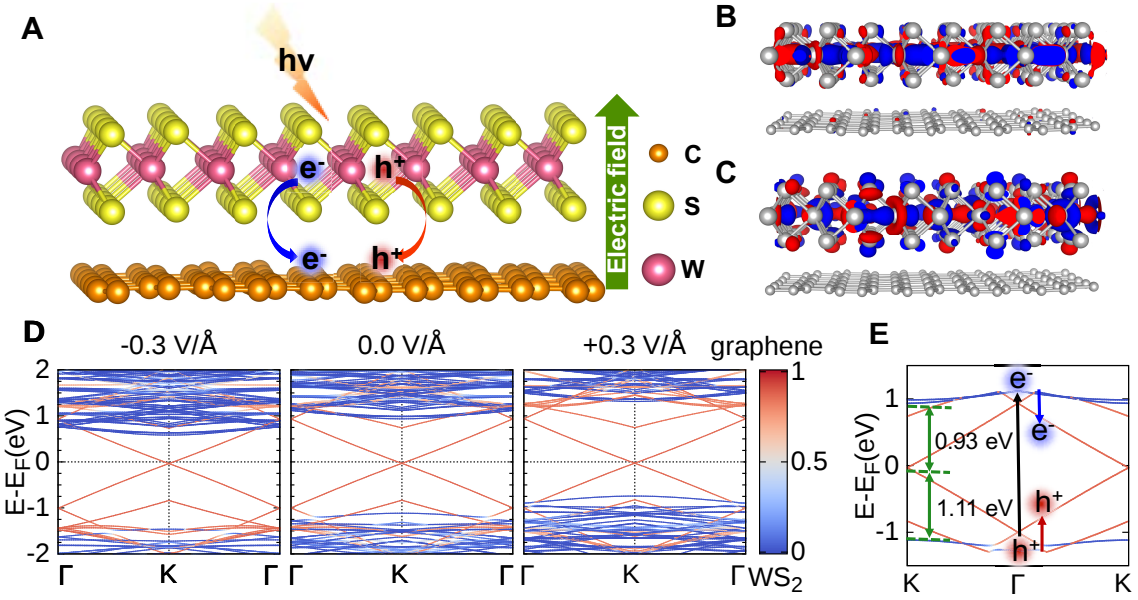

Figure 3.1: Electronic structures of graphene/WS_2 heterostructure. (A) Illustration of the graphene/WS_2 heterostructure, where WS_2 lies on top of graphene. Hole and electron excited by incident light transfer from WS_2 to graphene layer. The brown, yellow and purple spheres represent carbon, sulfur and tungsten atoms, respectively. The green arrow represents positive electric field direction, pointing from graphene to WS_2. Wave function of (B) VBM and (C) CBM states of WS_2 on $\Gamma-$point, positive and negative parts are in red and blue, respectively. The same crystal structure as Figure 3.1D is employed. To highlight the wavefunction, all atoms are represented by grey spheres. (D) The band structures of the heterostructure with different external electric fields varying from -0.3 V/Å to +0.3 V/Å. Fermi energies (E_F) are set to zero. The color of each band indicates the degree of localization of each state to graphene and WS_2, where one (red) represents that the state completely localizes to graphene, while zero (blue) represents that the state completely localizes to WS_2. (E) Band structures in the vicinity of $\Gamma-$point with zero external field to illustrate the photoexcitation process. Incident light excites one electron from the VBM of WS_2 to its CBM, as indicated by black arrow. The photoexcited hole and electron are then transferred to nearby graphene states, as indicated by red and blue arrows. The color map is the same as in Figure 3.1D.

coupling between donor and acceptor states, leading to an ultrafast interlayer charge transfer to graphene. These results imply that the faster interlayer hole transfer is determined by the stronger coupling. To quantify the coupling between donor and acceptor states, time-dependent density matrix is projected onto initial eigenstates

$$\sigma_{ij}(t) = \sum_{\mu\nu\kappa\lambda} (c_{\mu i}(0) S_{\kappa\mu})^* P_{\kappa\lambda}(t) S_{\lambda\nu} c_{\nu j}(0) \tag{3.2}$$

where c is the molecular orbital coefficient and μ, ν, κ, λ are atomic orbitals. The overlap matrix S and single-electron density matrix P are in non-orthogonal atomic basis representation. The summation in the above equation runs over all atomic orbitals. i and j are the eigenstates at t=0.

As shown in Figure 3.3, σ is divided into sub-blocks labelled by the layer number L_n, and each sub-block contains all the eigenstates localized on the layer. The diagonal element σ_{ii} (yellow block) represents the occupation of the state i, and the off-diagonal element σ_{ij} (green block) represents the coupling between states i and j. The coupling between i and states on the layer of interest is then obtained by summing over all the off-diagonal elements within L_n,

$$\tau_{i,L_n}(t) = \sum_{j \neq i, j \epsilon L_n} |\sigma_{ij}(t)| \tag{3.3}$$

for example, the red block represents the coupling between state i and all states on layer L_1, denoted by τ_{i,L_1}. Similarly, τ_{i,L_2} (blue block) is the coupling between state i and all states on layer L_2. In this work, the total coupling is obtained by summing over the states from $h-5$ to $e+5$ within the layer of interest $\tau_{i,L}(t) = \sum_{j\neq i, j=h-5}^{e+5} |\sigma_{ij}(t)|$, while L represents graphene (G) or WS_2 (W).

As shown in Figure 3.2(E) hole orbital couples stronger to the states on graphene while electron orbital couples stronger to the states on WS_2. Precisely, time-averaged value of $\tau_{h,G}(t)$ is $\sim$0.27, which is two times larger than that of $\tau_{h,W}(t)$ ($\sim$0.14). This is consistent with the tunneling model, in which the interlayer charge transfer is determined by the direct tunneling at points in Brillouin Zone where graphen and WS_2 bands cross[124]. The tunneling matrix elements for hole is much larger than that for electron. Thus, despite of weak binding of heterostructures, photoexcited hole interlayer transfer happens on an ultrafast timescale. In contrast, larger $\tau_{e,W}(t)$ drives electron intralayer relaxation within WS_2 layer more efficient. These results are further demonstrated by defining the charge localization

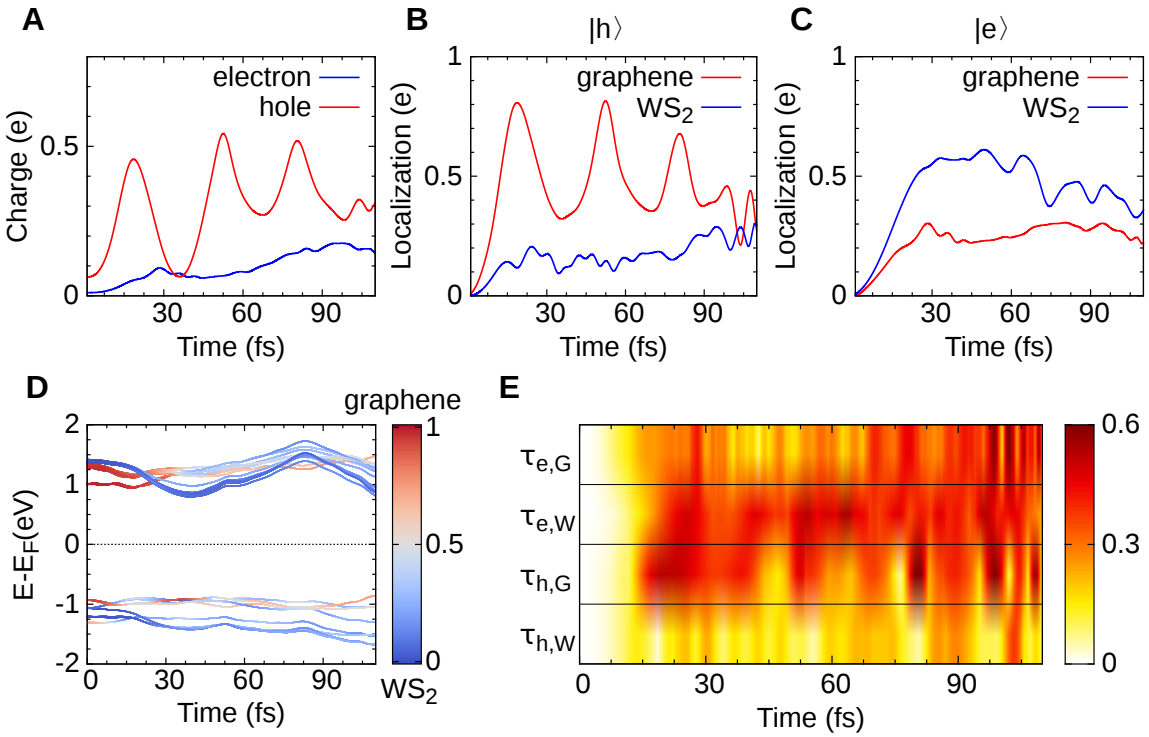

Figure 3.2: Excitation dynamics of graphene/WS_2 heterostructure. (A) Amount of photoexcited hole and electron transferred from WS_2 to graphene. The electron and hole transfer are shown in blue and red, respectively as a function of time. Time-evolution of photoexcited (B) hole and (C) electron localization $\gamma_{e/h}(t)$ on graphene and WS_2 layers. (D) Time-evolution of energy levels $\epsilon(t)$. Same color map as the Figure 3.1D is employed to show the charge localization. (E) Time-evolution of the couplings, $\tau_{e,G}(t)$, $\tau_{e,W}(t)$, $\tau_{h,G}(t)$ and $\tau_{h,W}(t)$. The color indicates the strength of the coupling between photoexcited carriers and acceptor states.

$$\gamma_h(t) = \sum_{j\neq h, j=h-5}^{e+5} |\langle j(0)|h(t)\rangle|^2, \qquad \gamma_e(t) = \sum_{j\neq h, j=h-5}^{e+5} |\langle j(0)|e(t)\rangle|^2 \tag{3.4}$$

Consistently with our previous results, Figure 3.2(B) and (C) present that excited hole delocalizes more rapidly to graphene due to the stronger coupling $\tau_{h,G}(t)$. While a large proportion of excited electron remains localized on WS_2 due to the more efficient intralayer relaxation. In other words, there is a competition between interlayer and intralayer carrier relaxation pathways, which is determined by the coupling $\tau_{e/h,L}(t)$. Next, we investigate how the carrier dynamics is influenced by the nuclear degrees of freedom in graphene/TMDC heterostructrues.

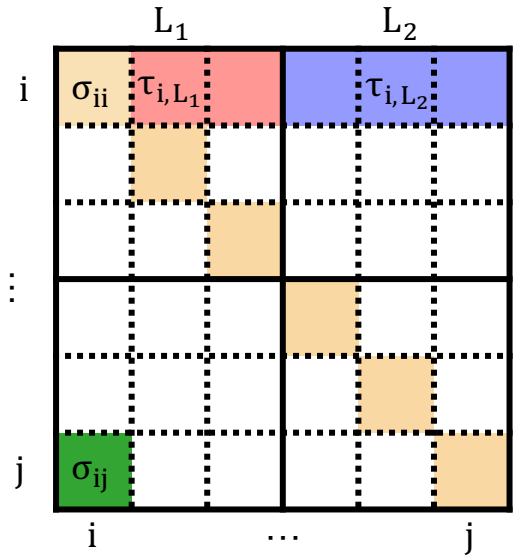

Figure 3.3: Illustration of the coupling matrix. σ is divided into sub-blocks according to different layers (solid lines), and the sub-blocks are further divided into eigenstates within the layer (dashed lines). The diagonal element σ_{ii}, shaded by yellow, represents the occupation of state i. The off-diagonal element σ_{ij}, shaded by green, represents the coupling between states i and j. Summing up all the off-diagonal elements within the layer L_1 (red shaded area) or L_2 (blue shaded area) gives the coupling between state i and all states on layer L_1 or L_2, denoted by τ_{i,L_1} or τ_{i,L_2} respectively.

3.3.2 The role of phonon modes in heterointerfacial carrier dynamics

To demonstrate the role of nuclear vibration in heterointerfacial carrier dynamics, FTs of $n_{e/h}(t)$, $\epsilon_{e/h}(t)$ and $\tau_{e/h}(t)$ are performed. As shown in Figure 3.4, hole transfer displays characteristic frequencies at ∼1067 cm^{-1} and ∼1584 cm^{-1}. The oscillation at ∼1067 cm^{-1} can also be found in the FTs of $\epsilon_h(t)$ as grey highlighted area in Figure 3.4(A). The ∼1584 cm^{-1} frequency (Figure 3.4(A), red shaded area) reflects the C=C stretching mode G[138], which can also be observed in the dynamics of $n_e(t)$ (Figure 3.4(B), red shaded area). For electron dynamics, apart from G mode, a noticeable peak at ∼413 cm^{-1} (Figure 3.4(B), left red shaded area) is found in FTs of $\epsilon_e(t)$ and $\tau_{e,G}(t)$, corresponding to the out-of-plane vibrational mode A_{1g} of WS_2[139]. In addition, the oscillatory component at ∼620 cm^{-1} (Figure 3.4(B),

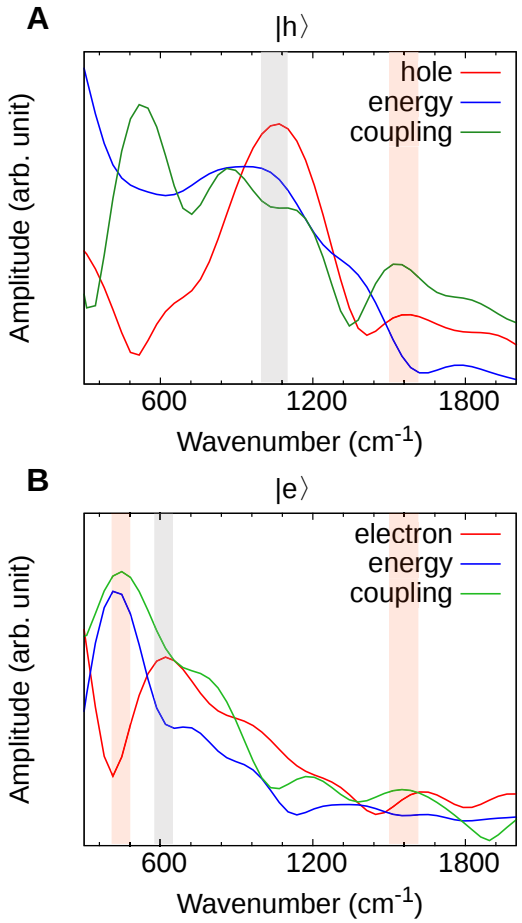

Figure 3.4: Comparison of FTs of photoexcited (A) hole and (B) electron transferred to graphene $n_{e/h}(t)$, their corresponding energies $\epsilon_{e/h}(t)$ and the couplings to electronic states of graphene layer $\tau_{e/h,G}(t)$. Red, blue and green curves correspond to the FTs of $n_{e/h}(t)$, $\epsilon_{e/h}(t)$ and $\tau_{e/h,G}(t)$, respectively. The red shaded areas highlight the frequencies associated with ionic vibrations, and the grey shaded areas represent the frequencies associated with the collective motion of carriers.

grey shaded area) are not associated with any phonon modes of graphene or WS_2. Therefore, it is expected that C=C stretching G mode is responsible for both interlayer hole and electron transfer while out-of-plane A_{1g} mode instead is related to interlayer electron transfer only.

To better understand the relationship between phonon modes and interlayer charge dynamics, the scenarios of fixed nuclear motions are investigated. We decouple the nuclear motion from the charge dynamics by freezing atoms in (i) both layers, in (ii) WS_2 layer only and (iii) graphene only, and excitation dynamic are displayed in

Figure 3.5. With all atoms clamped, the charge dynamics $n_i(t)$ presents two main features. On the one hand, for excited hole, a periodic sloshing between graphene and WS_2 with a prominent amplitude is observed, but there is no net hole on graphene within this period. On the other hand, the electron transfer is totally suppressed. These results further demonstrate that nuclear vibration is responsible for interlayer charge transfer in graphene/WS_2 heterostructure, in which the energy of carriers is dissipated by phonons during transition. Corresponding FTs of $n_{e/h}(t)$, $\epsilon_{e/h}(t)$ and $\tau_{e/h,G}(t)$ are presented in Figure 3.6. The excited hole and electron dynamics exhibit a distinct oscillation at $\sim$1100 cm^{-1} and $\sim$657 cm^{-1}, which is corresponding to the above frequencies at $\sim$1067 cm^{-1} and $\sim$620 cm^{-1} in the case with moving atoms. This is the same as that in MoS_2/WS_2 heterostructure, where hole dynamics present a similar oscillation when all atoms clamped. Wang *et al.* attributed the origin of this coherent oscillation by the collective motion of holes, which leads to strong dynamics coupling owing to the electric fields caused by charge transfer[140]. Therefore, the characteristic oscillation of charge dynamics derives from the collective motion of carriers. From Figure 3.5(C), there is no coupling between excited electron and graphene acceptor states, with a time-averaged value of 0.01. Instead, electron orbital couples more strongly to WS_2 states, with a time-averaged value of 0.32. As a results, excited hole fills and empties periodically the nearby graphene states, while a large majority of excited electron resides on WS_2 layer but relaxes to neighboring WS_2 states (Figure 3.7).

We further investigate the scenario when only atoms in WS_2 layer are clamped. Similarly, stronger couplings between excited hole and graphene states drive hole filling and emptying periodically nearby graphene states, but with a net amount of 0.2 hole transferred to graphene layer after 100 fs. Meanwhile, 0.1 electron gradually builds up on graphene layer within the same period. The carrier transfer rate is reduced by half compared with the case with moving atoms. For the case of frozen graphene, electron dynamics presents a similar trend as fixed WS_2, but no net hole transfer is observed within 100 fs. The excitation dynamics with clamped graphene and WS_2 layers in frequency domain is presented in Figure 3.8. When atoms in WS_2 layer are clamped, photoexcited hole and electron dynamics exhibit characteristic oscillation of the C=C stretching mode G, shaded by red areas in Figure 3.8(A). In contrast, the out-of-plane vibration A_{1g} [139] of WS_2 only contributes to the electron interlayer transfer. As showed in Figure 3.8(B), A_{1g}-mode (shaded by red area) can only be observed in electron dynamics when atoms in graphene are fixed. These

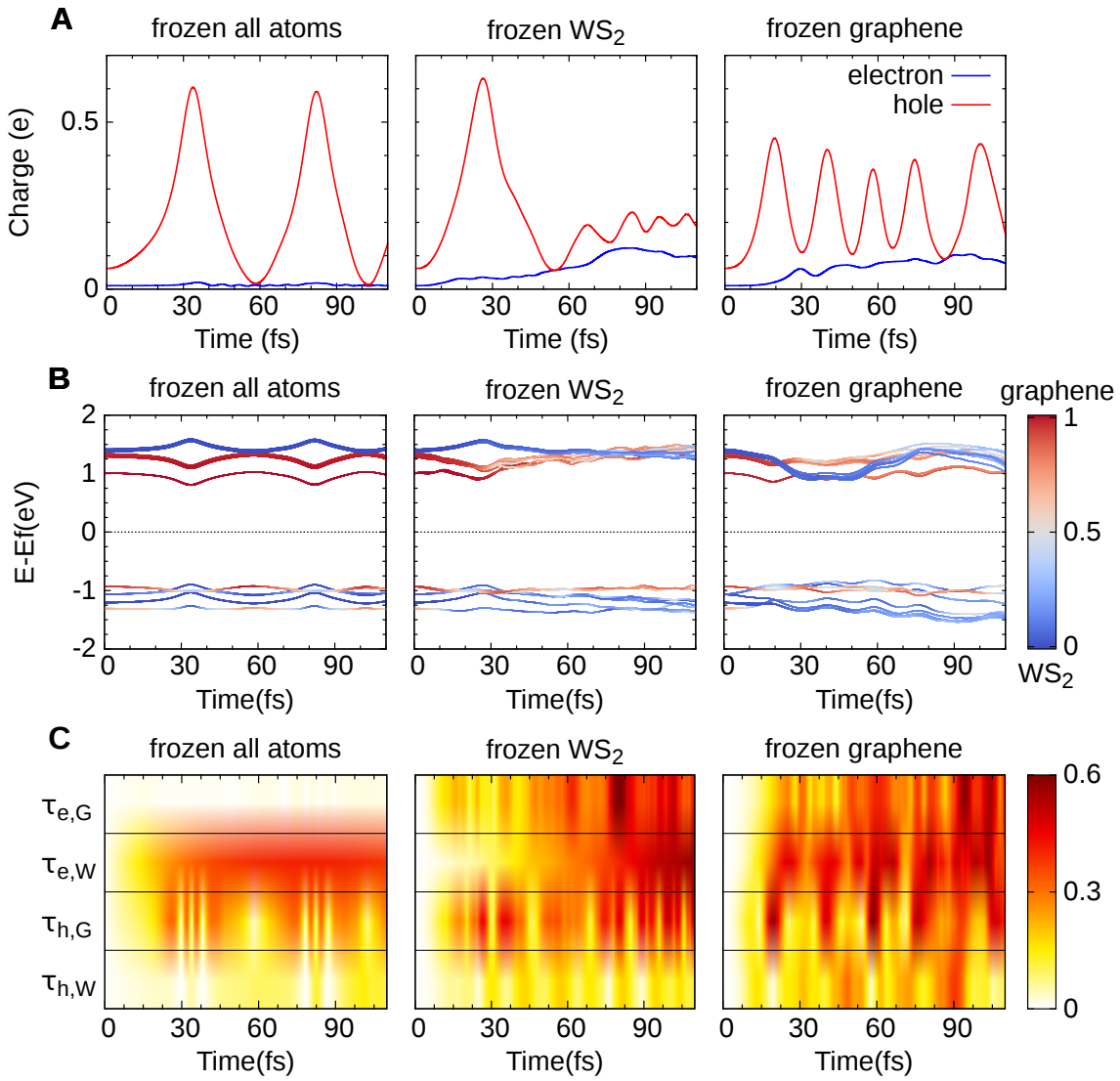

Figure 3.5: Excitation dynamics of graphene/WS_2 heterostructure with all frozen atoms, frozen WS_2 layer and frozen graphene layer. (A) Amount of photoexcited electron and hole transferred from WS_2 to graphene. (B) Time-evolution of the energy levels $\epsilon(t)$. The same color map as the Figure 3.1D is employed to show the charge localization. (C) Time-evolution of the couplings, $\tau_{e,G}(t)$, $\tau_{e,W}(t)$, $\tau_{h,G}(t)$ and $\tau_{h,W}(t)$. The color indicates the strength of the coupling between photoexcited carriers and acceptor states.

results imply that vibration of graphene is associated to electron and hole interlayer transfer process while vibration of WS_2 only contributes to electron interlayer dynamics. This is also in accordance with the excited hole and electron orbital spatial

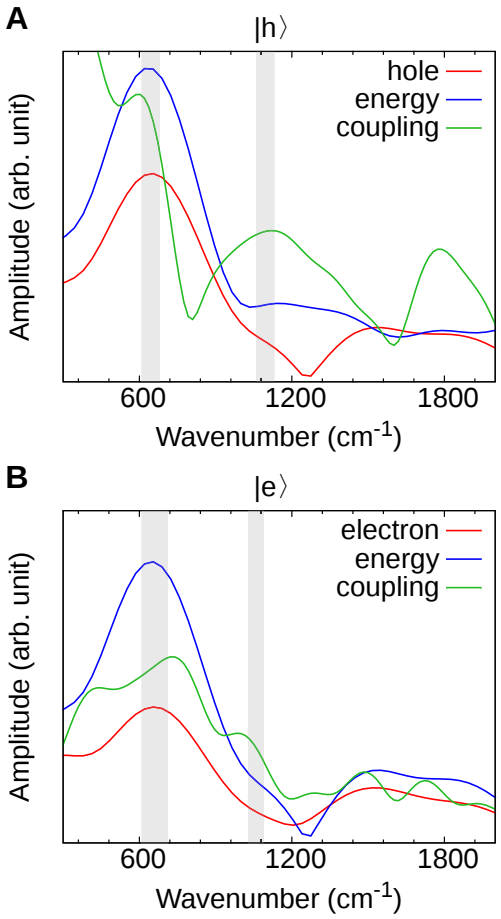

Figure 3.6: Comparison of FTs of photoexcited (A) hole and (B) electron transferred to graphene $n_{e/h}(t)$, their corresponding energies $\epsilon_{e/h}(t)$ and the coupling to electronic states of graphene layer $\tau_{e/h,G}(t)$ with all frozen atoms. Red, blue and green curves correspond to the FTs of $n_{e/h}(t)$, $\epsilon_{e/h}(t)$ and $\tau_{e/h,G}(t)$, respectively. The grey shaded areas represent the frequencies associated with the collective motion of carriers.

distribution, where excited hole distributes over the whole sandwich structure of WS_2 while excited electron is largely localized on W atoms (Figure 3.1(B)-(C)).

3.3.3 Electric field tunable carrier dynamics

In recent few years, intensive experimental research focuses on electric field tunable interlayer carrier relaxation dynamics at graphene/TMDC heterointerfaces. For example, built-in potential induced by gate-tunable Schottky barrier can acceler-

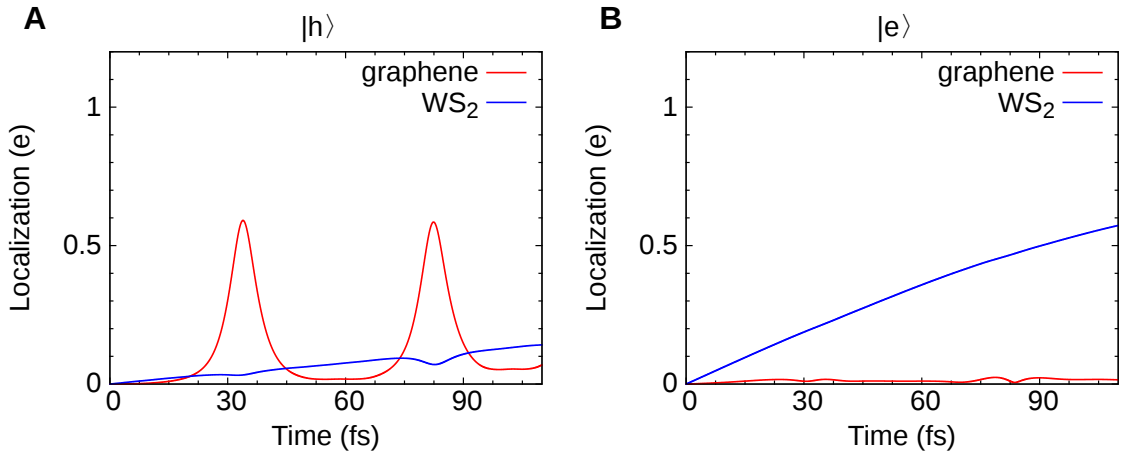

Figure 3.7: The Time-evolution of photoexcited (A) hole and (B) electron localization on graphene and WS_2 with all frozen atoms.

ate interlayer charge transfer in graphen/MoS_2, even achieving the modulation of amplitude and polarity of photocurrent[129]. As aforementioned, the observed ultrafast interlayer charge transfer is the result of the competition between interlayer and intralayer relaxation which is determined by the corresponding coupling. Thus, the couplings $\tau_{e/h,L}(t)$ and external electric fields are the keys to manipulate the heterointerfacial carrier dynamics. Vertical external electric fields are applied to heterostructure, ranging from -0.3 V/Å to +0.3 V/Å. As shown in Figure 3.1(D), electric fields have negligible effect on the electronic structures of graphene, but shift energy states of WS_2. Negative electric field downshifts WS_2 states by 0.4 eV, increasing acceptor states for hole transfer but decreasing acceptor states for electron transfer (Figure A.1). In contrast, positive electric field upshifts WS_2 states by 0.4 eV, which favors the electron interlayer transfer but prevents hole transfer. As shown in Figure 3.9(A), negative electric field indeed accelerates interlayer hole transfer with ∼0.35 of hole transferred to graphene at first 100 fs, which is faster than the case without electric field. But interlayer electron transfer is completely impeded. On the contrary, positive electric field promotes interlayer electron transfer, in which 0.25 of electron is delocalized to graphene within 100 fs, compared to the amount of ∼0.15 in the case without electric field. These results are consistent with experimental observation in graphene/MoS_2/graphene, in which -6 V top-gate bias enhances photoexcited hole transfer to top graphene while +4 V bias reverse the polarity of photocurrent via electron transferred to top graphene[129].

To further explore the origin of electric field tunable interlayer relaxation process,

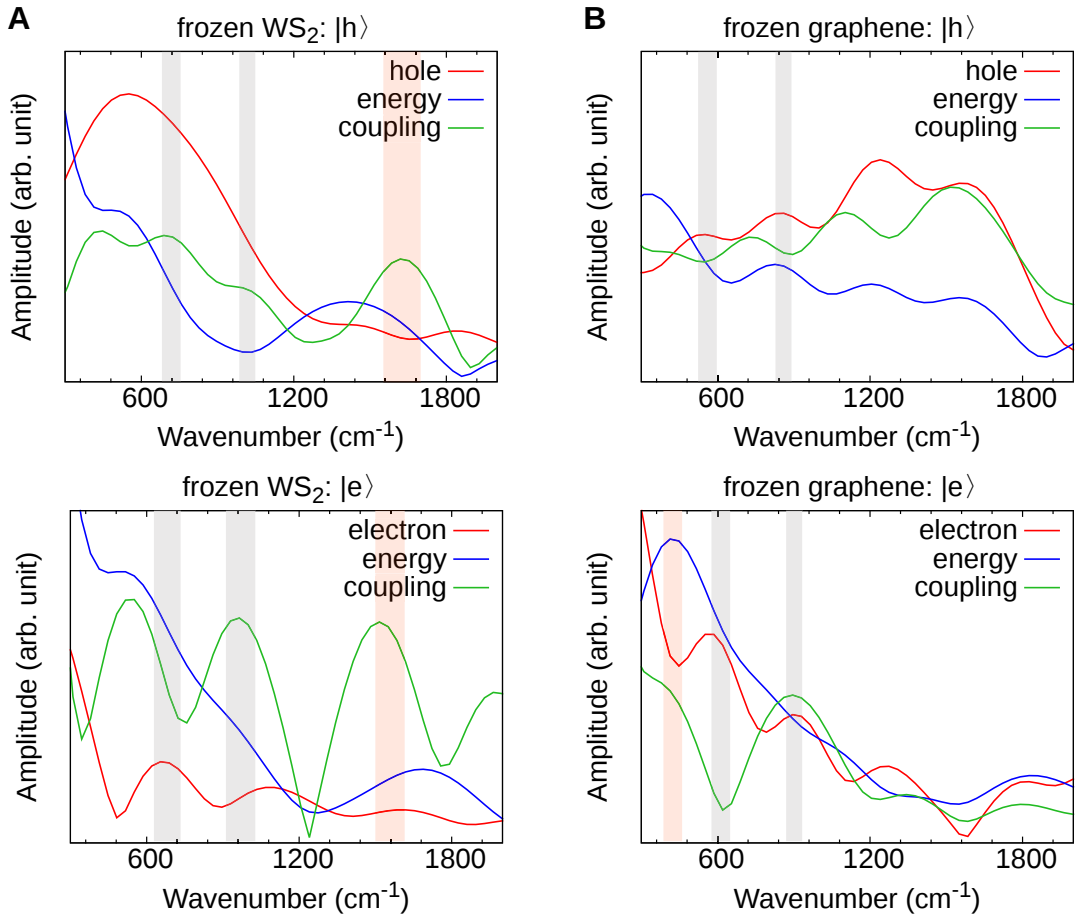

Figure 3.8: Comparison of FTs of photoexcited hole and electron transfer to graphene $n_{e/h}(t)$, their corresponding energies $\epsilon_{e/h}(t)$ and the coupling to electronic states of graphene layer $\tau_{e/h,G}(t)$ with (A) frozen WS_2 layer and (B) frozen graphene layer. Red, blue and green curves correspond to the FTs of $n_{e/h}(t)$, $\epsilon_{e/h}(t)$ and $\tau_{e/h,G}(t)$, respectively. The red shaded areas represent the frequencies associated with ionic vibrations, and grey shaded areas represent the frequencies associated with the collective motion of carriers.

we present the time-evolution of energy levels and corresponding couplings $\tau_{e/h,L}(t)$ in Figure 3.9(B)-(C). Since negative electric field introduces more acceptor states for hole transfer, $\tau_{h,G}(t)$ is enhanced and significantly accelerates interlayer hole transfer. Positive electric field has the same effect on acceptor states for electron transfer and thus stronger $\tau_{e,G}(t)$ facilitates the interlayer electron transfer. Comparing the couplings in Figure 3.9(C) with that in Figure 3.2(E), external electric fields indeed have significantly effects on the coupling between donor and acceptor states and

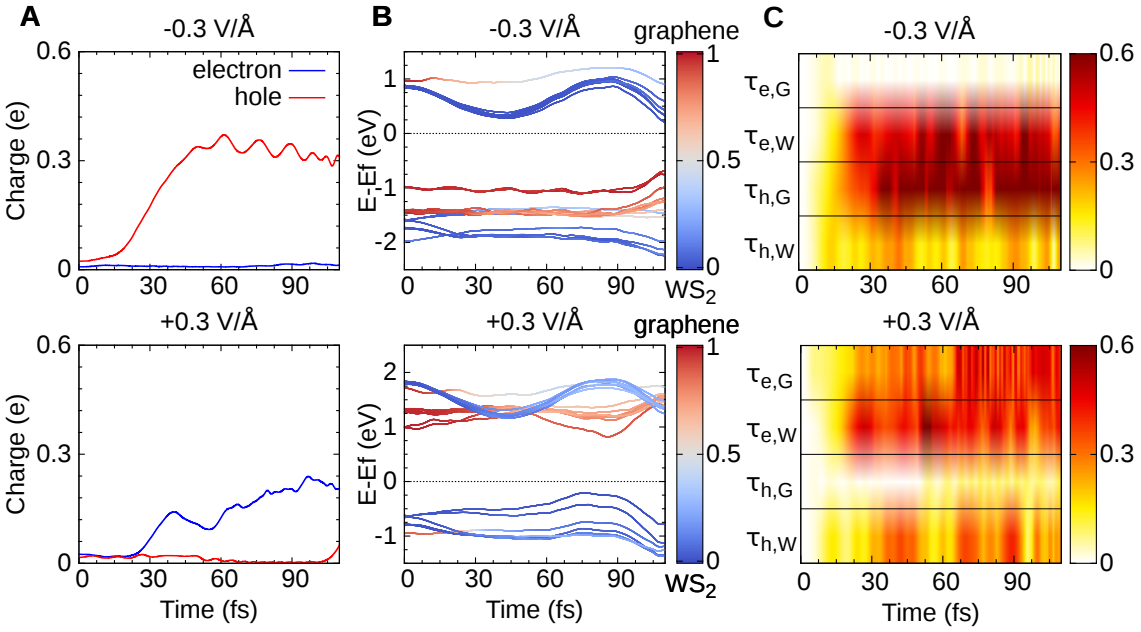

Figure 3.9: Excitation dynamics of graphene/WS_2 heterostructure with external electric fields varying from -0.3 V/Å to +0.3 V/Å. (A) Amount of photoexcited electron and hole transferred from WS_2 to graphene. (B) Time-evolution of the energy levels $\epsilon(t)$. Same color map as the Figure 3.1D is employed to show the charge localization. (C)Time-evolution of the couplings, $\tau_{e,G}(t)$, $\tau_{e,W}(t)$, $\tau_{h,G}(t)$ and $\tau_{h,W}(t)$. The color indicates the strength of the coupling between photoexcited carriers and acceptor states.

hence interlayer charge transfer rate. The scenario with ±0.1 V/Å electric fields are presented in Figure 3.10, the charge dynamics exhibits the same response to external electric fields. As shown in Figure A.2, +0.1V/Å electronic field increases the electron acceptor states, while -0.1V/Å electric field increases hole acceptor states. Consequently, +0.1V/Å electric field boosters $\tau_{h,G}(t)$, accelerating interlayer hole transfer, while -0.1V/Å electric field improves $\tau_{e,G}(t)$, stimulating interlayer electron transfer. Thus, it is possible to control interlayer charge transfer rate selectively via external electric fields, and therefore separate the photo-generated carriers. These results provide a versatile strategy to manipulate the photoexcited carrier generation, separation and transport process in graphene/TMDC heterostructures.

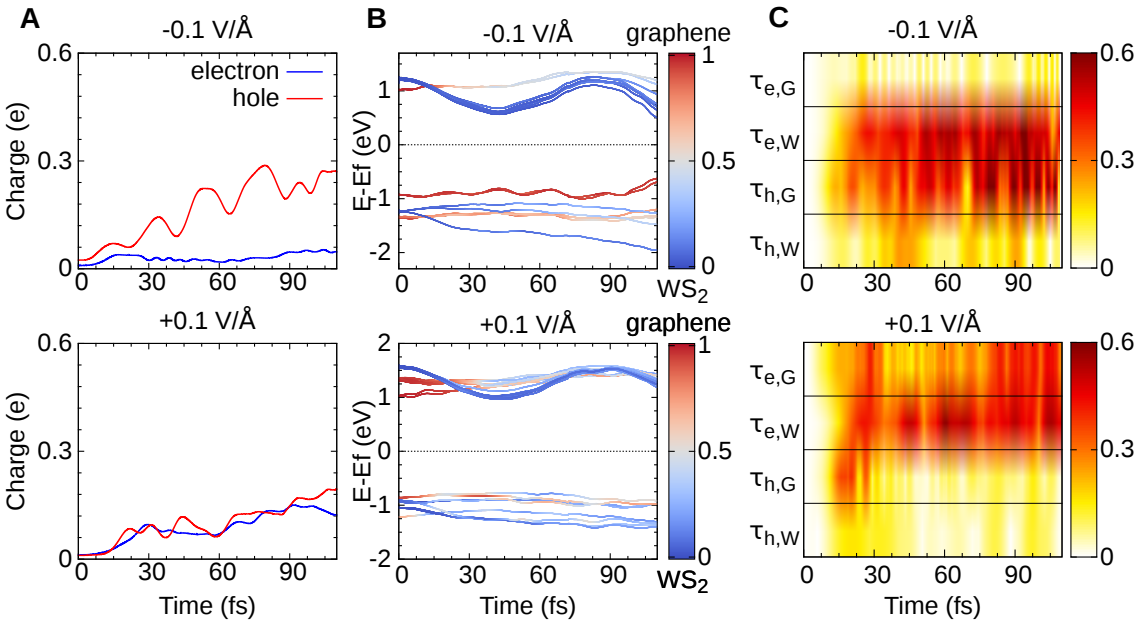

Figure 3.10: Excitation dynamics of graphene/WS_2 heterostructure with external electric fields varying from -0.1 V/Å to +0.1 V/Å. (A) Amount of photoexcited electron and hole transferred from WS_2 to graphene. (B) Time-evolution of the energy levels $\epsilon(t)$. Same color map as the Figure 1D is employed to show the charge localization. (C)Time-evolution of the couplings, $\tau_{e,G}(t)$, $\tau_{e,W}(t)$, $\tau_{h,G}(t)$ and $\tau_{h,W}(t)$. The color indicates the strength of the coupling between photoexcited carriers and acceptor states.

3.4 Conclusion

In summary, we employ TDDFT-NAMD method to investigate the ultrafast interlayer charge transfer process in graphene/WS_2 heterostructure. Our study reveals that interlayer charge dynamics is determined by the coupling between donor and acceptor states, which is the origin of different transfer rates of excited hole and electron in heterostructure. Meanwhile, it is found that phonon modes of graphene and WS_2 are related to the interlayer coupling and then facilitate the interlayer charge transfer. Specially, C=C stretching G-mode is associated with both interlayer hole and electron transfer process, while out-of-plane A_{1g}-mode only contributes to interlayer electron transfer. Moreover, we demonstrate the possibility of electric field modulation of the interlayer couplings and the control of carrier dynamics. Based on these findings, we could utilize the external electric fields to manipulate the ex-

cited carrier dynamics at vdW heterointerfaces. These results not only provide a deep understanding of heterointerfacial phenomena, but also offer new insights for constructing ultrasensitive optoelectronic devices.

Chapter 4

Carrier multiplication in transition metal dichalcogenides beyond threshold limit

Carrier multiplication (CM) is a process whereby absorption of a single photon creates multiple electron-hole pairs. Current state-of-the-art nanomaterials including quantum dots and carbon nanotubes have been demonstrated CM, but not satisfactory due to the high threshold energy and inherent difficulties with carrier extraction. In the chapter, we report CM in monolayer TMDCs MX_2 (M = Mo, W; X= S, Se, Te). Surprisingly, the threshold energy of CM in monolayer TMDCs can be effectively modulated by nuclear vibrational modes. EPC could induce significant changes in electronic structures, even lead to semiconductor-to-metal transition, and eventually reduce the threshold energy of CM to less than twice bandgap ($2E_g$). The stronger EPC drives CM process dominating the carrier relaxation dynamics after photo excitation, achieving a higher conversion efficiency η_{CM}. Our results show that the strongest EPC in monolayer MoS_2 results in the highest η_{CM} when the carriers with the same excess energy in six monolayer TMDCs. Further analysis indicates that chalcogen vacancies also lower the threshold energy of CM via defect states among the bandgap. Especially, for monolayer WS_2 with a bandgap of 1.95 eV, sulfur vacancies reduce the onset energy of CM to $1.51E_g$. These results identify TMDCs as promising candidate materials for efficient optoelectronic devices with combination of high photoconductivity and phonon-assisted tunable CM characteristics.

4.1 Introduction

Exciting semiconductors with photon energies exceeding their bandgap creates electron-hole pairs which can be collected to produce an electric current. When the excess energy of photoexcited carriers is higher than E_g, carriers obtain sufficient energy to excite another pair of electron-hole, which is known as CM. Beard *et al.* predicted that CM characteristics could overcome Schokley-Queisser limit and raise solar efficiency up to ∼46%[51]. Due to energy conservation limit and phonon-assisted energy dissipation, the threshold energy of CM should be closed to around $2E_g$ ∼$2.5E_g$ for maximal use of solar energy[141]. However, in bulk semiconductor, the relatively weak Coulomb interactions and momentum conservation constraints limit the threshold energy as high as ∼$6E_g$[52], which is impractical for applications. Meanwhile, phonon scattering act as a competing pathway for excited carriers in bulk semiconductors, which efficiently dissipates the excess energy. Eventually, CM is rarely realized in photovoltaic devices based on traditional bulk materials. In contrast, CM performance can be promoted in nanostructures, in which quantum confinement relaxes the strict momentum conservation requirements and phonon bottleneck impedes phonon emission[53, 142–144]. It has been reported that CM threshold energy in bulk PbSe is as high as $4.5E_g$[52] whereas it is substantially reduced to $3E_g$[141] in corresponding quantum dots and $2.2E_g$[145] in nanorods. Recently, CM phenomenon is observed in 2D TMDC films of 2H-$MoTe_2$ and 2H-WSe_2 with threshold energy as low as $2E_g$, and conversion efficiency can reach up to nearly 99%[62, 63]. These performances are superior to those previously reported nanostructure materials[64–66, 146–148]. To further optimize materials for photovoltaic applications, it is meaningful to explore if the threshold energy limit can be overcome.

Layered TMDC materials, represented by MX_2 (M=Mo, W; X= S, Se, Te), are intensively investigated due to their fascinating properties. MX_2 exhibits indirect-to-direct bandgap transition when exfoliated from bulk to monolayer[149, 150]. Meanwhile, the weak vdW interaction between individual layers allows easy formation of multiple layered heterostructures[151], which permits further tuning of material properties. MX_2 also presents distinctive electrical and optical properties. It has been demonstrated that carrier mobility in monolayer MoS_2 is at least 200 $cm^2V^{-1}s^{-1}$ at room temperature, similar to graphene nanoribbons[152]. In particular, the mobility in WSe_2 can reach up to 500 $cm^2V^{-1}s^{-1}$ which is comparable to the best performance of single silicon crystal[5, 153]. In addition, the absorption

of sunlight in monolayer MX_2 is typically 5-10%[154, 155], an order of magnitude larger than that in common photovoltaic materials[156]. Thus, exceptional mechanical flexibility, bandgap tunability, high carrier mobility, efficient sunlight absorption, together with the CM characteristics, render TMDCs as promising candidate materials for highly efficient next-generation solar cells.

In this chapter, we combine NAMD with rt-TDDFT to investigate the CM characteristics in various monolayer TMDCs. CM phenomenon is observed in all six monolayer TMDCs, with threshold energy as low as $1.75E_g$ caused by the couplings to phonons. It is found that nuclear vibrations introduce significant changes in electronic structures, which favors CM and overshadows the phonon-assisted energy dissipation pathways. This leads the onset of CM with excitation energy lower than $2E_g$. When the excess energy is the same in the six monolayer TMDCs, MoS_2 with the strongest EPC achieves the highest CM conversion efficiency η_{CM}. Meanwhile, chalcogen vacancy, as a common defect in TMDCs, can also improve CM efficiency by scattering electrons from valence bands to defect states. Particularly, sulfur vacancies reduce the threshold energy to $1.51E_g$ in monolayer WS_2. This work demonstrates the role of phonon modes in CM process, and provide insights into the design strategy to break CM threshold limit in TMDCs via phonon and defect engineering.

4.2 Computational details

First-principles simulations of monolayer TMDCs are performed with linear combination of atomic orbital methods implemented in SIESTA[132]. The core electrons are described by Troullier-Martins norm-conserving pseudopotentials[135]. The nonlocal exchange and correlation energies are treated with PBE functional[133, 134]. The structure is fully relaxed until the total energy variation is less than 10^{-6} eV and the residue forces are less than 5×10^{-3} eV/Å. The Brillouin Zone of unit cell is sampled by a 15 × 15 × 1 k-mesh grid with a 250 Ry energy cutoff to obtain electronic structures. A 30 Å vacuum layer is employed to avoid the repeat image interactions. NAMD simulations are calculated based on TDDFT using the TDAP code[137] with a time step of 0.02419 fs. The $3\sqrt{3} \times 3\sqrt{3}$ supercell is sampled at Γ point, and the initial ion velocities are obtained by the equilibrium Boltzmann-Maxwell distribution at a given temperature 300K.

The calculations of EPC parameters λ is based on DFT implemented in SIESTA

[132] together with INELEASTICA [157]. In the limitation of low temperature, phonon absorption is suppressed and Eliashberg function α^2F is written as

$$\alpha^2 F^E_{n\mathbf{k}}(\omega) = \sum_{\nu\mathbf{q}} \sum_{n'} |g^{\nu}(n\mathbf{k}, n'\mathbf{k+q})|^2 \times \delta(\epsilon_{n'\mathbf{k+q}} - \epsilon_{n\mathbf{k}} - \hbar\omega_{\nu\mathbf{q}}) \delta(h\omega - h\omega_{\nu\mathbf{q}}) \quad (4.1)$$

where the summations include all electron scattering from $\epsilon_{n'\mathbf{k+q}}$ states to $\epsilon_{n\mathbf{k}}$ states with emission of a phonon with energy of $\hbar\omega_{\nu\mathbf{q}}$. This transition process is mediated by EPC matrix elements $g^{\nu}(n\mathbf{k}, n'\mathbf{k+q})$. The EPC parameter $\lambda_{n\mathbf{k}}$ is defined as

$$\lambda_{n\mathbf{k}} = 2 \int d\omega \frac{\alpha^2 F^E_{n\mathbf{k}}(\omega)}{\omega} \quad (4.2)$$

For monolayer TMDCs, VBM and CBM of monolayer TMDCs locate at **K** point, thus we consider **q** that is around **K**-point with a distance of 0.1Å^{-1} in reciprocal space to satisfy energy conservation.

4.3 Results and discussions

4.3.1 Carrier excitation dynamics

To investigate the CM phenomenon in monolayer $MoTe_2$, twelve electron-hole pairs are created by moving electrons from valence bands to conduction bands at 300K. The excitation energy is set as $\sim$2E$_g$, where hole and electron excess energy (ΔE$_h$ and ΔE$_e$) equal to 0.86E$_g$ and 0.14E$_g$, respectively. The excess energy is defined as the difference in the energy of carriers with respect to band edge. To quantify the efficiency of CM, we define the carrier generation QY as the number of electron-hole pairs produced per absorbed photon. Recently, remarkably efficient CM is observed in layered $MoTe_2$, in which the threshold energy is as low as 2E$_g$ with carrier generation QY=2[62, 63]. Ellingson *et al.* attributed the low threshold by the asymmetric transition where the total kinetic energy is resident on only one kind of carrier and is therefore sufficient to scatter additional electron-hole pair[144]. In principle, ΔE_h (0.86E$_g$) and ΔE_e (0.14E$_g$) are insufficient to excite another electron-hole pair across the bandgap. Surprisingly, Figure 4.1(A) shows that the amount of carriers keeps increasing upon excitation and carrier generation QY reaches $\sim$1.07 at 500 fs. The origin of the relatively low CM conversion efficiency in our calculations is as follows. Firstly, twelve electron-hole pairs are excited in monolayer $MoTe_2$, with a concentration of 3.58×10^{-14}cm^{-2} which is larger than that in experiment work. Thus, an

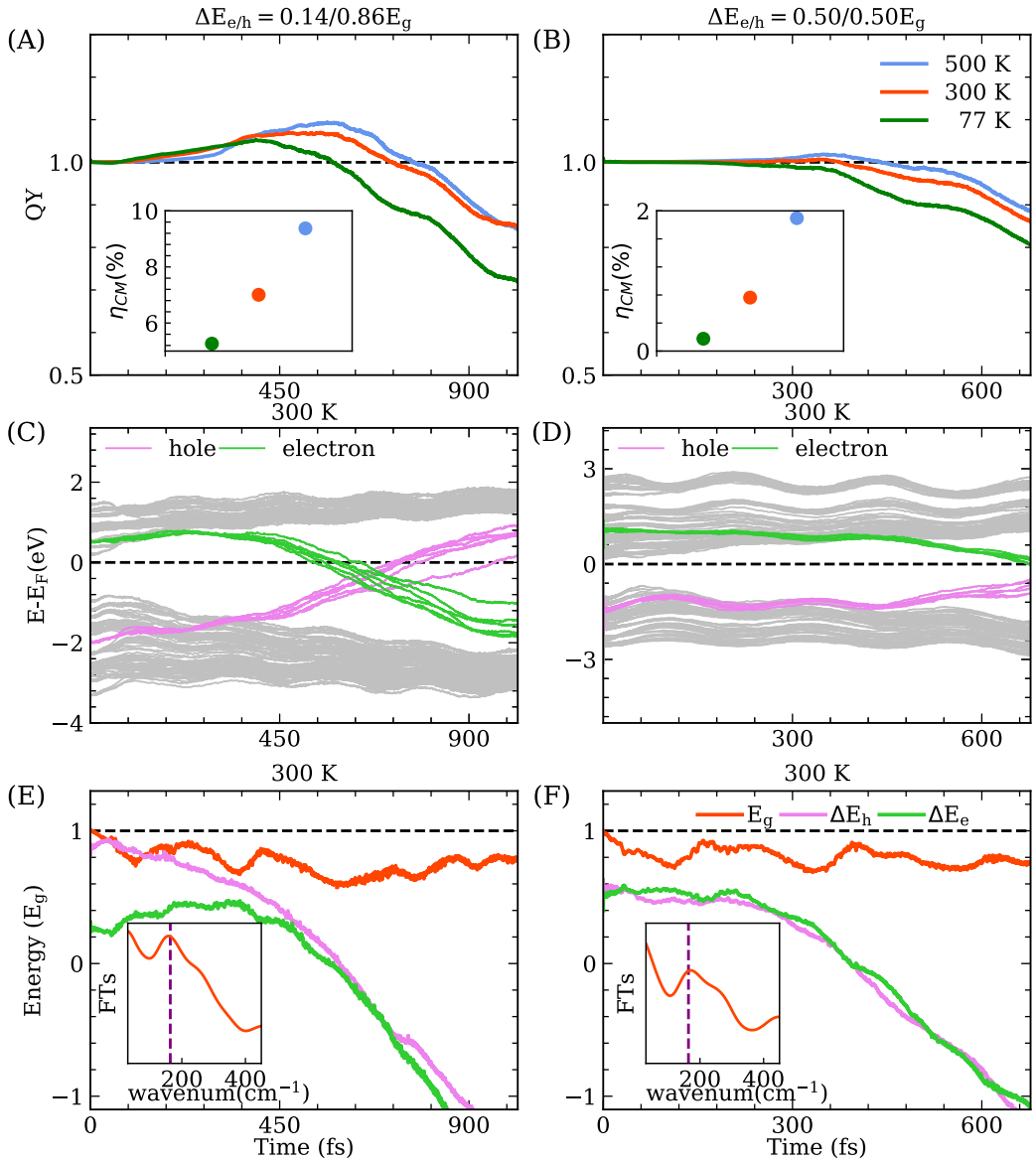

Figure 4.1: Excitation dynamics of monolayer $MoTe_2$ with different carrier excess energies at different temperatures. Electron-hole pairs are generated by photon with energy of $2E_g$ at temperature 77 K, 300 K and 500 K. The excess energies of carrier are $\Delta E_{e/h} = 0.14/0.86E_g$ (left panel) and $\Delta E_{e/h} = 0.5E_g/0.5E_g$ (right panel). (A)-(B) Carrier generation QY of CM in $MoTe_2$ as a function of time upon excitation. Inset: CM conversion efficiency at the three temperatures. (C)-(D) Time-evolution of energy states at 300 K. Purple and green lines are hole and electron states, respectively. The dashed lines show the Fermi level E_F. (E)-(F) $E_g(t)$ at 300 K is compared with the excess energy of hole ΔE_h and electron ΔE_e. The dashed lines represent the bandgap at $t = 0$ fs. Inset: FTs of time-dependent bandgap $E_g(t)$. Vertical dashed line represents phonon mode A' with vibrational frequency of 163.7 cm^{-1}

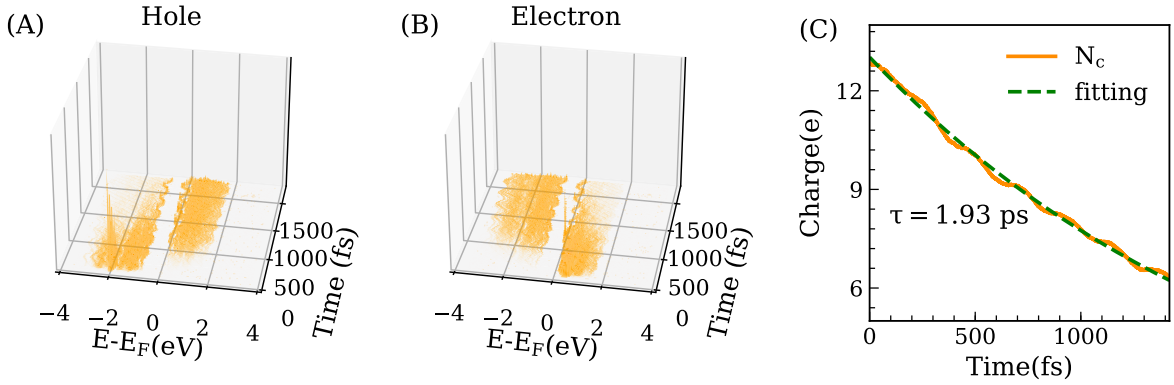

Figure 4.2: Excitation dynamics of monolayer $MoTe_2$. Twelve electron-hole pairs are excited with carrier excess energy of $\Delta E_{e/h}$=0.14/0.86E_g Density of excited (A) hole and (B) electron as a function of time and energy. (C) Decay dynamics of carrier after reaching maximum carrier generation. The carrier lifetime is fitted with an exponential function and lifetime is found to be 1.93 ps.

efficient Auger recombination becomes a competitive pathways for carrier relaxation. As shown in Figure 4.2(A)-(B), partial excited holes and electrons populate higher energy states, which is the fingerprint of Auger process. This decay dynamics can be fitted by exponential decay with a lifetime of ∼1.98 ps (Figure 4.2(C)), which can be attributed to Auger trapping free carriers with 1-2 ps time scale lifetime in TMDCs[158–161]. Meanwhile, surface/defect trapping which effectively competes with Auger process also make contributions to the higher conversion efficiency in experiments. Apart from Auger recombination, monolayer crystal structure accelerates charge carrier nonradiative recombination. As shown in Figure 4.2(A)-(B), excited holes partially occupy conduction band states while excited electrons populate valence band states, corresponding to the nonradiative recombination. Corresponding to Figure 4.1(C) that excited hole and electron both decay back to conduction bands and valence bands at ∼600 fs. To demonstrate above statements, the excitation dynamics of $MoTe_2$ with only one electron-hole pair is presented in Figure 4.3(A). With a lower carrier concentration, the lifetime of excited carriers becomes longer and carrier generation QY is raised to 2 and conversion efficiency η_{CM} reaches up to 100% which is consistent with the experimental observations[62, 63]. Obviously, Auger recombination and non-adiabatic recombination are impeded by the lower carrier concentration (Figure 4.3(B)-(C)).

To reveal the mechanism of CM in monolayer $MoTe_2$, time-evolution of bandgap

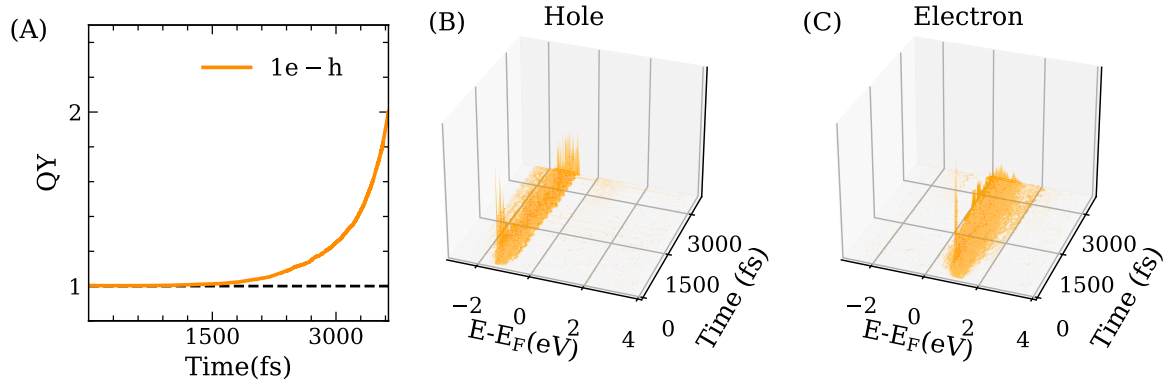

Figure 4.3: Excitation dynamics in monolayer $MoTe_2$. One electron-hole pair are generated, and carrier excess energy are distributed as $\Delta E_{e/h}$=0.14/0.86E_g. (A) Time-evolution of carrier generation QY. Density of excited (B) hole and (C) electron as a function of time and energy.

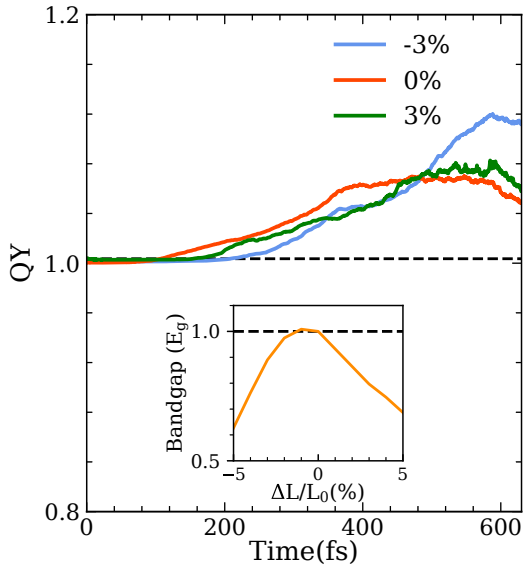

Figure 4.4: Excitation dynamics in monolayer $MoTe_2$ with applied strain. Electron-hole pairs are excited with carrier excess energy of $\Delta E_{e/h} = 0.14/0.86E_g$. Inset: The bandgap of monolayer $MoTe_2$ under tensile and compressive strain.

is plotted in Figure 4.1(E). Upon excitation, the bandgap of $MoTe_2$ oscillates periodically owing to the nuclear vibrations. Overall, the bandgap becomes narrower along the whole trajectory and even drops to 60% of its initial value, which enables excited holes have sufficient energy to excite additional electron-hole pair across the bandgap. Obviously, Figure 4.1(E) shows that $\Delta E_e(t)$ surpasses the bandgap at ∼50

fs, triggering CM. Previous research showed that tensile strain could lead to significant changes in electronic structure of monolayer TMDCs. This could even induce semiconductor-to-metal transition with deformation of ∼10%[162, 163]. Our calculations also indicate 3% of tensile and compressive strain could narrow bandgap by 20% (inset of Figure 4.4). In other words, besides energy dissipation, nuclear vibrations can also cause significant changes in electronic structures and carrier relaxation dynamics. To further investigate the influence of phonons on the bandgap, FTs of $E_g(t)$ is plotted in the inset of Figure 4.1(E). FTs displays a characteristic frequency at ∼163.7 cm^{-1} which is associated to the out-of-plane vibrational mode of tellurium atoms (A'). Therefore, it is expected that A'-mode of $MoTe_2$ has impressive effect on the bandgap. Thus, the resulting bandgap reduction favors CM process, especially when the excess energy of carriers $\Delta E_{e/h}$ is below the threshold limit.

4.3.2 Phonon-assisted CM beyond threshold limit

To better understand the role of phonon modes in CM process, nuclear vibrational modes of monolayer TMDC are calculated. The phonon dispersion of monolayer $MoTe_2$ and ionic vibrations of four optical phonon modes are presented in Figure 4.5. These vibrational frequencies are in accordance with previous studies[164, 165]. The effect of optical phonon modes on the bandgap is demonstrated in Figure 4.5(B), where we present the bandgap as a function of the displacement amplitude of these modes. Obviously, all four optical phonons narrow the bandgap of $MoTe_2$, the same phenomenon is also observed in other five TMDCs (Figure B.3-FigureB.7). The phonon-dependent bandgap in our calculations are consistent with the results calculated by hybrid HSE06 functional, in which the equibiaxial tensile strains can lead to phase transformation from semiconducting 2H phase to metallic 1T phase[162]. As mentioned above, our results also observe a narrower bandgap of monolayer $MoTe_2$ caused by strains (Inset of Figure 4.4). At room temperature, only A'-mode and E"-mode can be activated effectively based on Bose-Einstein distribution. Compared with A'-mode, E"-mode only reduces bandgap by 2%. Thus, the contribution of E"-mode is negligible, while A'-mode is responsible for the narrower bandgap at room temperature, which is consistent with the results in the inset of Figure 4.1(E). We further study the scenario where $MoTe_2$ is excited at different temperatures to identify the positive effect of EPC on CM process (Figure 4.1). Electron-hole pairs with energy of $2E_g$ are created at 77 K, 300 K and 500 K, respectively.

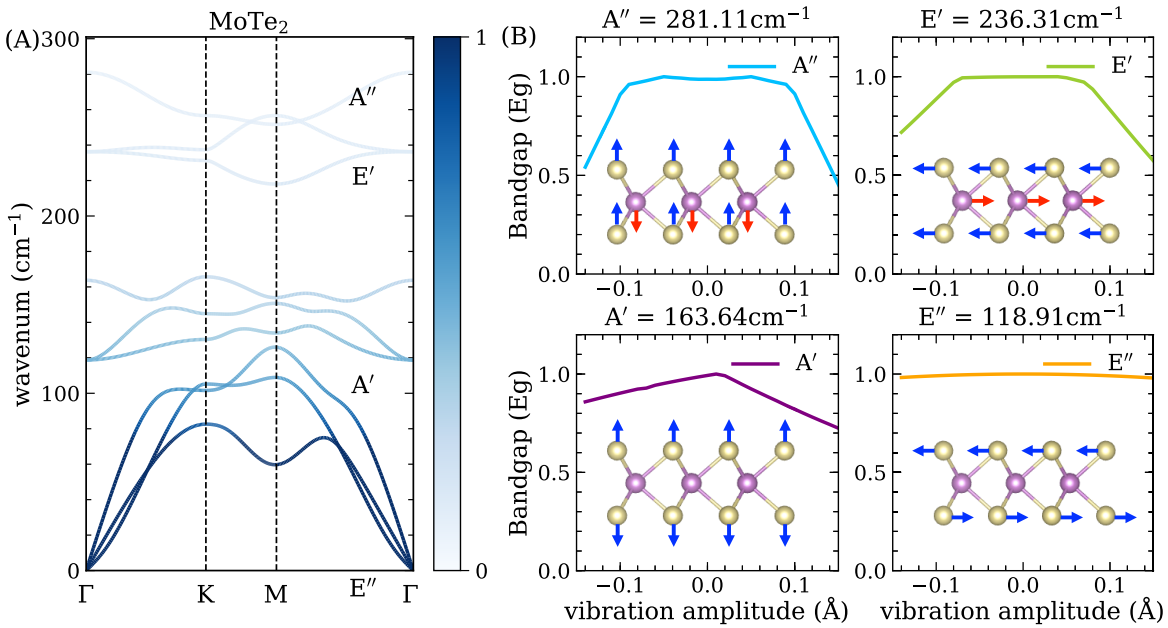

Figure 4.5: Lattice vibrational modes in monolayer $MoTe_2$. (A)Phonon dispersion of monolayer $MoTe_2$. The colormap indicates the phonon occupation number which is determined by the Bose-Einstein distribution at 300 K. (B) The bandgap as a function of the vibration amplitude of four optical phonon modes in monolayer $MoTe_2$. The inset shows vibrational modes of optical phonons at Γ point.

Here, we take account for two type of excitation: (i) asymmetric electron-hole pairs with ΔE_e=0.14E$_g$/ΔE_h=0.86E$_g$ and (ii) symmetric electron-hole pairs with ΔE_e=ΔE_h=0.50E$_g$. To facilitate our analysis, we quantify the CM conversion efficiency as follows

$$\eta_{CM} = \frac{\phi_{max} - 1}{\frac{h\nu}{E_g} - 1} \times 100\% \tag{4.3}$$

where ϕ_{max} is the maximum QY in the time-evolution process, and $h\nu$ is the energy of phonons. In previous works, it was reported that carrier relaxation pathways via phonons is the main channel for energy dissipation[141]. Therefore, it is generally anticipated that weakening EPC is a straightforward method to enhance η_{CM}. However, this viewpoint ignores the influence of nuclear motions on the bandgap. As shown in Figure 4.1(A), with phonon-induced narrower bandgap, CM phenomenon is observed even when the excess energy ΔE_h is only 0.86E$_g$. With a higher temperature, the vibration excursions of atoms are larger. Consequently, a higher carrier generation QY in $MoTe_2$ is achieved via a narrower bandgap. The CM conversion

efficiency η_{CM} is promoted from 5.26% to 9.37% when then temperature rising from 77 K to 500 K. Similarly, increasing temperature has the same effect on improving η_{CM} for the symmetric electron-hole pair excitation, as shown in Figure 4.1(B). Especially, at 77 K and 300 K, CM is not observed, and nonradiative recombination and Auger recombination dominate the carrier relaxation process. This can be explained by the fact that ΔE_h(t) and ΔE_e(t) are both below E_g(t) along the whole trajectory (Figure 4.1(F) and Figure C.2). As discussed above, the oscillation of E_g(t) is caused by A'-mode. However, at 77 K, only a few phonons are excited and E_g(t) keeps much larger than the excess energy of carriers. In contrast, at 500 K, intensive vibrations shrink the bandgap by ∼50% and trigger the onset of CM. To further demonstrate the role of bandgap in CM process, we also stimulate the carrier dynamics in monolayer $MoTe_2$ under ±3% strain. The inset of Figure 4.4 displays that the bandgap of monolayer decreases significantly under tensile and compressive strains, which is expected to stimulate CM efficiency. As shown in Figure 4.4, carrier generation QY is enhanced, +3% strain improve QY of CM slightly, with a value of ∼1.08. Particularly in the case with -3% strain, QY gives rise to ∼1.12, increased by nearly 30% compared with the case without strain. In this way, we present the possibility to reduce the threshold energy for CM in monolayer TMDCs.

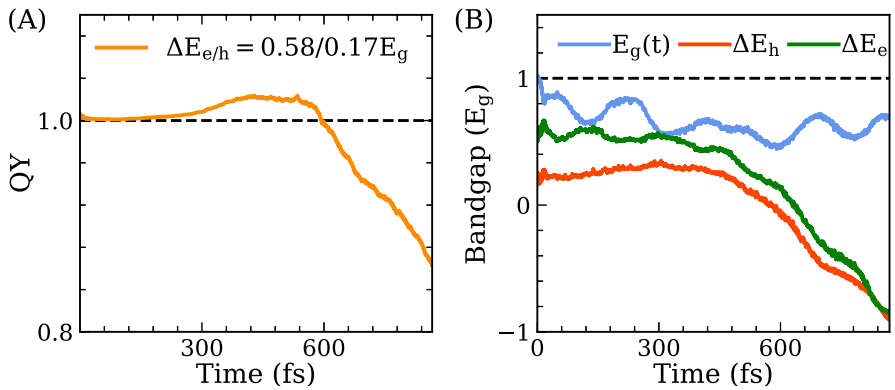

Figure 4.6: Excitation dynamics of monolayer $MoTe_2$ with excitation energy of $1.75E_g$. The hole and electron excess energies are $\Delta E_{e/h}$=0.58/0.17E_g. (A) Carrier generation QY as a function of time. (B) Time-evolution of bandgap $E_g(t)$, hole excess energy $\Delta E_h(t)$ and electron excess energy $\Delta E_e(t)$.

To examine the above mechanism, we excite $MoTe_2$ with energy of 1.75E_g at 300K. Precisely, ΔE_e and ΔE_h are 0.58E_g and 0.17E_g, respectively. As shown in Figure 4.6, CM is indeed observed after excitation, and CM conversion efficiency η_{CM} is ∼4%

at 500 fs. Figure 4.6(B) shows that phonon-induced reduction of bandgap is about $0.45E_g$, thus excited electrons have sufficient energy to scatter extra electrons across bandgap at ∼150 fs, resulting in CM. It is the first time that CM process occurs with excitation energy lower than $2E_g$, which implies that phonons have positive effect on CM process in monolayer TMDCs. Next, we further explore the possibility of phonon-assisted CM in other MX_2, and compare their conversion efficiency η_{CM}. The EPC parameter for electronic state $n\boldsymbol{k}$ is defined as

$$\lambda_{n\boldsymbol{k}} = 2\int d\omega \frac{\sum_{\nu\boldsymbol{q}}\sum_{n'}\left|g^{\nu}(n\boldsymbol{k}, n'\boldsymbol{k}+\boldsymbol{q})\right|^2 \times \delta(\epsilon_{n'\boldsymbol{k}+\boldsymbol{q}} - \epsilon_{n\boldsymbol{k}} - \hbar\omega_{\nu\boldsymbol{q}})\delta(\hbar\omega - \hbar\omega_{\nu\boldsymbol{q}})}{\omega} \tag{4.4}$$

where the summations over all electron scattering events from state $\epsilon_{n'\boldsymbol{k}+\boldsymbol{q}}$ to $\epsilon_{n\boldsymbol{k}}$ with the emission of a phonon with energy of $\hbar\omega_{\nu\boldsymbol{q}}$. Figure 4.7(B) displays the sum of EPC parameters of VBM and CBM at K-point ($\lambda = \lambda_{VBM\boldsymbol{K}} + \lambda_{CBM\boldsymbol{K}}$) in six monolayer MX_2, which is consistent with reported theoretical valued obtained by density functional perturbation theory[166]. Clearly, EPC parameters decrease with the atomic radii when the metal atoms changed from Mo to W and chalcogen atoms changed from Te to S. This can be explained by the reduced separation between atoms where the displacements of atoms have stronger influence on electronic interactions.

Table 4.1: Effective carrier excess energy ΔE_{eff} in six monolayer TMDCs

	WTe_2	$MoTe_2$	WSe_2	$MoSe_2$	WS_2	MoS_2
ΔE_{eff} (E_g)	0.73	0.76	0.69	0.65	0.66	0.65

To verify the relationship between η_{CM} and EPC parameters, six monolayer MX_2 are excited by the phonons with energy of $2E_g$, and the carrier excess energy are distributed as $\Delta E_{e/h} \sim 0.70/0.30E_g$ (or $\Delta E_{e/h}$ ∼$0.30/0.70E_g$). In this situation, the effective energy for CM is ∼$0.70E_g$, but the exact values of excess energy depend on the electronic structures of materials, given in Table4.1. From Figure 4.7(B), there is clear correlation between ϕ_{max} and λ in monolayer TMDCs. In other words, the stronger EPC, the more efficient CM. The strongest EPC in monolayer MoS_2 gives rise to about 7 times higher η_{CM} than that in WTe_2 with weakest EPC. Figure 4.7(C) and Figure 4.7(D) present the time-evolution of bandgap in each MX_2 upon excitation. Consistent with above results, monolayer MX_2 with stronger EPC indeed leads to an overall narrower average bandgap. Meanwhile, FTs of

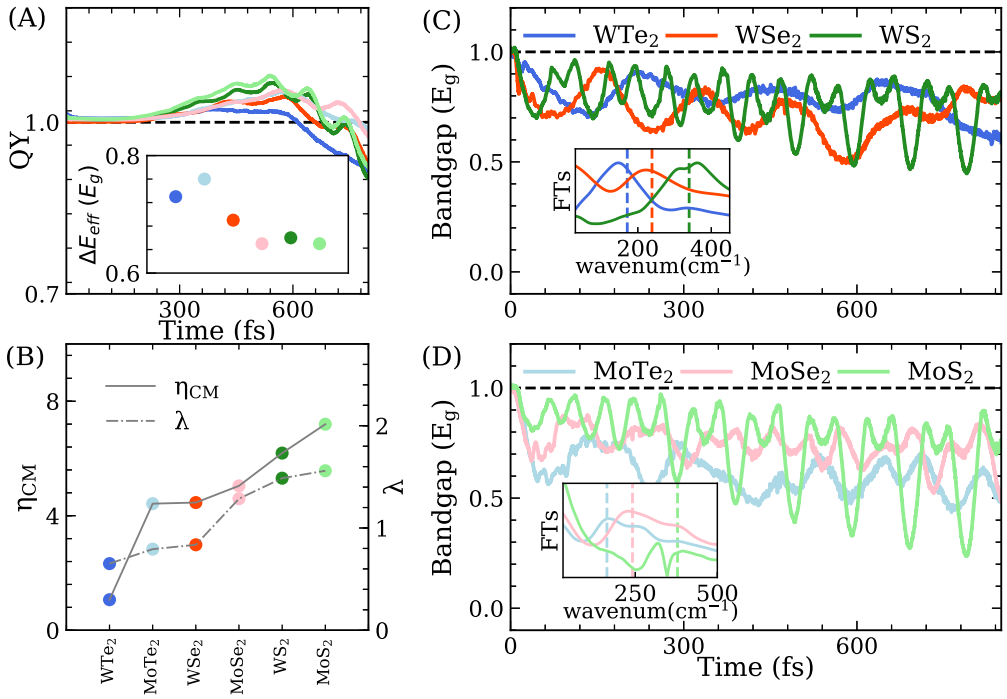

Figure 4.7: Excitation dynamics of the six monolayer TMDCs. Electron-hole pairs are excited with photon energy of $2E_g$, with excess energies distributed as $\Delta E_{e/h} \sim 0.7/0.3E_g$ (or $\sim 0.3/0.7E_g$). (A) Time-evolution of carrier generation QY of CM. The inset presents the effective carrier excess energy ΔE_{eff} in six monolayer TMDCs. (B) Comparison of CM conversion efficiency η_{CM} and EPC strengths λ in the six monolayer TMDCs. Time-evolution bandgap $E_g(t)$ of (C) WX_2 and (d) MoX_2 (X = S, Se, Te). Insets: FTs of $E_g(t)$. Colored dashed lines represent the frequencies of phonon mode A' in each TMDC.

bandgap also reveal the A'-mode characteristics, which further confirms the bandgap reduction and enhancement of CM are phonon-related.

4.3.3 Effect of defects on CM

Monolayer TMDCs, as light-absorbing materials for solar cells, their absorption should significantly overlaps with solar spectra, and therefore can be able to utilize the energy for carrier generation. As Beard *et al.* stated, the ideal bandgap of light-absorbing materials with CM characteristics for photovoltaics should be closed to 1.0 eV[51, 141]. Thus, it is essential to optimize CM threshold of TMDCs for better performance in photovoltaic devices. Defect engineering has been one of

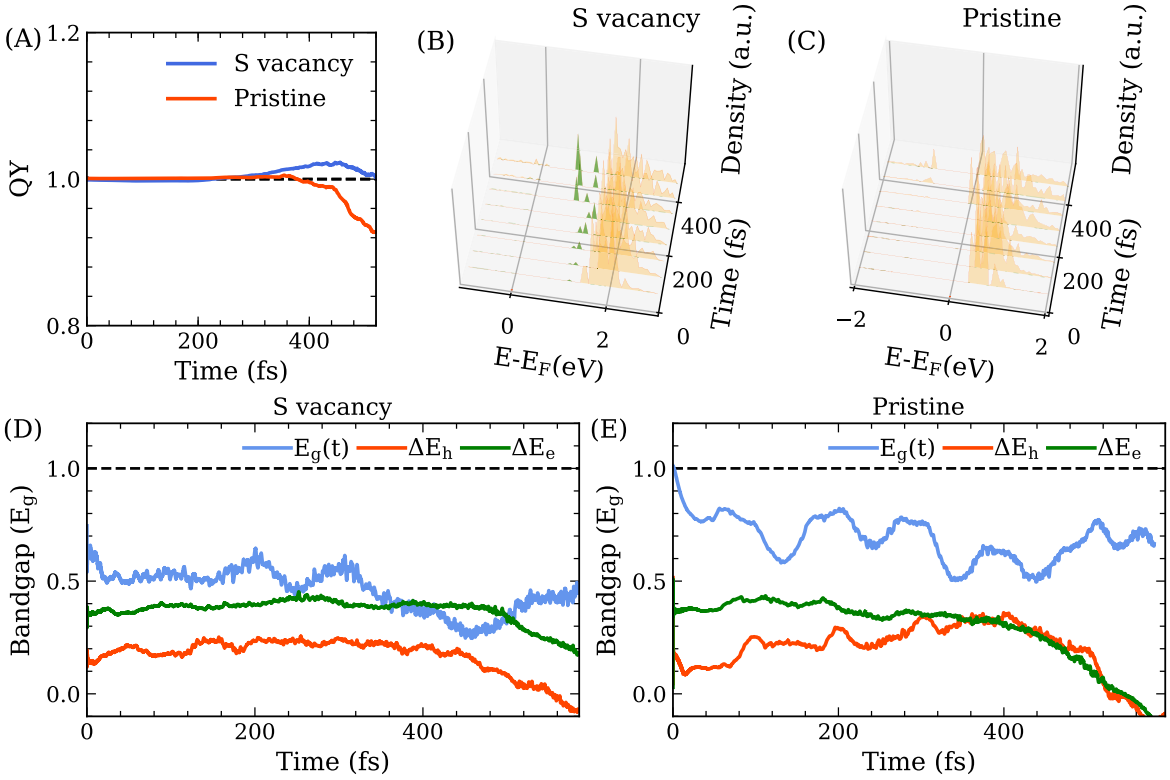

Figure 4.8: Excitation dynamics in monolayer pristine WS_2 and WS_2 with sulfur vacancy. Electron-hole pairs are excited with photon energy of $1.51E_g$, and carrier excess energies are distributed as $\Delta E_{e/h} = 0.36/0.15E_g$. (A) Time-evolution of carrier generation QY of CM. Density of excited electron as a function of time and energy in (B) WS_2 with sulfur vacancy and in (C) pristine WS_2. Green fillings in (B) represent the sulfur vacancy states in the conduction bands. Time-dependent bandgap $E_g(t)$, hole excess energy ΔE_h(t) and electron excess energy ΔE_e(t) in (D) WS_2 with sulfur vacancy and in (E) pristine WS_2.

key strategies of material design and defect-assisted CM had been previously reported in amorphous silicon[167]. Various defects and impurities are unavoidable during the processes of TMDCs. Among different defects, chalcogen vacancies are known to introduce sub-gap states[168], which provide possibilities to manipulate the threshold energy of CM. Therefore, sulfur vacancy is introduced to our monolayer WS_2 model, with a concentration of $3.66\times10^{13}\text{cm}^{-1}$. As shown in Figure C.3, sulfur vacancy introduces two defect states among bandgap, including a shallow hole trap state and a deep electron trap state. The hole trap state is 0.03 eV above VBM while electron trap state is 0.48 eV below CBM, resulting in the reduction

of bandgap by 0.51 eV. Electron-hole pairs are then excited with photon energy of $1.51E_g$ in pristine WS_2 and defective WS_2. The carrier excess energies are distributed as $\Delta E_{e/h}$=0.36/0.15E_g. Here, E_g corresponds to the bandgap of pristine WS_2. Figure 4.8(A) displays the time-evolution of QY upon excitation. Compared with pristine WS_2, sulfur vacancy indeed lowers the excitation energy to only $1.51E_g$ for CM to occur. As shown in Figure 4.8(C), for pristine WS_2, there are two major relaxation pathways for excited carriers. On the one hand, excited electrons transfer to higher energy states via Auger recombination. On the other hand, excited electrons decay to valence bands to recombine with excited holes nonradiatively. On the contrary, for defective WS_2, excited electrons with sufficient energy scatter extra electrons from valence bands to populate the defect states. This is in accordance with Figure 4.8(D) where ΔE_e(t) surpasses the bandgap at ∼250 fs and CM kicks in. In contrast, even with phonon-induced bandgap narrowing, the excess energy ΔE_e(t) is inadequate in pristine WS_2 to excite additional electron-hole pairs. Therefore, exciton relaxation dynamics is dictated by nonradiative recombination and Auger recombination only, shown in Figure 4.8(C) and (E) and Figure C.4(B). These results provide insights into the defect engineering for tailoring CM threshold energy to promote performance of TMDCs for photovoltaic devices.

4.4 Conclusion

In conclusion, with rt-TDDFT-NAMD method, we investigate CM phenomenon in monolayer TMDCs. Specifically, the role of lattice vibrations in the excited carrier dynamics is examined. It is found that the bandgap is reduced due to the coupling to out-of-plane A'-mode. Consequently, additional electron-hole pairs can be excited more effectively. In addition, we identify chalcogen vacancies can further enhance CM by introducing sub-gap defect states. Based on these findings, we show the possibility of triggering CM with below threshold limit in monolayer TMDCs. Thus, high conductivity, large absorbance and excellent CM characteristics enable monolayer TMDCs as promising materials for next-generation photovoltaic devices.

Chapter 5

Doping effect on carrier multiplication in graphene

CM, multiexciton generation by absorbing a single photon, is a promising strategy to improve photovoltaic devices performance. Graphene has emerged as a prospective CM candidate material due to its linear band structure, combined with strong electron-electron scattering and weak EPCs. Here, we report an effectively doping tunable CM in graphene. Theoretical simulations based on NAMD and rt-TDDFT method show that doping level can lead to remarkable differences in CM conversion efficiency. In n-doped graphene, the CM QY can be increased from 1.41 to 1.89 when the Fermi level rising from 0.40 eV to 0.78 eV via doping nitrogen atoms. Consistently, TR-ARPES measurements on n-doped graphene also indicate the same correlation between doping levels and the CM conversion efficiency. These results suggest that tuning doping levels is an effective strategy to manipulate the performance of graphene in optoelectronic devices.

5.1 Introduction

The vital goal in the field of optoelectronics is to explore materials which could convert light energy into electrical energy with high efficiency. Materials with CM characteristic, which generate multiple excitons via absorbing one photon, are prospective candidates for optoelectronic devices. Graphene has been considered as a potential photovoltaic material due to its unique electronic and optical properties, including high room-temperature carrier mobility and CM characteristic. CM performance is predicted to be particularly effective in graphene thanks to its linear band structure[55, 56], combined with slow electron-phonon cooling[57, 58] and strong electron-electron interaction[59, 60]. In the past few years, extensive theoretical and experimental efforts have been made to investigate the CM phenomenon in graphene[55, 169–171]. It is reported that CM conversion efficiency is highly sensitive to the location of Fermi level relative to the Dirac point via ultrafast cascade of impact excitation processes[61, 172]. Intriguingly, this observation indicates that doping levels can be used to manipulate CM characteristic in graphene, which can be easily tuned by gate voltages [173, 174] or intercalating different elements[175, 176]. However, the effect of doping level on CM in graphene is still under debate. On the one hand, impact excitation as scattering process result in a chain like cascade consisting of sequential steps with relatively small energy loss per step $\Delta\epsilon \sim E_F$, which indicates that carrier excess energies play a major role in CM conversion efficiency[61]. On the other hand, CM process is directly determined by the probability of excited carriers finding scattering partners in the Fermi sea. In other words, the larger phase space, the more efficient CM[171].

In this part, we investigate the effect of doping levels on CM in graphene based on NAMD with rt-TDDFT method. Our theoretical calculations show that CM QY in strongly n-doped graphene is significantly more efficient than that in slightly n-doped graphene. Especially, the CM QY is increased from 1.41 to 1.89 when the Fermi level rising from 0.40 eV to 0.78 eV. Consistently, experimental measurements via TR-ARPES also observe the same correlation between doping levels and CM conversion efficiency. It is found that CM QY can be promoted from 1.70 to 2.80 when the Fermi level increasing from 0.30 eV to 0.38 eV. It is further demonstrated that CM QY mainly depends on available phase space, strongly n-doped graphene provides a larger phase space which boosters electron-electron scattering to enhance CM conversion efficiency. These results provide a practical strategy to promote CM performance in graphene via doping levels, achieving high light energy to electrical

energy conversion efficiency in optoelectronic devices.

5.2 Methods

5.2.1 Computational Details

First-principles simulations of doped graphene are performed with DFT implemented in SIESTA[132]. Troullier-Martins norm-conserving pseudopotentials are employed to deal with the core electrons[135]. The structure is fully relaxed until the total energy variation is less than 10^{-6} eV and the residue forces are less than 5×10^{-3} eV/Å, with PBE exchange-correlation functional[133, 134]. The $6\sqrt{3}\times6\sqrt{3}$ supercell, with 216 atoms, is sampled by a $3 \times 3 \times 1$ k-mesh grid with a 250 Ry energy cutoff to simulate electronic structures. Two, four and six carbon atoms are replaced by nitrogen atoms respectively, leading to different doping levels. A 30 Å vacuum layer is employed to avoid the repeat image interactions. NAMD simulations are calculated with TDAP[137]. The supercell is sampled at Γ point with a time step of 0.02419 fs. The initial ion velocities are determined by the equilibrium Boltzmann-Maxwell distribution at 300K.

5.2.2 Experimental Methods

Epitaxial monolayer graphene grown on a 4H-SiC(0001) is initially prepared ex situ[177]. Before growing bismuth dopant, it is cleaned via anealing to 600 K to remove the surface contamination in the molecular beam epitaxy chamber with a base pressure of 2×10^{-10} *mbar*. Bismuth atoms are deposited on the epitaxial graphene at room temperature with the Knudsen cell evaporator, meanwhile, the adatom doping concentration is determined by the deposition flux. After deposition, samples are in situ transferred to the ARPES chamber via a high vacuum to ensure a clean sample surface. With different contents of Bi dopants, the varied n-type doping graphene is achieved.

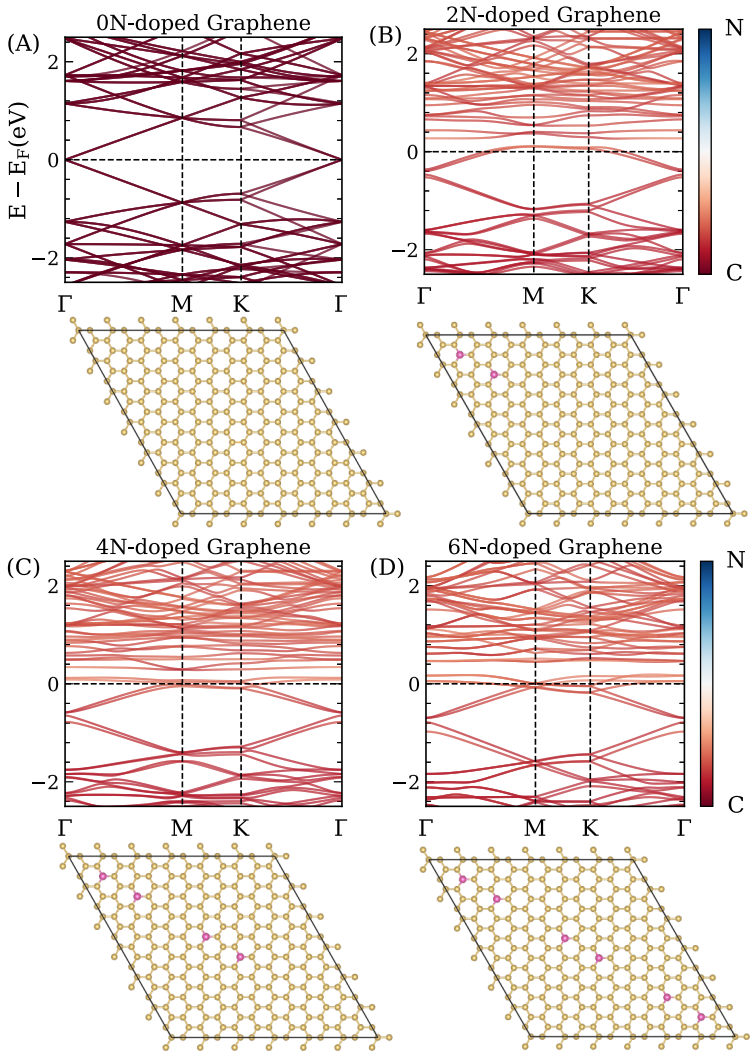

Figure 5.1: Electronic and crystal structures of graphene with different doping levels. Upper panel: Band structures of (A) undoped graphene, (B) 2N-doped graphene, (C) 4N-doped graphene and (D) 6N-doped graphene. Dashed lines represent the Fermi levels. Lower panel: Top view of crystal structures of corresponding doped graphene. Yellow and purple balls are carbon and nitrogen atoms.

5.3 Results and discussion

5.3.1 Theoretical simulations of doping dependence of carrier multiplication in graphene

To investigate the effect of doping levels on CM in graphene, two, four, and six carbon atoms are replaced by nitrogen atoms in $6\sqrt{3}\times6\sqrt{3}$ graphene supercell (lower panel of Figure 5.1). Obviously, nitrogen atoms introduce extra electrons to the system, lifting the Fermi level away from Dirac point by 0.40 eV, 0.58 eV and 0.78 eV respectively. To stimulate the excited carrier relaxation dynamics, a pair of electron-hole is created by moving electron from valence bands to conduction bands at 300 K, with excitation energy of 3.52 eV. In the case of pristine (undoped) graphene, the linear bandstructure leads to a symmetry excitation, in which the electron and hole excess energy (ΔE_e and ΔE_h) both equal to 1.76 eV. Here, the excess energy is defined as the energy difference between excited carriers and Fermi level. In the case of N-doped graphene, due to the change of Fermi level location, the electron excess energies are 1.36 eV, 1.18 eV and 0.98 eV in 2N-doped, 4N-doped and 6N-doped graphene, respectively.

In general, CM process in graphene is divide into two types. In the first case, CM occurs by scattering additional electron from valence bands to conduction bands, and this interband transition is labelled as *carrier multiplication*. On the other hand, counting carriers with respect to the Fermi level, and CM takes places via Coulomb-induced scattering electrons over the Fermi level, which is defined as *hot carrier multiplication*. It is reported that CM involves interband scattering at low Fermi energy ($E_F \leq 0.1$ eV), while intraband scattering contributes to the CM process at high Fermi energy ($E_F \geq 0.15$ eV)[178]. In other words, *hot carrier multiplication* dominates the CM process in strongly doped graphene. In the following part, CM is actually referred as *hot carrier multiplication*.

To demonstrate the effect of doping levels on CM, we simulate the CM QY in different N-doped graphene. As shown in Figure 5.2, strongly n-doped graphene indeed triggers more efficient CM. Specifically, the CM QY is increased from 1.41 to 1.89 when the Fermi level is lifted from 0.40 eV to 0.78 eV. However, for pristine graphene, there is no CM observed, which is conflicted with previously reported theoretical prediction[55]. To explore the origin of the absence of CM in pristine graphene and the mechanism of CM in doped graphene, we present the density of

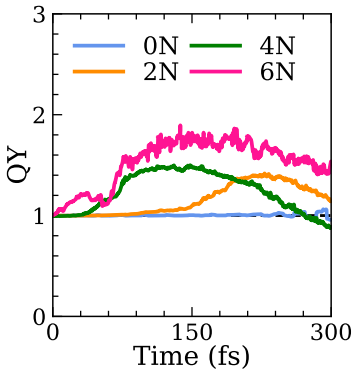

Figure 5.2: CM QY of graphene with different doping levels. The electron-hole pair is generated by phonon with energy of 3.52 eV at 300K.

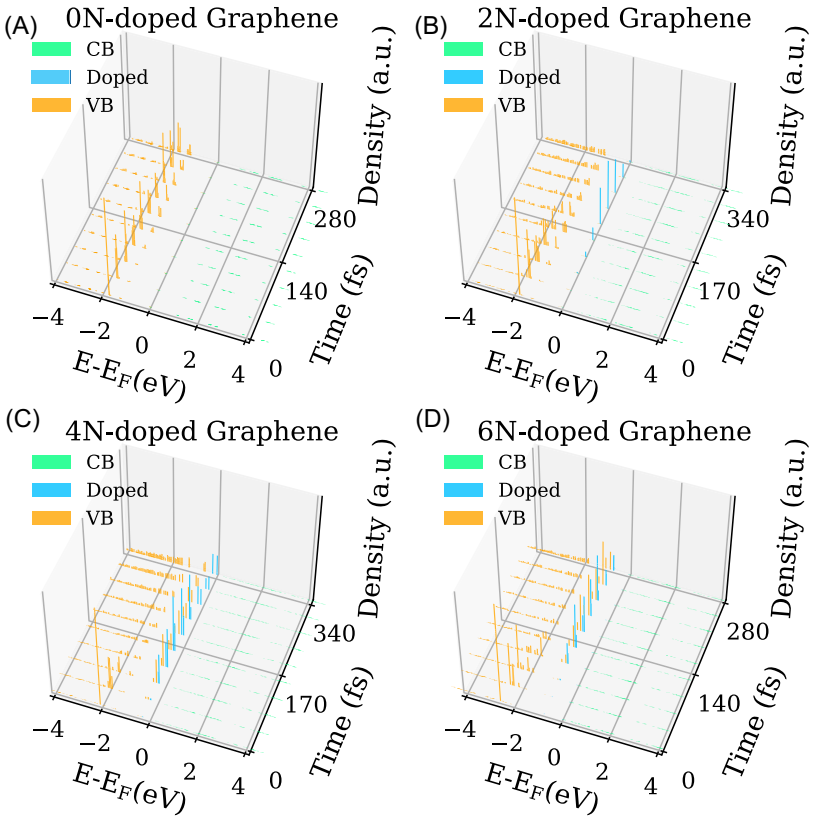

Figure 5.3: Density of excited hole as a function of time and energy. Conduction bands (CB), valence bands (VB), doped states (Doped) are in green, orange and blue, respectively.

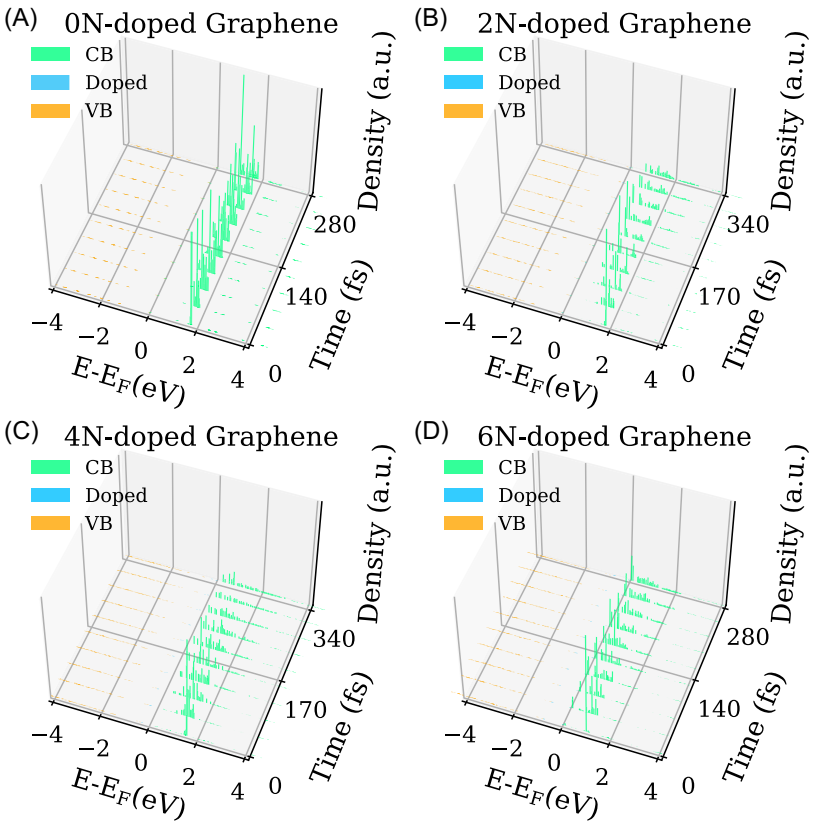

Figure 5.4: Density of excited electron as a function of time and energy. Conduction bands (CB), valence bands (VB), doped states (Doped) are in green, orange and blue, respectively.

excited electron and hole as a function of time and energy in undoped, 2N-doped, 4N-doped and 6N-doped graphene. As shown in Figure 5.3(A) and Figure 5.4(A), in undoped graphene, excited hole and electron both occupy higher energy regions, which indicate the occurrence of Auger recombination. Meanwhile, portion of excited hole and electron also distribute in lower energy region, which is related to CM process or phonon-assisted cooling relaxation. Thus, the absence of CM in pristine graphene should be attributed to the equality of CM rate and Auger recombination rate. Reported theoretical and experimental research both indicate that higher carrier concentration conditions favour the Auger recombination which competes with CM process[179, 180]. Winzer *et al.* reported that CM rate and Auger recombination rate reach an equilibrium very fast when the initial carrier density in the range of 10^{13}cm^{-2}, while the carrier concentration in our simulation is exactly $\sim 3\times10^{13}$cm^{-2}. Therefore, the absence of CM in pristine graphene comes from higher carrier concen-

tration induced more efficient Auger recombination. In contrast, n-doped graphene favours CM process. Obviously, a portion of excited hole occupies the doped states, especially, the more strongly n-doped graphene, the more excited hole on doped states. In strongly n-doped graphene, photoexcited electron can easily find scattering partner in the Fermi sea to involve in CM process owing to the larger scattering phase space. Thus, CM process prevails over the Auger recombination, dominating the carrier relaxation dynamics.

5.3.2 Experimental measurements of doping dependence of carrier multiplication in graphene

To further demonstrate the role of doping level in CM, we investigate the photoexcited carrier dynamics in n-doped graphene with different doping level using TR-ARPES, which is a powerful tool to identify the time-evolution of electrons in energy and momentum resolution. N-doped graphene with different doping levels are grown via adhering to different contents of bismuth dopants, and the doping level of graphene can be revealed by static ARPES at room temperature. As shown in Figure 5.5, the Fermi level in pristine graphene is located at ∼0.38 eV above the Dirac point due to the substrate[181, 182]. Accompanied with adsorption of higher amount of Bi atoms, as indicated by the red arrow in Figure 5.5, the Fermi level shifts toward the Dirac point, which is caused by the lower electron affinity of bismuth atoms. Specifically, with the bismuth coverage varying from 0.14 to 0.28 monolayer, the Fermi level moves from 0.38 eV to 0.35 eV to 0.30 eV above the Dirac point. In other words, with bismuth adatoms, we successfully obtain n-doped graphene with different doping levels, ranging from 0.30 eV to 0.38 eV.

TR-ARPES measurements are performed following a pump-probe scheme. To generate the pump and probe pulses, a 1 kHz Ti:sapphire amplified laser system provides ultrafast infrared pulses with a wavelength 800 nm (∼1.55 eV), and the pulse duration is 50 fs. The laser beam is split into two, the one beam is used as pump light to introduce excitation from valence bands to conduction bands, and the other one is collimated into the high-harmonic generation chamber in a pulsed jet of argon gas. The harmonic probe pulses with a photon energy of ∼26.35 eV is selected as the probe light. TR-ARPES data is acquired by spatial overlapping pump and probe beams. The pump fluence is set to 1.5 mJ/cm^2 during the measurements, and pump and probe beam are both s-polarized, which is oriented along Γ-K direction. The

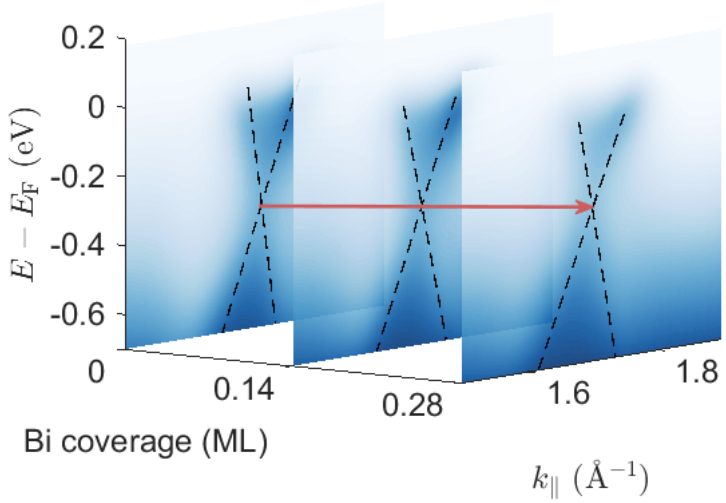

Figure 5.5: Band structure of expitaxial graphene with increasing bismuth coverage along Γ-K direction. The dashed black lines are the guide for eyes, and the red arrow represents the variation of Dirac point relative to Fermi level. The Fermi levels are set to zero.

sample temperature is fixed at room temperature, and the overall energy resolution and time resolution are 190 meV and 60 fs, respectively. As shown in Figure 5.6, instead of the Dirac cone, only one branch is visible due to the matrix element effect induced by the polarized probe pulse[183–185]. Obviously, after the pump pulse (t = 100 fs), an increase of spectral intensity above E_F is captured in all samples. Then, the excited electrons dissipate the excess energy via phonon scattering. Finally, after ∼3 ps, carrier distribution returns to equilibrium state by electron-hole recombination.

Since the thermalization of excited electrons has been realized within the pump pulse duration, the measured electron distribution can be treated as a quasi-equilibrium state at each delay time step (60 fs) and Fermi-Dirac (FD) distribution can be applied[58, 179, 186]. As shown in Figure 5.7(A), time-evolution of electronic temperature can be evaluated by FD fitting. Obviously, electronic temperature gives a rise to ∼2500 K instantly in all three samples. Then, the CM QY in doped graphene can be obtained by the following ratio[58, 186],

$$QY = \frac{n(T_e) - n(300K)}{n_0} \tag{5.1}$$

where $n(T_e)$ is the total hot carrier at highest electronic temperature which equals to ∼ 2500 K in three cases, and $n(300\ \mathrm{K})$ is total hot carrier at room temperature,

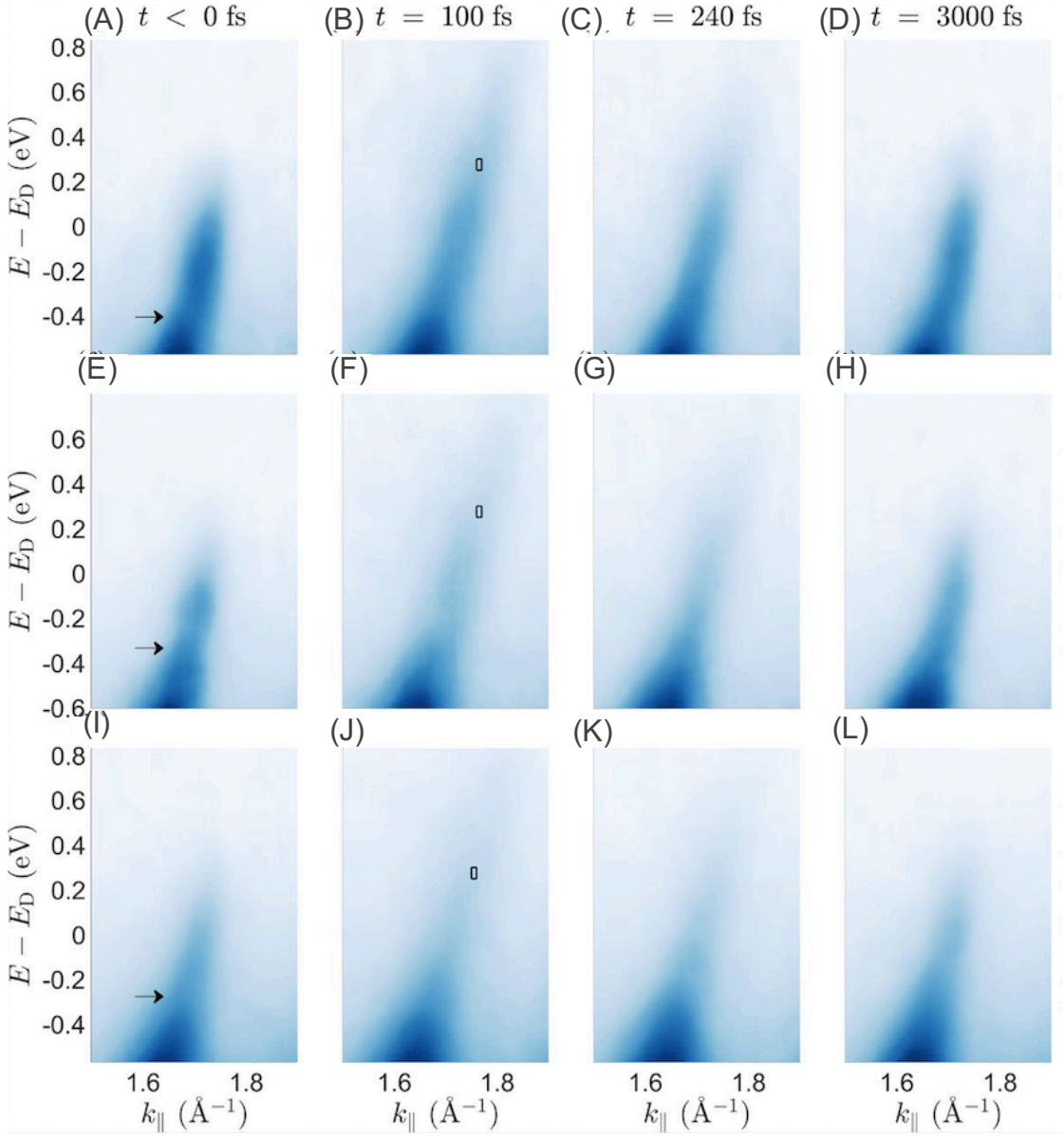

Figure 5.6: Photoexcitation dynamics in graphene with different doping levels. (A)-(D) Dispersion of pristine graphene around K-point taken before the pump pulse and 100 fs, 240 fs and 3000 fs after the pump pulse. (E)-(H) and (I)-(L) present the time-evolution of band structures for graphene/0.14 Bi and graphene/0.28 Bi.

and n_0 represents the amount of absorbed photons. As shown in Figure 5.7(B), the CM QY in pristine graphene is the highest, with a value of ∼2.80. While with bismuth coverage, the QY is decreased to ∼2.40 and ∼1.70 in graphene/0.14Bi and graphene/0.28Bi, respectively. In other words, the CM QY is increased from ∼1.70

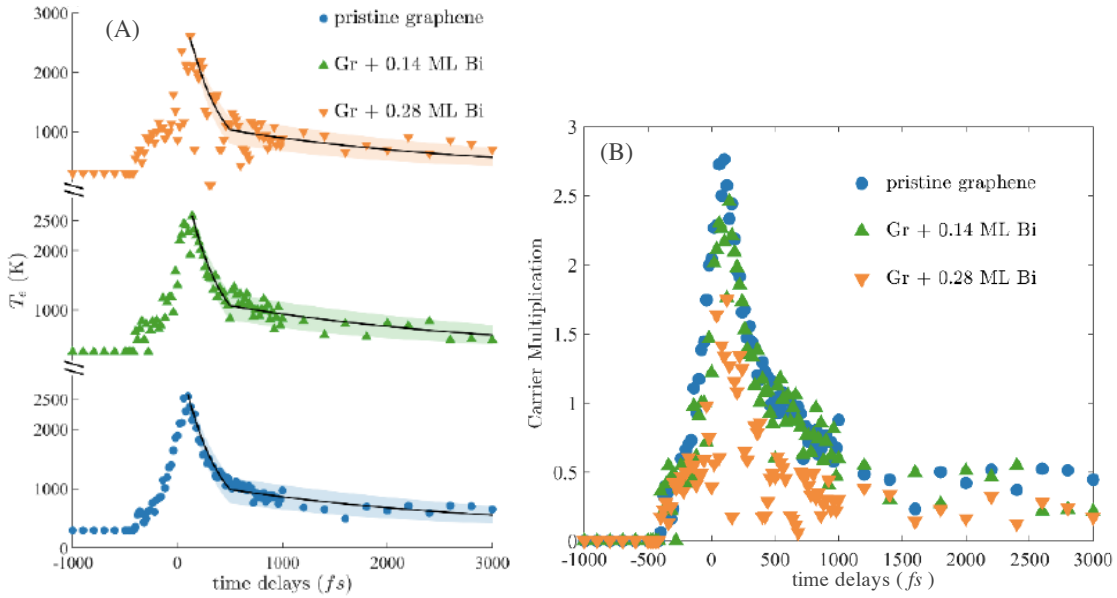

Figure 5.7: Excitation dynamics of pristine graphene, graphene/0.14Bi and graphene/0.28Bi. Time-evolution of (A) electronic temperature and (B) CM QY after pump and probe pulse in three samples.

to ∼2.80 when the Fermi level rising from 0.30 eV to 0.38 eV, which is consistent with our theoretical calculations. Therefore, tuning doping levels is an effective method to manipulate CM performance in graphene.

5.4 Conclusion

In summary, with rt-TDDFT-NAMD and TR-ARPES methods, we investigate CM phenomenon in n-doped graphene. It is found that CM characteristic is more efficient in strongly n-doped graphene. Since the larger phase space in strongly n-doped graphene provides more available scattering partners for excited electrons in the Fermi sea to involve in CM process. Thus, high carrier mobility and easily tunable CM characteristic promote graphene performance in photovoltaic devices.

Chapter 6

Summary and conclusion

The results of chapter 3 reveal the mechanism of interlayer charge transfer in graphene/TMDCs heterostructures. It is found that phonon modes of graphene and WS_2 are related to the interlayer couplings and then facilitate the interlayer charge transfer. Specially, G-mode of graphene is related to interlayer hole and electron transfer, while A_{1g}-mode is only associated with interlayer electron transfer. Moreover, our results provide a practical method to manipulate the interlayer couplings, and then control the carrier dynamics via external electric fields.

The results of chapter 4 give a insight on the mechanism of CM in monolayer TMDCs. It is found that out-of-plane A'-mode induced reduction of bandgap lowers CM threshold energy beyond limit. Meanwhile, chalcogen vacancies can further lower the CM threshold to 1.51 E_g. Based on these findings, we present an effective strategy to trigger CM with below threshold limit excitation energy in monolayer TMDCs, promoting their performance in photovoltaic devices.

The results in chapter 5 identify the mechanism of CM in n-doped graphene. In strongly n-doped graphene, CM characteristic is more efficient. Since the larger phase space provides more scattering partners for excited electrons in the Fermi sea to trigger CM process. Doping level tunable CM characteristic enables graphene as a prospective photovoltaic materials in next-generation optoelectronic applications.

In summary, it is hoped that the results of this thesis will contribute to better understanding of carrier dynamics in layered 2D materials and provide instrumental advice for their future applications.

Appendix A

Electronic structures of graphene/WS_2 heterostructure

A.1 Density of States

Figure A.1 shows the density of states (DOS) of graphene/WS_2 heterostructure applied with different external electric fields, varying from -0.3 V/Å to +0.3 V/Å. The density of acceptor states for photoexcited electron and hole are similar when no electric field is applied. Thus, it is expected the availability of acceptor states for electron and hole transfer should be similar. The more efficient interlayer hole transfer is attributed to the couplings between states on the two layer. In the case of applied fields, it can be seen that negative electric field significantly increases the density of acceptor states for hole transfer, which is 10 times more than that for electron transfer. Meanwhile, positive electric field has the same effect on the density of acceptor states for electron.

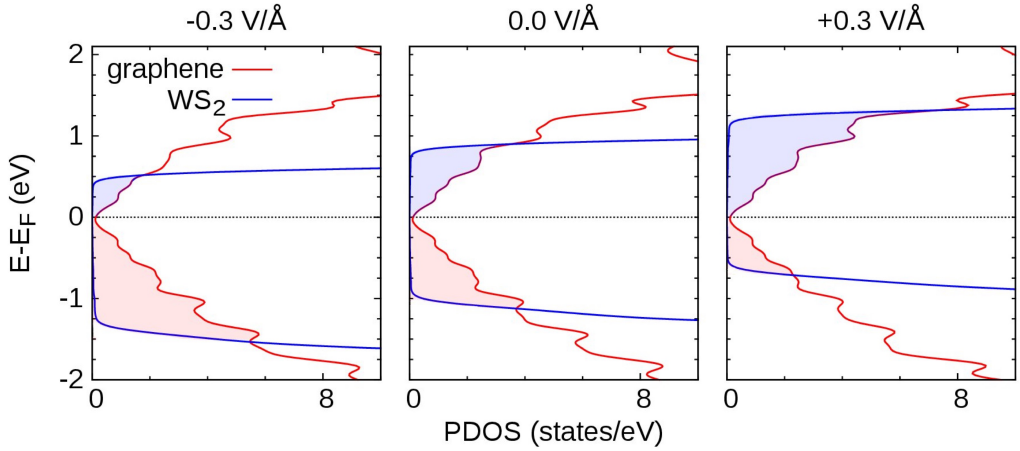

Figure A.1: The DOS of graphene/WS_2 heterostructure with external electric fields, varying from -0.3 V/Å to +0.3 V/Å. The density of acceptor states on graphene for photoexcited electron and hole are illustrated by blue and red areas, respectively.

A.2 Electronics structure of graphene/WS_2 heterostructure applied with ± 0.1 V/Å electric fields

Applied with -0.1V/Å and +0.1V/Å electric fields, electronic structures of graphene/WS_2 heterostructure exhibit the similar response as that applied with

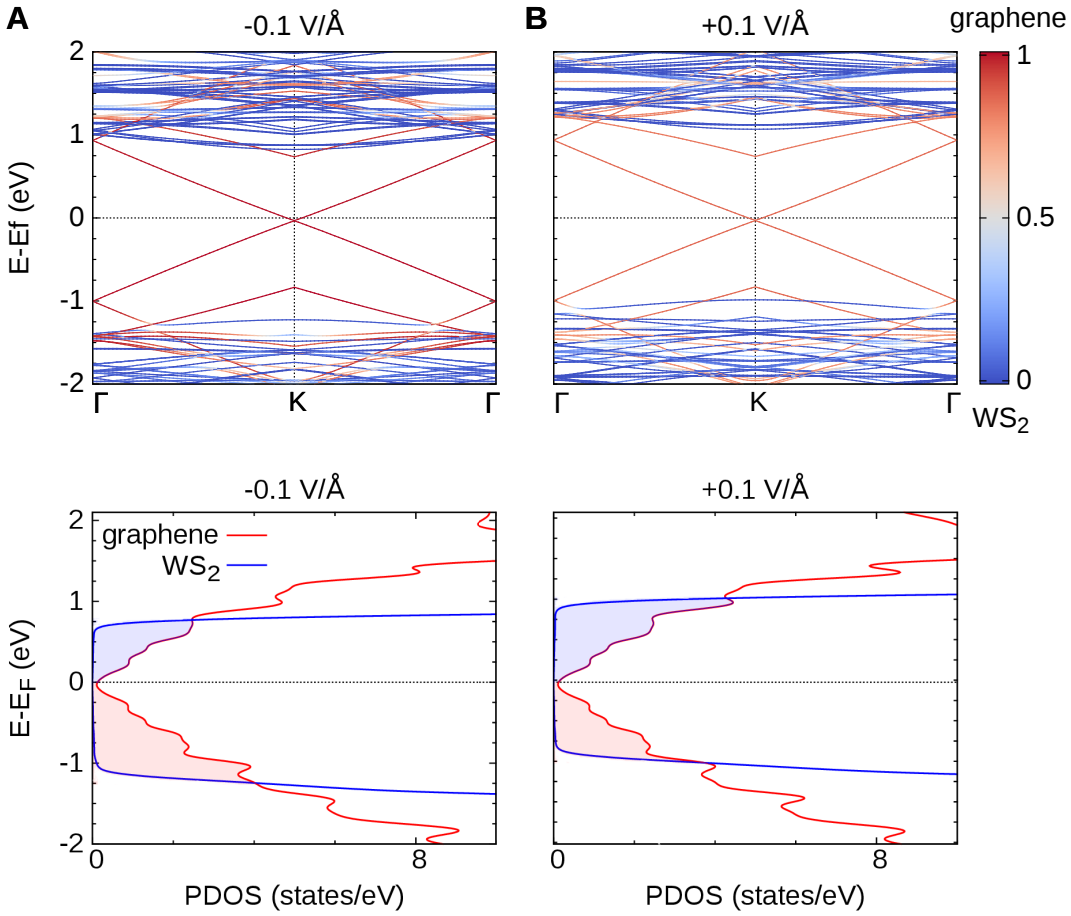

Figure A.2: Band structures and DOS of graphene/WS_2 heterostructure with different applied electric fields, varying from (A) -0.1 V/Å to (B) +0.1 V/Å. Fermi energy is set to zero. Same color map as Figure 1D is employed to show the charge localization. The density of acceptor states on graphene for photoexcited electron and hole are illustrated by blue and red areas, respectively.

-0.3V/Å and +0.3V/Å electric fields. As shown in Figure A.2(A), -0.1V/Å electric field downshifts the WS_2 states, which increases acceptor states for hole transfer and simultaneously suppresses electron transfer due to the decrease of available states. On the contrary, +0.1V/Å electric field upshifts the WS_2 states, and thus accelerates electron transfer but impedes hole transfer. The time-evolution of $n_{e/h}(t)$, $\epsilon_{e/h}(t)$ and $\tau_{e/h,L}(t)$ are presented in Figure 3.10 to further demonstrate the above findings. For the case of +0.1V/Å electric field, it is found that some of the states are delocalized over both graphene and WS_2 layers. Taking into account the delocalization effect, Eq. 3.3 is modified by including a weight factor $f_j^{L_n}$: $\tau_{i,L_n}(t) = \sum_{j\neq i, j\epsilon L_n} f_j^{L_n} |\sigma_{ij}(t)|$.

$f_j^{L_n}$ corresponds to the fraction of the state j that are localized on layer L_n.

Appendix B

Electronic structures of monolayer TMDCs

B.1 Electronic structures of monolayer TMDCs

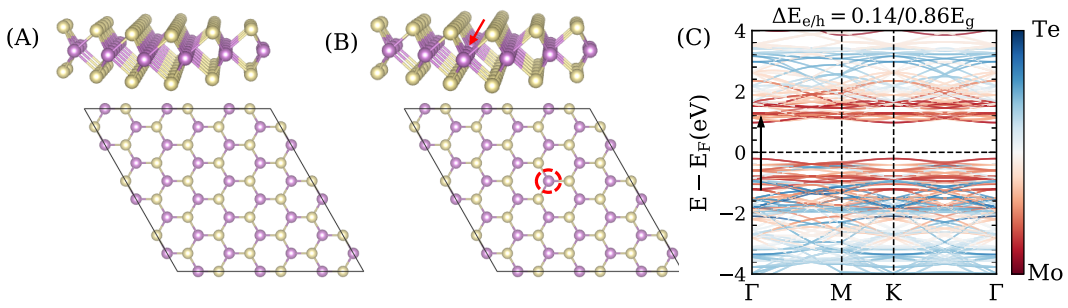

Figure B.1: Side view and top view of the $3\sqrt{3} \times 3\sqrt{3}$ supercell of (A) pristine monolayer MX_2, (B) monolayer MX_2 with chalcogen vacancy defect. The yellow and purple spheres represent chalcogen and transition metal atoms, respectively. Chalcogen vacancy defect is highlighted with red arrow and red cycles at side and top views. (C) Electron-hole pairs excited with photon energy of $2E_g$. The hole and the electron excess energy are $0.86E_g$ and $0.14E_g$, respectively.

To investigate CM phenomena in monolayer TMDCs, we build a $3\sqrt{3} \times 3\sqrt{3}$ supercell with 81 atoms shown in Figure B.1(A). vdW layered TMDCs, represented by MX_2 (M = Mo, W; X = Te, Se, S), exhibit indirect-to-direct bandgap transition when exfoliated from bulk to monolayer. As shown in Figure B.2, the six different monolayer TMDCs are all direct semiconductors, and the bandgap increases as the anions change from sulfur to tellurium and cations change from molybdenum to tungsten owing to the decrease in electronegativity and increase of ionic radii.

B.2 Lattice vibrational modes in monolayer TMDCs

To verify the relationship between nuclear motions and electronic structures, we simulate lattice vibrational modes in monolayer TMDCs. The phonon dispersion and ionic vibrations of four optical phonon modes are shown in Figure 4.5 and Figure B.3-Figure B.7. These calculated vibration frequencies coincide with experimental measurements[187–191]. Similar to monolayer $MoTe_2$, all four optical phonons, including A", E', A' and E" modes, significantly change the electronic structures in the other five monolayer TMDCs, leading to a narrower of bandgap.

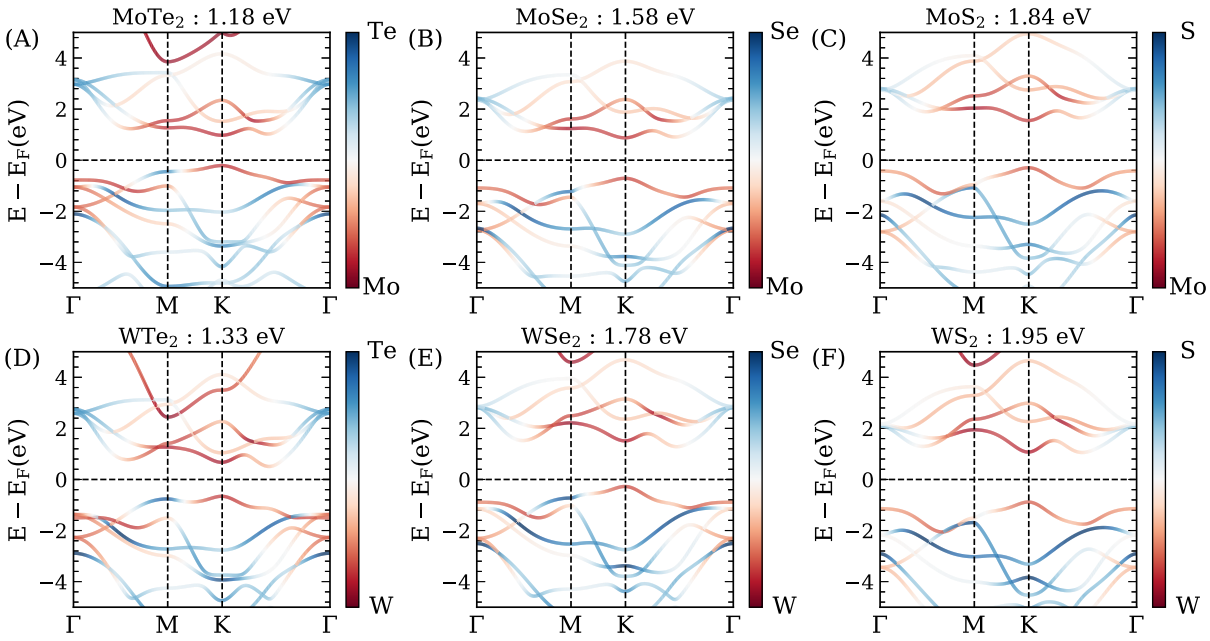

Figure B.2: Band structure of monolayer (A) $MoTe_2$, (B) $MoSe_2$, (C) MoS_2, (D) WTe_2, (E) WSe_2 and (F) WS_2. The dashed lines show the Fermi level E_F.

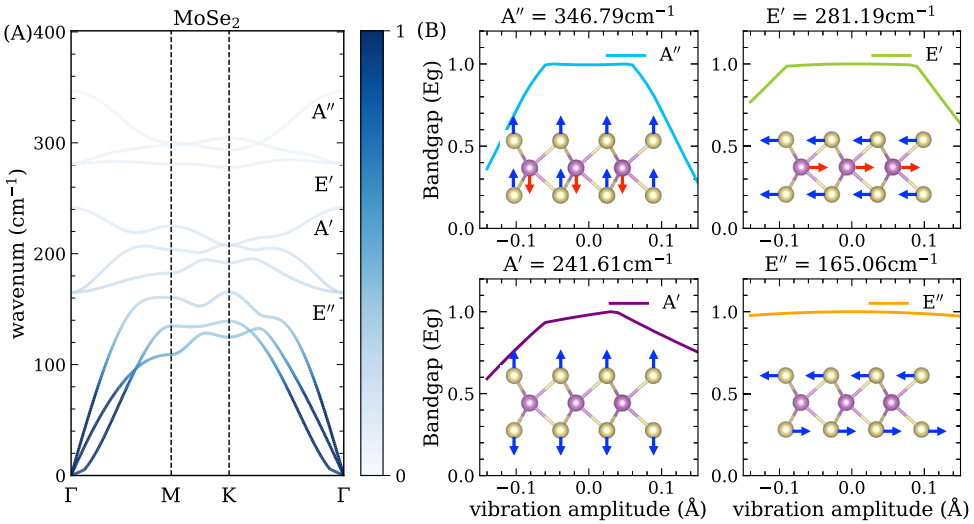

Figure B.3: Lattice vibrational modes in monolayer $MoSe_2$. (A) Phonon dispersion of monolayer $MoSe_2$. The colormap indicates the phonon occupation number which is determined by the Bose-Einstein distribution at 300K. (B) The bandgap as a function of vibration amplitude of four optical phonon in $MoSe_2$. The insets show the corresponding lattice vibrations for optical phonons at Γ point.

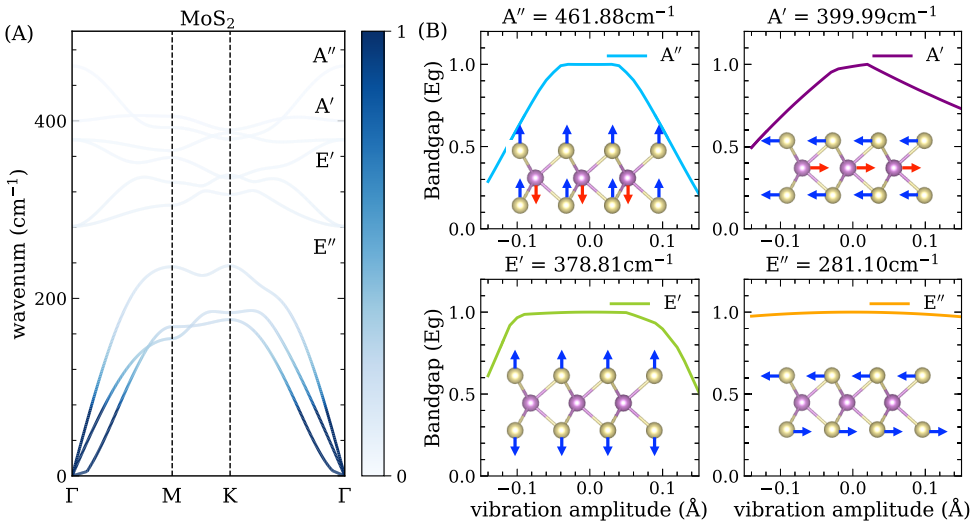

Figure B.4: Lattice vibrational modes in monolayer MoS_2. (A) Phonon dispersion of monolayer MoS_2. The colormap indicates the phonon occupation number which is determined by the Bose-Einstein distribution at 300K. (B) The bandgap as a function of vibration amplitude of four optical phonon in MoS_2. The insets show the corresponding lattice vibrations for optical phonons at Γ point.

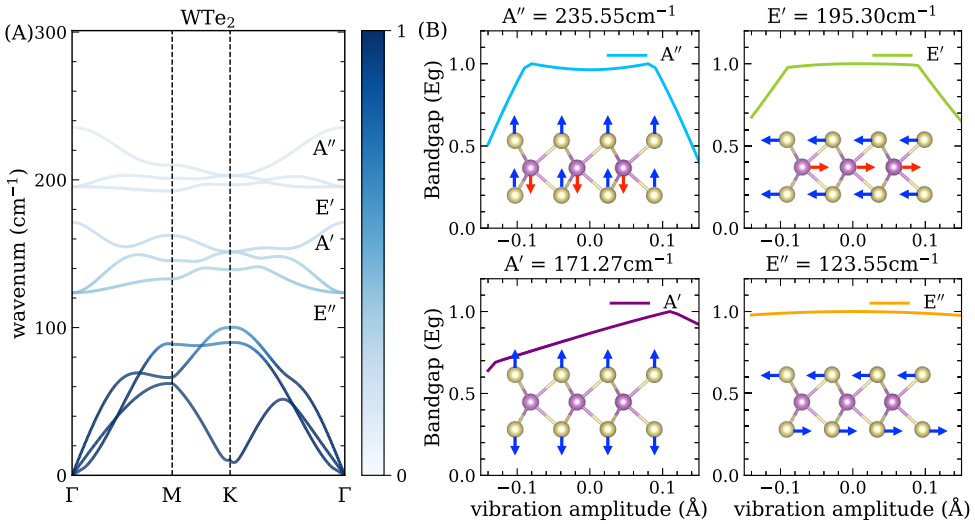

Figure B.5: Lattice vibrational modes in monolayer WTe_2. (A) Phonon dispersion of monolayer WTe_2. The colormap indicates the phonon occupation number which is determined by the Bose-Einstein distribution at 300K. (B) The bandgap as a function of vibration amplitude of four optical phonon in WTe_2. The insets show the corresponding lattice vibrations for optical phonons at Γ point.

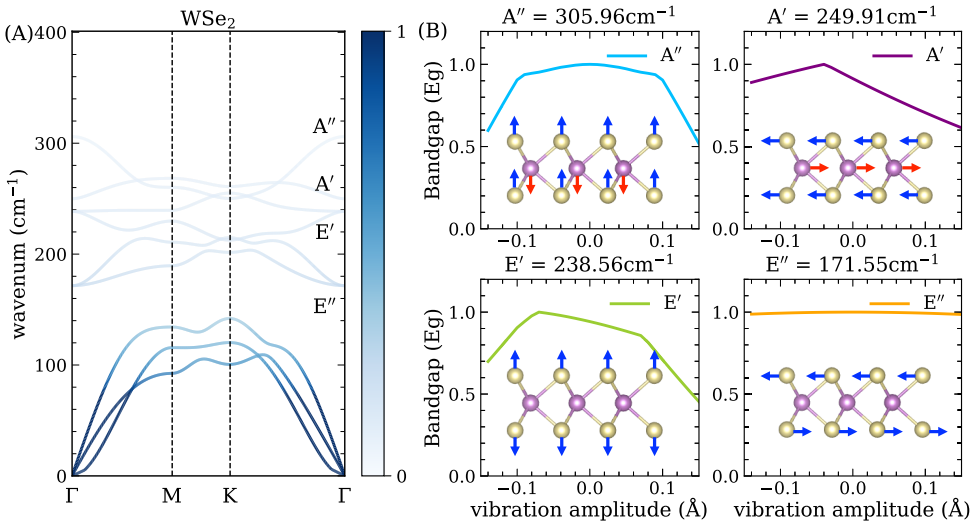

Figure B.6: Lattice vibrational modes in monolayer WSe_2. (A) Phonon dispersion of monolayer WSe_2. The colormap indicates the phonon occupation number which is determined by the Bose-Einstein distribution at 300K. (B) The bandgap as a function of vibration amplitude of four optical phonon in WSe_2. The insets show the corresponding lattice vibrations for optical phonons at Γ point.

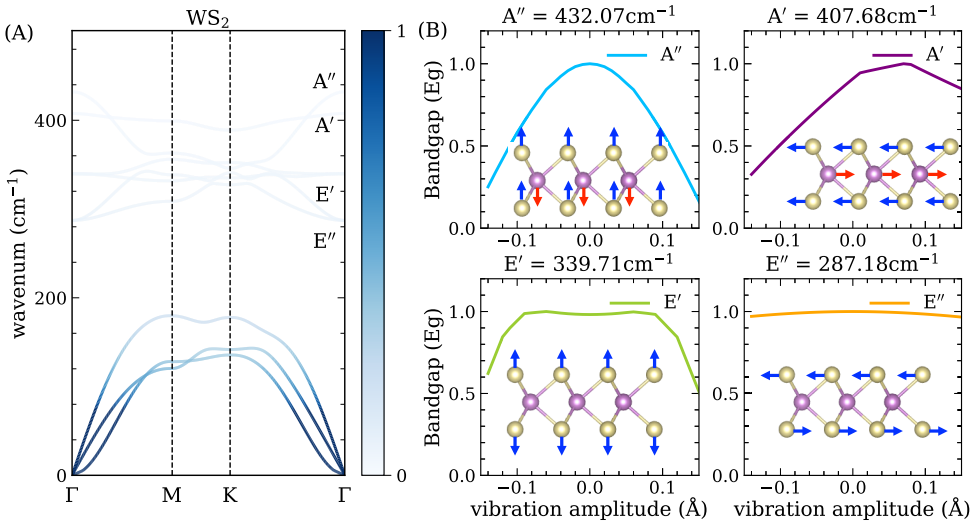

Figure B.7: Lattice vibrational modes in monolayer WS_2. (A) Phonon dispersion of monolayer WS_2. The colormap indicates the phonon occupation number which is determined by the Bose-Einstein distribution at 300K. (B) The bandgap as a function of vibration amplitude of four optical phonon in WS_2. The insets show the corresponding lattice vibrations for optical phonons at Γ point.

Appendix C

Excitation dynamics in monolayer TMDCs

C.1 Excitation Dynamics in monolayer $MoTe_2$

For further analysis the role of EPC in CM process, carriers are excited in monolayer $MoTe_2$ with energy of $2E_g$ at 77 K, 300 K and 500 K, respectively. Excitations with two different excess energy distribution are simulated ($\Delta E_{e/h}$=0.14/0.86E_g and $\Delta E_{e/h}$=0.50/0.50E_g). As discussed in chapter4, for asymmetric electron-hole pair, CM phenomenon is observed at all three temperatures. It is found that increasing temperature has a positive effect on improving carrier generation QY. Compared with 77 K, the CM conversion efficiency η_{CM} is about doubled at 500 K. With a higher temperature, ionic vibrations are more intense, which results in a narrower bandgap and consequently more efficient carrier generation QY. As shown in Figure C.1 and Figure 4.1, from 77 K to 500 K, the reduction of bandgap increasing from 28% to 64%. If keep increasing temperature, semicondutor-to-metal transitions may eventually kick in. In the case of carriers with excess energies of $\Delta E_{e/h}$=0.5/0.5E_g, CM phenomenon is only observed in 500 K among three cases. Consistently, Figure C.2(A) shows that the electron excess energy ΔE_e(t) is beyond E_g(t) at about 100 fs. In contrast, E_g(t) is always larger than $\Delta E_{e/h}$(t) after excitation in the case of 77 K and 300 K (Figure C.2(B) and Figure 4.1(F)). Therefore, it is possible to break the threshold limit for CM via coupling to phonons.

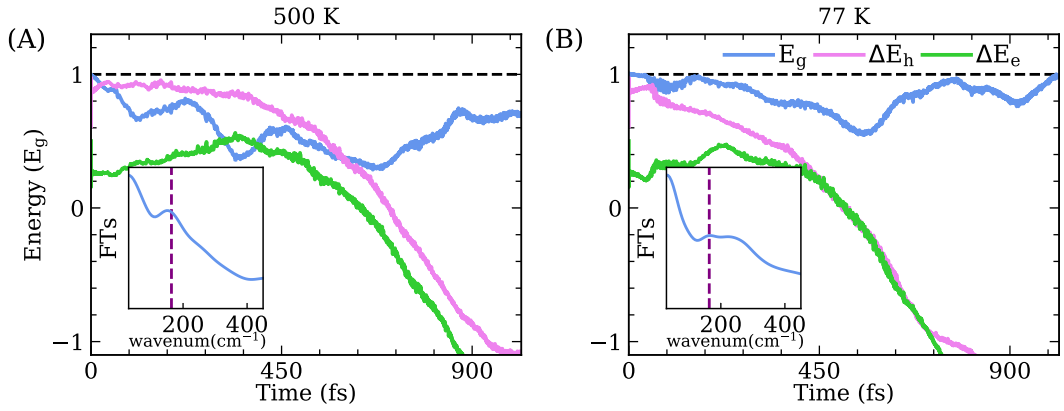

Figure C.1: Excitation dynamics in monolayer $MoTe_2$ with carrier excess energy of $\Delta E_{e/h} = 0.14/0.86Eg$. Electron-hole pairs are excited at different temperatures. Comparison of E_g(t), ΔE_e(t) and ΔE_h(t) at excitation temperature of (A) 500K and (B) 77 K. Inset: FTs of time-dependent bandgap $E_g(t)$. Vertical dashed lines represent phonon mode A' with vibrational frequency of 163.7 cm^{-1}.

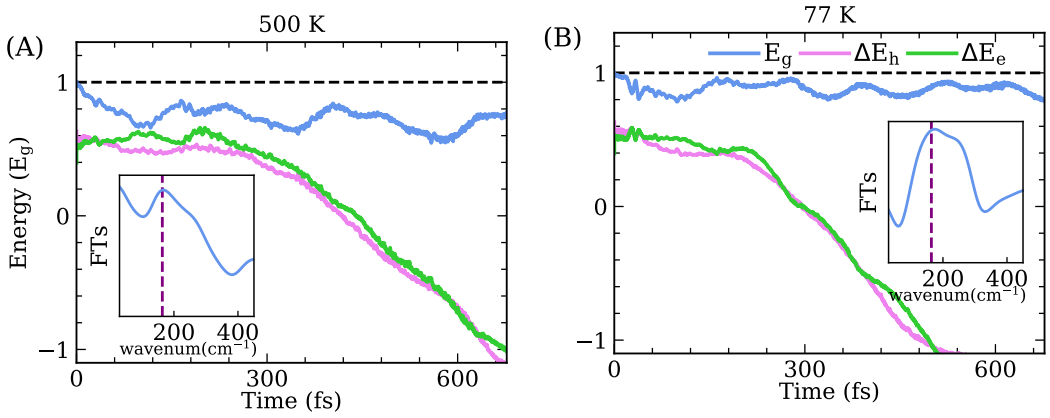

Figure C.2: Excitation dynamics in monolayer $MoTe_2$ with carrier excess energy of $\Delta E_{e/h} = 0.50/0.50Eg$. Electron-hole pairs are excited at different temperatures. Comparison of E_g(t), ΔE_e(t) and ΔE_h(t) at excitation temperature of (A) 500K and (B) 77 K. Inset: FTs of time-dependent bandgap $E_g(t)$. Vertical dashed lines represent phonon mode A' with vibrational frequency of 163.7 cm^{-1}.

C.2 Effect of chalcogen vacancy defect on carrier dynamics

To optimize the electronic structures of TMDCs to enhance their performance for photovoltaic applications, a sulfur vacancy is introduced to the $3\sqrt{3} \times 3\sqrt{3}$ supercell of monolayer WS_2 (Figure B.1(B)), corresponding to a defect concentration of $3.66 \times 10^{13} cm^{-2}$. As shown in Figure C.3, the calculated bandgap of pristine monolayer WS_2 is 1.95 eV, which is consistent with previously reported values[192]. The sulfur vacancies create two defect states, one is shallow hole trap state which reduces bandgap by a value of 0.03 eV, and the other is deep electron trap state that is 0.48 eV below the CBM. Thus, sulfur vacancies lower the bandgap of monolayer WS_2 by a vaule of ∼0.51 eV.

Carriers are excited in pristine monolayer WS_2 and monolayer WS_2 with sulfur vacancy by photons with energy of 1.51 E_g. The carrier excess energy is the same in two cases, with a value of $\Delta E_{e/h}$=0.36/0.15E_g. Compared with pristine monolayer WS_2, with phonon-assisted modulation and defect states, CM phenomenon is observed in monolayer WS_2 with sulfur vacancy, and CM conversion efficiency is ∼2.37%. As shown in Figure 4.8(B)-(C) and Figure C.4, the deep electron defect states play an important role in the relaxation dynamics, in which excited holes with

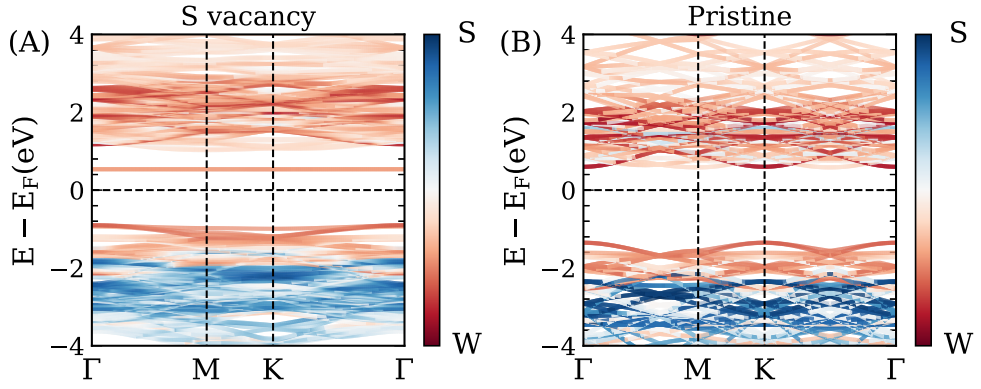

Figure C.3: Band structures of $3\sqrt{3} \times 3\sqrt{3}$ supercell of (A) monolayer WS_2 with S vacancy, and (B) pristine monolayer WS_2. The dashed lines indicate the Fermi levels.

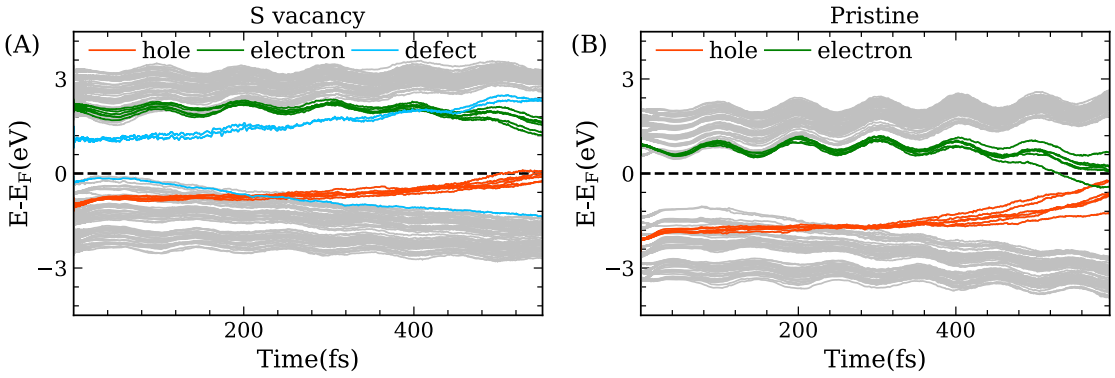

Figure C.4: Time-evolution of energy states after excitation in (A) monolayer WS_2 with sulfur vacancy, and (B) pristine mononlayer WS_2. The blue, red and green lines are defect states, excited hole and electron states, respectively. The dashed lines indicate the Fermi levels.

sufficient energy scatter additional electrons from occupied valence bands to these deep trap states. Eventually, CM process prevails over Auger decay and nonradiative recombination.

Bibliography

1. Novoselov, K. S. *et al.* Electric field effect in atomically thin carbon films. *Science* **306,** 666–669 (2004).
2. Duan, X., Wang, C., Pan, A., Yu, R. & Duan, X. Two-dimensional transition metal dichalcogenides as atomically thin semiconductors: opportunities and challenges. *Chemical Society Reviews* **44,** 8859–8876 (2015).
3. Schmidt, H., Giustiniano, F. & Eda, G. Electronic transport properties of transition metal dichalcogenide field-effect devices: surface and interface effects. *Chemical Society Reviews* **44,** 7715–7736 (2015).
4. Avouris, P. & Xia, F. Graphene applications in electronics and photonics. *Mrs Bulletin* **37,** 1225–1234 (2012).
5. Wang, Q. H., Kalantar-Zadeh, K., Kis, A., Coleman, J. N. & Strano, M. S. Electronics and optoelectronics of two-dimensional transition metal dichalcogenides. *Nature Nanotechnology* **7,** 699–712 (2012).
6. Liu, L. *et al.* Heteroepitaxial growth of two-dimensional hexagonal boron nitride templated by graphene edges. *Science* **343,** 163–167 (2014).
7. Takao, Y., Asahina, H. & Morita, A. Electronic structure of black phosphorus in tight binding approach. *Journal of the Physical Society of Japan* **50,** 3362–3369 (1981).
8. Naguib, M. *et al.* New two-dimensional niobium and vanadium carbides as promising materials for Li-ion batteries. *Journal of the American Chemical Society* **135,** 15966–15969 (2013).
9. Naguib, M. *et al.* Two-dimensional transition metal carbides. *ACS Nano* **6,** 1322–1331 (2012).

10. Khan, K. *et al.* Recent advances in two-dimensional materials and their nanocomposites in sustainable energy conversion applications. *Nanoscale* **11,** 21622–21678 (2019).

11. Chia, X. & Pumera, M. Characteristics and performance of two-dimensional materials for electrocatalysis. *Nature Catalysis* **1,** 909–921 (2018).

12. Kostarelos, K. Translating graphene and 2D materials into medicine. *Nature Reviews Materials* **1,** 1–2 (2016).

13. Gosling, J. H. *et al.* Universal mobility characteristics of graphene originating from charge scattering by ionised impurities. *Communications Physics* **4,** 1–8 (2021).

14. Stoller, M. D., Park, S., Zhu, Y., An, J. & Ruoff, R. S. Graphene-based ultracapacitors. *Nano Letters* **8,** 3498–3502 (2008).

15. Bolotin, K. I. *et al.* Ultrahigh electron mobility in suspended graphene. *Solid State Communications* **146,** 351–355 (2008).

16. Du, X., Skachko, I., Barker, A. & Andrei, E. Y. Approaching ballistic transport in suspended graphene. *Nature Nanotechnology* **3,** 491–495 (2008).

17. Schwierz, F. Graphene transistors. *Nature Nanotechnology* **5,** 487–496 (2010).

18. Lin, Y.-M. *et al.* 100-GHz transistors from wafer-scale epitaxial graphene. *Science* **327,** 662–662 (2010).

19. Zheng, J. *et al.* Sub-10 nm gate length graphene transistors: operating at terahertz frequencies with current saturation. *Scientific Reports* **3,** 1–9 (2013).

20. Brownson, D. A., Kampouris, D. K. & Banks, C. E. Graphene electrochemistry: fundamental concepts through to prominent applications. *Chemical Society Reviews* **41,** 6944–6976 (2012).

21. Kim, K. S. *et al.* Large-scale pattern growth of graphene films for stretchable transparent electrodes. *Nature* **457,** 706–710 (2009).

22. Balandin, A. A. *et al.* Superior thermal conductivity of single-layer graphene. *Nano Letters* **8,** 902–907 (2008).

23. Bao, W., Cai, X., Kim, D., Sridhara, K. & Fuhrer, M. S. High mobility ambipolar MoS_2 field-effect transistors: Substrate and dielectric effects. *Applied Physics Letters* **102,** 042104 (2013).

24. Kang, D.-H. *et al.* High-performance transition metal dichalcogenide photodetectors enhanced by self-assembled monolayer doping. *Advanced Functional Materials* **25,** 4219–4227 (2015).

25. Tsai, M.-L. *et al.* Monolayer MoS_2 heterojunction solar cells. *ACS Nano* **8,** 8317–8322 (2014).

26. Ross, J. S. *et al.* Electrically tunable excitonic light-emitting diodes based on monolayer WSe_2 p-n junctions. *Nature Nanotechnology* **9,** 268–272 (2014).

27. Wang, T. *et al.* High-performance WSe_2 phototransistors with 2D/2D ohmic contacts. *Nano Letters* **18,** 2766–2771 (2018).

28. Fuhrer, M. S. & Hone, J. Measurement of mobility in dual-gated MoS_2 transistors. *Nature Nanotechnology* **8,** 146–147 (2013).

29. Geim, A. K. & Grigorieva, I. V. Van der Waals heterostructures. *Nature* **499,** 419–425 (2013).

30. Novoselov, K., Mishchenko, o. A., Carvalho, o. A. & Castro Neto, A. 2D materials and van der Waals heterostructures. *Science* **353,** aac9439 (2016).

31. Deng, D. *et al.* Catalysis with two-dimensional materials and their heterostructures. *Nature Nanotechnology* **11,** 218–230 (2016).

32. Liu, C. *et al.* A semi-floating gate memory based on van der Waals heterostructures for quasi-non-volatile applications. *Nature Nanotechnology* **13,** 404–410 (2018).

33. Georgiou, T. *et al.* Vertical field-effect transistor based on graphene-WS_2 heterostructures for flexible and transparent electronics. *Nature Nanotechnology* **8,** 100–103 (2013).

34. Liu, X. *et al.* Modulation of quantum tunneling via a vertical two-dimensional black phosphorus and molybdenum disulfide p-n junction. *ACS Nano* **11,** 9143–9150 (2017).

35. Vaziri, S. *et al.* A graphene-based hot electron transistor. *Nano Letters* **13,** 1435–1439 (2013).

36. Li, X. *et al.* Graphene and related two-dimensional materials: Structure-property relationships for electronics and optoelectronics. *Applied Physics Reviews* **4,** 021306 (2017).

37. Zhang, K. *et al.* Interlayer transition and infrared photodetection in atomically thin type-II $MoTe_2/MoS_2$ van der Waals heterostructures. *ACS Nano* **10,** 3852–3858 (2016).

38. Yin, J. *et al.* Ultrafast and highly sensitive infrared photodetectors based on two-dimensional oxyselenide crystals. *Nature Communications* **9,** 1–7 (2018).

39. Gibertini, M., Koperski, M., Morpurgo, A. F. & Novoselov, K. S. Magnetic 2D materials and heterostructures. *Nature Nanotechnology* **14,** 408–419 (2019).

40. Gong, C. & Zhang, X. Two-dimensional magnetic crystals and emergent heterostructure devices. *Science* **363,** eaav4450 (2019).

41. Jiang, S., Li, L., Wang, Z., Mak, K. F. & Shan, J. Controlling magnetism in 2D CrI_3 by electrostatic doping. *Nature Nanotechnology* **13,** 549–553 (2018).

42. Jiang, S., Shan, J. & Mak, K. F. Electric-field switching of two-dimensional van der Waals magnets. *Nature Materials* **17,** 406–410 (2018).

43. Jin, C. *et al.* Ultrafast dynamics in van der Waals heterostructures. *Nature Nanotechnology* **13,** 994–1003 (2018).

44. Bellus, M. Z. *et al.* Type-I van der Waals heterostructure formed by MoS_2 and ReS_2 monolayers. *Nanoscale Horizons* **2,** 31–36 (2017).

45. Hong, X. *et al.* Ultrafast charge transfer in atomically thin MoS_2/WS_2 heterostructures. *Nature Nanotechnology* **9,** 682–686 (2014).

46. Chen, H. *et al.* Ultrafast formation of interlayer hot excitons in atomically thin MoS_2/WS_2 heterostructures. *Nature Communications* **7,** 1–8 (2016).

47. Fu, S. *et al.* Long-lived charge separation following pump-wavelength–dependent ultrafast charge transfer in graphene/WS_2 heterostructures. *Science Advances* **7,** eabd9061 (2021).

48. Rigosi, A. F., Hill, H. M., Li, Y., Chernikov, A. & Heinz, T. F. Probing interlayer interactions in transition metal dichalcogenide heterostructures by optical spectroscopy: MoS_2/WS_2 and $MoSe_2/WSe_2$. *Nano Letters* **15,** 5033–5038 (2015).

49. Ji, Z. *et al.* Robust stacking-independent ultrafast charge transfer in MoS_2/WS_2 bilayers. *ACS Nano* **11,** 12020–12026 (2017).

50. Li, Y. *et al.* Electric field tunable interlayer relaxation process and interlayer coupling in WSe_2/graphene heterostructures. *Advanced Functional Materials* **26,** 4319–4328 (2016).

51. Beard, M. C., Luther, J. M., Semonin, O. E. & Nozik, A. J. Third generation photovoltaics based on multiple exciton generation in quantum confined semiconductors. *Accounts of Chemical Research* **46,** 1252–1260 (2013).

52. McGuire, J. A., Joo, J., Pietryga, J. M., Schaller, R. D. & Klimov, V. I. New aspects of carrier multiplication in semiconductor nanocrystals. *Accounts of Chemical Research* **41,** 1810–1819 (2008).

53. Pandey, A. & Guyot-Sionnest, P. Slow electron cooling in colloidal quantum dots. *Science* **322,** 929–932 (2008).

54. Schaller, R. D. & Klimov, V. I. High Efficiency Carrier Multiplication in PbSe Nanocrystals: Implications for Solar Energy Conversion. *Physical Review Letters* **92,** 186601 (18 2004).

55. Winzer, T., Knorr, A. & Malic, E. Carrier multiplication in graphene. *Nano Letters* **10,** 4839–4843 (2010).

56. Rana, F. Electron-hole generation and recombination rates for Coulomb scattering in graphene. *Physical Review B* **76,** 155431 (2007).

57. Song, J. C., Reizer, M. Y. & Levitov, L. S. Disorder-assisted electron-phonon scattering and cooling pathways in graphene. *Physical Review Letters* **109,** 106602 (2012).

58. Johannsen, J. C. *et al.* Direct view of hot carrier dynamics in graphene. *Physical Review Letters* **111,** 027403 (2013).

59. Kotov, V. N., Uchoa, B., Pereira, V. M., Guinea, F. & Neto, A. C. Electron-electron interactions in graphene: Current status and perspectives. *Reviews of Modern Physics* **84,** 1067 (2012).

60. Song, J. C., Rudner, M. S., Marcus, C. M. & Levitov, L. S. Hot carrier transport and photocurrent response in graphene. *Nano Letters* **11,** 4688–4692 (2011).

61. Song, J. C., Tielrooij, K. J., Koppens, F. H. & Levitov, L. S. Photoexcited carrier dynamics and impact-excitation cascade in graphene. *Physical Review B* **87,** 155429 (2013).

62. Kim, J.-H. *et al.* Carrier multiplication in van der Waals layered transition metal dichalcogenides. *Nature Communications* **10,** 1–9 (2019).

63. Zheng, W., Bonn, M. & Wang, H. I. Photoconductivity Multiplication in Semiconducting Few-Layer $MoTe_2$. *Nano Letters* **20,** 5807–5813 (2020).

64. Trinh, M. T. *et al.* Direct generation of multiple excitons in adjacent silicon nanocrystals revealed by induced absorption. *Nature Photonics* **6,** 316–321 (2012).

65. Cirloganu, C. M. *et al.* Enhanced carrier multiplication in engineered quasi-type-II quantum dots. *Nature Communications* **5,** 1–8 (2014).

66. Padilha, L. A. *et al.* Aspect ratio dependence of auger recombination and carrier multiplication in PbSe nanorods. *Nano Letters* **13,** 1092–1099 (2013).

67. Hohenberg, P. & Kohn, W. Inhomogeneous Electron Gas. *Physical Review* **136,** B864–B871 (3B 1964).

68. Kohn, W. & Sham, L. J. Self-Consistent Equations Including Exchange and Correlation Effects. *Physcial Review* **140,** A1133–A1138 (4A 1965).

69. Runge, E. & Gross, E. K. U. Density-Functional Theory for Time-Dependent Systems. *Physical Review Letters* **52,** 997–1000 (12 1984).

70. Burke, K., Werschnik, J. & Gross, E. Time-dependent density functional theory: Past, present, and future. *The Journal of Chemical Physics* **123,** 062206 (2005).

71. Furche, F. & Burke, K. *Annual Reports in Computational Chemistry 1, edited by D. Spellmeyer* 2005.

72. Levine, B. G., Ko, C., Quenneville, J. & MartÍnez, T. J. Conical intersections and double excitations in time-dependent density functional theory. *Molecular Physics* **104,** 1039–1051 (2006).

73. Casida, M. E., Jamorski, C., Casida, K. C. & Salahub, D. R. Molecular excitation energies to high-lying bound states from time-dependent density-functional response theory: Characterization and correction of the time-dependent local density approximation ionization threshold. *The Journal of Chemical Physics* **108,** 4439–4449 (1998).

74. Chu, S.-I. Recent development of self-interaction-free time-dependent density-functional theory for nonperturbative treatment of atomic and molecular multiphoton processes in intense laser fields. *The Journal of Chemical Physics* **123,** 062207 (2005).

75. Zhao, Y. & Truhlar, D. G. Density functional for spectroscopy: no long-range self-interaction error, good performance for Rydberg and charge-transfer states, and better performance on average than B3LYP for ground states. *The Journal of Physical Chemistry A* **110,** 13126–13130 (2006).

76. Tapavicza, E., Tavernelli, I. & Rothlisberger, U. Trajectory surface hopping within linear response time-dependent density-functional theory. *Physical Review Letters* **98,** 023001 (2007).

77. Barbatti, M. Nonadiabatic dynamics with trajectory surface hopping method. *Wiley Interdisciplinary Reviews: Computational Molecular Science* **1,** 620–633 (2011).

78. Tully, J. C. Molecular dynamics with electronic transitions. *The Journal of Chemical Physics* **93,** 1061–1071 (1990).

79. Thomas, L. H. *The calculation of atomic fields* in *Mathematical proceedings of the Cambridge philosophical society* **23** (1927), 542–548.

80. Fermi, E. A statistical method for determining some properties of the atom and its application to the theory of the periodic table of the elements. *Journal for Physics* **48,** 73–79 (1928).

81. Hohenberg, P. & Kohn, W. Inhomogeneous electron gas. *Physical Review* **136,** B864 (1964).

82. Born, M. & Oppenheimer, R. Zur Quantentheorie der Molekeln. *Annalen der Physik* **389,** 457–484 (1927).

83. Kohn, W. & Sham, L. J. Self-consistent equations including exchange and correlation effects. *Physical Review* **140,** A1133 (1965).

84. Becke, A. D. Perspective: Fifty years of density-functional theory in chemical physics. *The Journal of Chemical Physics* **140,** 18A301 (2014).

85. Dundas, D., Taylor, K. T., Parker, J. S. & Smyth, E. S. Double-ionization dynamics of laser-driven helium. *Journal of Physics B: Atomic, Molecular and Optical Physics* **32,** L231 (1999).

86. Runge, E. & Gross, E. K. Density-functional theory for time-dependent systems. *Physical Review Letters* **52,** 997 (1984).

87. Marques, M. A., Castro, A., Bertsch, G. F. & Rubio, A. octopus: a first-principles tool for excited electron–ion dynamics. *Computer Physics Communications* **151,** 60–78 (2003).

88. Hesselmann, A., Ipatov, A. & Görling, A. Charge-transfer excitation energies with a time-dependent density-functional method suitable for orbital-dependent exchange-correlation kernels. *Physical Review A* **80,** 012507 (2009).

89. Maitra, N. T., Zhang, F., Cave, R. J. & Burke, K. Double excitations within time-dependent density functional theory linear response. *The Journal of Chemical Physics* **120,** 5932–5937 (2004).

90. Cave, R. J., Zhang, F., Maitra, N. T. & Burke, K. A dressed TDDFT treatment of the 21Ag states of butadiene and hexatriene. *Chemical Physics Letters* **389,** 39–42 (2004).

91. Dreuw, A., Weisman, J. L. & Head-Gordon, M. Long-range charge-transfer excited states in time-dependent density functional theory require non-local exchange. *The Journal of Chemical Physics* **119,** 2943–2946 (2003).

92. Cordova, F. *et al.* Troubleshooting time-dependent density-functional theory for photochemical applications: Oxirane. *The Journal of Chemical Physics* **127,** 164111 (2007).

93. Krieger, J., Li, Y. & Iafrate, G. Construction and application of an accurate local spin-polarized Kohn-Sham potential with integer discontinuity: Exchange-only theory. *Physical Review A* **45,** 101 (1992).

94. Dobson, J. F., Bünner, M. & Gross, E. Time-dependent density functional theory beyond linear response: An exchange-correlation potential with memory. *Physical Review Letters* **79,** 1905 (1997).

95. Casida, M. E. in *Recent Advances In Density Functional Methods: (Part I)* 155–192 (World Scientific, 1995).

96. Beck, M. H., Jäckle, A., Worth, G. A. & Meyer, H.-D. The multiconfiguration time-dependent Hartree (MCTDH) method: a highly efficient algorithm for propagating wavepackets. *Physics Reports* **324,** 1–105 (2000).

97. Ben-Nun, M. & Martınez, T. J. Ab initio quantum molecular dynamics. *Advances in Chemical Physics* **121,** 439–512 (2002).

98. Stock, G. & Thoss, M. Semiclassical description of nonadiabatic quantum dynamics. *Physical Review Letters* **78,** 578 (1997).

99. Makhov, D. V., Symonds, C., Fernandez-Alberti, S. & Shalashilin, D. V. Ab initio quantum direct dynamics simulations of ultrafast photochemistry with Multiconfigurational Ehrenfest approach. *Chemical Physics* **493,** 200–218 (2017).

100. McLachlan, A. A variational solution of the time-dependent Schrodinger equation. *Molecular Physics* **8,** 39–44 (1964).

101. Micha, D. A. A self-consistent eikonal treatment of electronic transitions in molecular collisions. *The Journal of Chemical Physics* **78,** 7138–7145 (1983).

102. Kirson, Z., Gerber, R., Nitzan, A. & Ratner, M. Dynamics of metal electron excitation in atom-surface collisions: A quantum wave packet approach. *Surface Science* **137,** 527–550 (1984).

103. Sawada, S.-I., Nitzan, A. & Metiu, H. Mean-trajectory approximation for charge-and energy-transfer processes at surfaces. *Physical Review B* **32,** 851 (1985).

104. Wang, L., Akimov, A. & Prezhdo, O. V. Recent progress in surface hopping: 2011–2015. *The Journal of Physical Chemistry Letters* **7,** 2100–2112 (2016).

105. Ehrenfest, P. Bemerkung über die angenäherte Gültigkeit der klassischen Mechanik innerhalb der Quantenmechanik. *Journal for Physics* **45,** 455–457 (1927).

106. Tully, J. C. & Preston, R. K. Trajectory surface hopping approach to nonadiabatic molecular collisions: the reaction of H+ with D2. *The Journal of Chemical Physics* **55,** 562–572 (1971).

107. Yu, W. J. *et al.* Vertically stacked multi-heterostructures of layered materials for logic transistors and complementary inverters. *Nature Materials* **12,** 246–252 (2013).

108. Jariwala, D., Sangwan, V. K., Lauhon, L. J., Marks, T. J. & Hersam, M. C. Emerging device applications for semiconducting two-dimensional transition metal dichalcogenides. *ACS Nano* **8,** 1102–1120 (2014).

109. Wang, Q. H., Kalantar-Zadeh, K., Kis, A., Coleman, J. N. & Strano, M. S. Electronics and optoelectronics of two-dimensional transition metal dichalcogenides. *Nature Nanotechnology* **7,** 699–712 (2012).

110. Novoselov, K. S. *et al.* Electric field effect in atomically thin carbon films. *Science* **306,** 666–669 (2004).

111. Novoselov, K. S. *et al.* Two-dimensional gas of massless Dirac fermions in graphene. *Nature* **438,** 197–200 (2005).

112. Georgiou, T. *et al.* Vertical field-effect transistor based on graphene-WS_2 heterostructures for flexible and transparent electronics. *Nature Nanotechnology* **8,** 100 (2013).

113. Liu, X., Gao, P., Hu, W. & Yang, J. Photogenerated-Carrier Separation and Transfer in Two-Dimensional Janus Transition Metal Dichalcogenides and Graphene van der Waals Sandwich Heterojunction Photovoltaic Cells. *The Journal of Physical Chemistry Letters* **11,** 4070–4079 (2020).

114. Liu, Y. *et al.* Van der Waals heterostructures and devices. *Nature Review Materials* **1,** 1–17 (2016).

115. He, J. *et al.* Electron transfer and coupling in graphene–tungsten disulfide van der Waals heterostructures. *Nature Communications* **5,** 1–5 (2014).

116. Iida, K., Noda, M. & Nobusada, K. Photoinduced electron transfer at the interface between heterogeneous two-dimensional layered materials. *The Journal of Physical Chemistry C* **122,** 21651–21658 (2018).

117. Shan, H. *et al.* Electron transfer and cascade relaxation dynamics of graphene quantum dots/MoS_2 monolayer mixed-dimensional van der Waals heterostructures. *Materials Today* **24,** 10–16 (2019).

118. Wen, X. *et al.* Ultrafast probes of electron–hole transitions between two atomic layers. *Nature Communications* **9,** 1–9 (2018).

119. Massicotte, M. *et al.* Photo-thermionic effect in vertical graphene heterostructures. *Nature Communications* **7,** 1–7 (2016).

120. Garcia-Basabe, Y. *et al.* Ultrafast charge transfer dynamics pathways in two-dimensional MoS_2–graphene heterostructures: a core-hole clock approach. *Physical Chemistry Chemical Physics* **19,** 29954–29962 (2017).

121. Yuan, L. *et al.* Photocarrier generation from interlayer charge-transfer transitions in WS_2-graphene heterostructures. *Science Advances* **4,** e1700324 (2018).

122. Froehlicher, G., Lorchat, E. & Berciaud, S. Charge versus energy transfer in atomically thin graphene-transition metal dichalcogenide van der Waals heterostructures. *Physical Review X* **8,** 011007 (2018).

123. Aeschlimann, S. *et al.* Direct evidence for efficient ultrafast charge separation in epitaxial WS_2/graphene heterostructures. *Science Advances* **6,** eaay0761 (2020).

124. Krause, R. *et al.* Microscopic understanding of ultrafast charge transfer in van-der-Waals heterostructures. *arXiv preprint arXiv:2012.09268* (2020).

125. He, J., He, D., Wang, Y. & Zhao, H. Probing effect of electric field on photocarrier transfer in graphene-WS_2 van der Waals heterostructures. *Optical Express* **25,** 1949–1957 (2017).

126. Jones, A. M. *et al.* Optical generation of excitonic valley coherence in monolayer WSe_2. *Nature Nanotechnology* **8,** 634–638 (2013).

127. Wu, S. *et al.* Electrical tuning of valley magnetic moment through symmetry control in bilayer MoS_2. *Nature Physics* **9,** 149–153 (2013).

128. Ramasubramaniam, A., Naveh, D. & Towe, E. Tunable band gaps in bilayer transition-metal dichalcogenides. *Physical Review B* **84,** 205325 (2011).

129. Yu, W. J. *et al.* Highly efficient gate-tunable photocurrent generation in vertical heterostructures of layered materials. *Nature Nanotechnology* **8,** 952–958 (2013).

130. Britnell, L. *et al.* Strong light-matter interactions in heterostructures of atomically thin films. *Science* **340,** 1311–1314 (2013).

131. Tan, H. *et al.* Ultrathin 2D photodetectors utilizing chemical vapor deposition grown WS_2 with graphene electrodes. *ACS Nano* **10,** 7866–7873 (2016).

132. Soler, J. M. *et al.* The SIESTA Method for Ab Initio Order-N Materials Simulation. *Journal of Physics: Condensed Matter* **14,** 2745 (2002).

133. Blöchl, P. E. Projector Augmented-Wave Method. *Physical Review B* **50,** 17953 (1994).

134. Perdew, J. P., Burke, K. & Ernzerhof, M. Generalized Gradient Approximation Made Simple. *Physical Review Letters* **77,** 3865 (1996).

135. Troullier, N. & Martins, J. L. Efficient Pseudopotentials for Plane-Wave Calculations. *Physical Review B* **43,** 1993 (1991).

136. Lee, K., Murray, É. D., Kong, L., Lundqvist, B. I. & Langreth, D. C. Higher-Accuracy Van Der Waals Density Functional. *Physical Review B* **82,** 081101 (2010).

137. Meng, S. & Kaxiras, E. Real-time, Local Basis-Set Implementation of Time-Dependent Density Functional Theory for Excited State Dynamics Simulations. *Journal of Chemical Physics* **129,** 054110 (2008).

138. Dresselhaus, M. S., Jorio, A., Hofmann, M., Dresselhaus, G. & Saito, R. Perspectives on carbon nanotubes and graphene Raman spectroscopy. *Nano Letters* **10,** 751–758 (2010).

139. Zhao, W. *et al.* Lattice dynamics in mono-and few-layer sheets of WS_2 and WSe_2. *Nanoscale* **5,** 9677–9683 (2013).

140. Wang, H. *et al.* The role of collective motion in the ultrafast charge transfer in van der Waals heterostructures. *Nature Communications* **7,** 1–9 (2016).

141. Beard, M. C. *et al.* Comparing multiple exciton generation in quantum dots to impact ionization in bulk semiconductors: implications for enhancement of solar energy conversion. *Nano Letters* **10,** 3019–3027 (2010).

142. Wang, L.-W., Califano, M., Zunger, A. & Franceschetti, A. Pseudopotential theory of Auger processes in CdSe quantum dots. *Physical Review Letters* **91,** 056404 (2003).

143. Schaller, R. D. & Klimov, V. I. High efficiency carrier multiplication in PbSe nanocrystals: implications for solar energy conversion. *Physical Review Letters* **92,** 186601 (2004).

144. Ellingson, R. J. *et al.* Highly efficient multiple exciton generation in colloidal PbSe and PbS quantum dots. *Nano Letters* **5,** 865–871 (2005).

145. Cunningham, P. D. *et al.* Enhanced multiple exciton generation in quasi-one-dimensional semiconductors. *Nano Letters* **11,** 3476–3481 (2011).

146. Aerts, M. *et al.* Highly efficient carrier multiplication in PbS nanosheets. *Nature Communications* **5,** 1–5 (2014).

147. Kim, S.-T., Kim, J.-H. & Lee, Y. H. Carrier Multiplication in PbS quantum dots anchored on a Au tip using conductive atomic force microscopy. *Advanced Materials* **32,** 1908461 (2020).

148. Ma, Y.-J. *et al.* Enhanced carrier multiplication in InAs quantum dots for bulk avalanche photodetector applications. *Advanced Optical Materials* **5,** 1601023 (2017).

149. Mak, K. F., Lee, C., Hone, J., Shan, J. & Heinz, T. F. Atomically thin MoS_2: a new direct-gap semiconductor. *Physical Review Letters* **105,** 136805 (2010).

150. Splendiani, A. *et al.* Emerging photoluminescence in monolayer MoS_2. *Nano Letters* **10,** 1271–1275 (2010).

151. Li, M.-Y., Chen, C.-H., Shi, Y. & Li, L.-J. Heterostructures based on two-dimensional layered materials and their potential applications. *Materials Today* **19,** 322–335 (2016).

152. Radisavljevic, B., Radenovic, A., Brivio, J., Giacometti, V. & Kis, A. Single-layer MoS_2 transistors. *Nature Nanotechnology* **6,** 147–150 (2011).

153. Podzorov, V., Gershenson, M., Kloc, C., Zeis, R. & Bucher, E. High-mobility field-effect transistors based on transition metal dichalcogenides. *Applied Physics Letters* **84,** 3301–3303 (2004).

154. Bernardi, M., Palummo, M. & Grossman, J. C. Extraordinary sunlight absorption and one nanometer thick photovoltaics using two-dimensional monolayer materials. *Nano Letters* **13,** 3664–3670 (2013).

155. Villegas, C. E. & Rocha, A. Elucidating the optical properties of novel heterolayered materials based on $MoTe_2$-InN for photovoltaic applications. *The Journal of Physical Chemistry C* **119,** 11886–11895 (2015).

156. Polman, A., Knight, M., Garnett, E. C., Ehrler, B. & Sinke, W. C. Photovoltaic materials: Present efficiencies and future challenges. *Science* **352** (2016).

157. Frederiksen, T., Paulsson, M., Brandbyge, M. & Jauho, A.-P. Inelastic transport theory from first principles: Methodology and application to nanoscale devices. *Physical Review B* **75,** 205413 (2007).

158. Wang, H., Zhang, C. & Rana, F. Ultrafast dynamics of defect-assisted electron–hole recombination in monolayer MoS_2. *Nano Letters* **15,** 339–345 (2015).

159. Wang, H. *et al.* Fast exciton annihilation by capture of electrons or holes by defects via Auger scattering in monolayer metal dichalcogenides. *Physical Review B* **91,** 165411 (2015).

160. Kar, S., Su, Y., Nair, R. R. & Sood, A. Probing photoexcited carriers in a few-layer MoS_2 laminate by time-resolved optical pump–terahertz probe spectroscopy. *ACS Nano* **9,** 12004–12010 (2015).

161. Li, L. *et al.* Phonon-suppressed auger scattering of charge carriers in defective two-dimensional transition metal dichalcogenides. *Nano Letters* **19,** 6078–6086 (2019).

162. Duerloo, K.-A. N., Li, Y. & Reed, E. J. Structural phase transitions in two-dimensional Mo- and W-dichalcogenide monolayers. *Nature Communications* **5,** 1–9 (2014).

163. Ghorbani-Asl, M., Borini, S., Kuc, A. & Heine, T. Strain-dependent modulation of conductivity in single-layer transition-metal dichalcogenides. *Physical Review B* **87,** 235434 (2013).

164. Kan, M., Nam, H. G., Lee, Y. H. & Sun, Q. Phase stability and Raman vibration of the molybdenum ditelluride ($MoTe_2$) monolayer. *Physical Chemistry Chemical Physics* **17,** 14866–14871 (2015).

165. Guo, H. *et al.* Double resonance Raman modes in monolayer and few-layer $MoTe_2$. *Physical Review B* **91,** 205415 (2015).

166. Li, X. *et al.* Intrinsic electrical transport properties of monolayer silicene and MoS_2 from first principles. *Physical Review B* **87,** 115418 (2013).

167. Miah, M. A. R., Niaz, I. A. & Lo, Y.-H. Defect assisted carrier multiplication in amorphous silicon. *IEEE Journal of Quantum Electronics* **56,** 1–11 (2020).

168. Yuan, L. & Huang, L. Exciton dynamics and annihilation in WS_2 2D semiconductors. *Nanoscale* **7,** 7402–7408 (2015).

169. Plotzing, T. *et al.* Experimental verification of carrier multiplication in graphene. *Nano Letters* **14,** 5371–5375 (2014).

170. Johannsen, J. C. *et al.* Tunable carrier multiplication and cooling in graphene. *Nano Letters* **15,** 326–331 (2015).

171. Kadi, F., Winzer, T., Knorr, A. & Malic, E. Impact of doping on the carrier dynamics in graphene. *Scientific Reports* **5,** 1–7 (2015).

172. Tielrooij, K.-J. *et al.* Photoexcitation cascade and multiple hot-carrier generation in graphene. *Nature Physics* **9,** 248–252 (2013).

173. Geim, A. K. & Novoselov, K. S. in *Nanoscience and technology: a collection of reviews from nature journals* 11–19 (World Scientific, 2010).

174. Yu, Y.-J. *et al.* Tuning the graphene work function by electric field effect. *Nano Letters* **9,** 3430–3434 (2009).

175. Larciprete, R. *et al.* Oxygen switching of the epitaxial graphene–metal interaction. *ACS Nano* **6,** 9551–9558 (2012).

176. Riedl, C., Coletti, C., Iwasaki, T., Zakharov, A. & Starke, U. Quasi-free-standing epitaxial graphene on SiC obtained by hydrogen intercalation. *Physical Review Letters* **103,** 246804 (2009).

177. Wang, C. *et al.* Direct Observation of Global Elastic Intervalley Scattering Induced by Impurities on Graphene. *Nano Letters* **21,** 8258–8265 (2021).

178. Tomadin, A. *et al.* The ultrafast dynamics and conductivity of photoexcited graphene at different Fermi energies. *Science Advances* **4,** eaar5313 (2018).

179. Gierz, I. *et al.* Snapshots of non-equilibrium Dirac carrier distributions in graphene. *Nature Materials* **12,** 1119–1124 (2013).

180. Winzer, T. & Malić, E. Impact of Auger processes on carrier dynamics in graphene. *Physical Review B* **85,** 241404 (2012).

181. Emtsev, K., Speck, F., Seyller, T., Ley, L. & Riley, J. D. Interaction, growth, and ordering of epitaxial graphene on SiC {0001} surfaces: A comparative photoelectron spectroscopy study. *Physical Review B* **77,** 155303 (2008).

182. Ristein, J., Mammadov, S. & Seyller, T. Origin of doping in quasi-free-standing graphene on silicon carbide. *Physical Review Letters* **108,** 246104 (2012).

183. Shirley, E. L., Terminello, L., Santoni, A. & Himpsel, F. Brillouin-zone-selection effects in graphite photoelectron angular distributions. *Physical Review B* **51,** 13614 (1995).

184. Gierz, I., Henk, J., Höchst, H., Ast, C. R. & Kern, K. Illuminating the dark corridor in graphene: Polarization dependence of angle-resolved photoemission spectroscopy on graphene. *Physical Review B* **83,** 121408 (2011).

185. Liu, Y., Bian, G., Miller, T. & Chiang, T.-C. Visualizing electronic chirality and berry phases in graphene systems using photoemission with circularly polarized light. *Physical Review Letters* **107,** 166803 (2011).

186. Ulstrup, S. *et al.* Ultrafast dynamics of massive Dirac fermions in bilayer graphene. *Physical Review Letters* **112,** 257401 (2014).

187. Han, H.-V. *et al.* Photoluminescence enhancement and structure repairing of monolayer $MoSe_2$ by hydrohalic acid treatment. *Acs Nano* **10,** 1454–1461 (2016).

188. Wang, Y., Cong, C., Qiu, C. & Yu, T. Raman spectroscopy study of lattice vibration and crystallographic orientation of monolayer MoS_2 under uniaxial strain. *Small* **9,** 2857–2861 (2013).

189. Oliver, S. M. *et al.* Valley phenomena in the candidate phase change material $WSe_{2(1-x)}Te_{2x}$. *Communications Physics* **3,** 1–10 (2020).

190. Terrones, H. *et al.* New first order Raman-active modes in few layered transition metal dichalcogenides. *Scientific Reports* **4,** 1–9 (2014).

191. Wang, F. *et al.* Strain-induced phonon shifts in tungsten disulfide nanoplatelets and nanotubes. *2D Materials* **4,** 015007 (2016).

192. Gusakova, J. *et al.* Electronic properties of bulk and monolayer TMDs: theoretical study within DFT framework (GVJ-2e method). *Physica Status Solidi (a)* **214,** 1700218 (2017).